

Material development for extrusion-based 3D printing

DISSERTATION

zur Erlangung des akademischen Grades eines
Doktors der Naturwissenschaften (Dr. rer. nat.)
an der Bayreuther Graduiertenschule für Mathematik und
Naturwissenschaften der Universität Bayreuth

vorgelegt von

Minde Jin

Geboren in Jiangsu, VR China

Bayreuth, 2020

Material development for extrusion-based 3D printing

DISSERTATION

zur Erlangung des akademischen Grades eines
Doktors der Naturwissenschaften (Dr. rer. nat.)
an der Bayreuther Graduiertenschule für Mathematik und
Naturwissenschaften der Universität Bayreuth

vorgelegt von

Minde Jin

Geboren in Jiangsu, VR China

Bayreuth, 2020

Der experimentelle Teil der vorliegenden Arbeit wurde in der Zeit von Dezember 2014 bis November 2019 an der Universität Bayreuth am Lehrstuhl für Makromolekulare Chemie I unter Betreuung von Herrn Prof. Dr. Hans-Werner Schmidt angefertigt.

Vollständiger Abdruck der von der Bayreuther Graduiertenschule für Mathematik und Naturwissenschaften (BayNAT) der Universität Bayreuth genehmigten Dissertation zur Erlangung des akademischen Grades eines Doktors der Naturwissenschaften (Dr. rer. nat.).

Dissertation eingereicht am: 29.06.2020

Zulassung durch die Promotionskommission: 07.07.2020

Wissenschaftliches Kolloquium: 30.07.2020

Amtierender Direktor: Prof. Dr. Markus Lippitz

Prüfungsausschuss:

Prof. Dr. Hans-Werner Schmidt (Erstgutachter)

Prof. Dr. Volker Altstädt (Gutachter)

Prof. Dr. Seema Agarwal (Vorsitz)

Prof. Dr. Frank Döpfer



to my family

“There is nothing noble in being superior to some other man. The true nobility is in being superior to your previous self. “

Ernest Miller Hemingway (July 21, 1899 - July 2, 1961)

Table of contents

Abbreviations and symbols	I
Short summary	III
Kurzzusammenfassung	V
1. Introduction.....	1
1.1 Overview of important 3D printing technologies	1
1.1.1 Rapid prototyping and additive manufacturing.....	1
1.1.2 Typical 3D printing technologies.....	3
1.1.3 3D printing in the future	6
1.2 Extrusion-based 3D printing.....	9
1.2.1 Setup and principle	9
1.2.2. Challenges of extrusion-based 3D printing.....	11
1.3 Polymers for extrusion-based 3D printing.....	17
1.3.1 Commonly used thermoplastic materials.....	17
1.3.2 Polypropylene for extrusion-based 3D printing.....	20
1.4 Smart material for 4D printing	23
1.5 Reference.....	26
2. The objective of this thesis.....	38
3. Synopsis	40
3.1 Overview of the Thesis.....	40
3.2 Filament materials screening for FDM by means of injection molded short rods.....	42
3.3 Tailoring polypropylene for extrusion-based additive manufacturing.....	46
3.4 (AB) _n segmented copolyetherimides for 3D and 4D printing.....	50
4. Publications and manuscripts	54
4.1 List of publications and manuscripts	54
4.2 Individual contributions to the publications	55
4.3 Filament materials screening for FDM 3D printing by means of injection molded short rods.....	57
4.4 Tailoring polypropylene for extrusion-based additive manufacturing.....	64
4.5 (AB) _n segmented copolyetherimides for 4D printing.....	85
Extended summary.....	123
Acknowledgment	126

Abbreviations and symbols

2D	Two-dimensional
3D	Three-dimensional
4D	Four-dimensional
aPP	Amorphous polypropylene
AM	Additive manufacturing
ABS	Acrylonitrile-butadiene-styrene
ASA	Acrylonitrile-styrene-acrylate
CAD	Computer aided design
CLIP	Continuous liquid interface production
CNC	Computer numerical control
CT	Computed tomography
DoE	Design of experiment
D_{warp}	Warp deformation
E	Young's modulus
FDM	Fused deposition modeling
FFF	Fused filament fabrication
FLM	Fused layer manufacturing
G'	Storage modulus
G''	Loss modulus
iPP	Isotactic polypropylene
LLDPE	Linear low-density polyethylene
MRI	Magnetic resonance imaging
NA	Nucleating agent
PA	Polyamide
PBT	Poly(butylene terephthalate)
PC	Polycarbonate
PCL	Poly(ϵ -caprolactone)
PE	Polyethylene
PEG	poly(ethylene glycol)
PETG	Poly(ethylene terephthalate) glycol-modified
PEI	Polyetherimide

PI	Polyimide
PLA	Poly lactide
POM	Polyoxymethylene
PP	Polypropylene
PPS	Poly(phenylene sulfide)
PPSU	Polyphenylsulfone
PS	Polystyrene
PTFE	Polyetheretherketone
PVC	Poly(vinyl chloride)
Raco PP	Polypropylene-ethylene random copolymer
RP	Rapid prototyping
SAN	Styrene-acrylonitrile
SDCNF	Spray-dried cellulose nanofibril
SL	Stereolithography
SLS	Selective laser sintering
SMP	Shape memory polymer
T	Temperature
T_g	Glass transition temperature
T_m	Melting temperature
T_{trans}	Transition temperature
TPE	Thermoplastic elastomer
TPU	Thermoplastic polyurethane
UV	Ultraviolet
X%	Degree of crystallization

Short summary

The motivation for this thesis arises from the rapidly emerging field of additive manufacturing. Among 3D printing technologies, extrusion-based additive manufacturing, also known as fused deposition modeling (FDM) or fused filament fabrication (FFF), is one of the most widely-used processes. Here, a thermoplastic extrusion process provides in combination with computer-numerical-controlled technology a cost-effective layer by layer production of 3D printed parts. There is a demand for targeted material development for extrusion-based 3D printing. In this context, the thesis covers (i) an efficient material screening method for the development and testing of polymers for extrusion-based 3D printing, (ii) tailoring polypropylene for extrusion-based additive manufacturing and (iii) a new class of $(AB)_n$ segmented copolyetherimides for 3D and 4D printing.

The *Introduction* gives a brief overview of 3D printing technologies with special emphasis on extrusion-based 3D printing. The principles, challenges, and commonly used polymers are discussed. Particular focus is given on the semi-crystalline polypropylene, which is underrepresented in extrusion-based 3D printing in spite of its outstanding broad property profile. In addition, smart materials with shape memory effects are presented in view of 4D printing.

This cumulative thesis consists of three topics, which resulted in already two publications and one manuscript. An overview of the thesis and a summary of the significant achievements are presented in chapter *Synopsis*.

The first topic deals with the development of an *efficient material screening method to identify and optimize thermoplastic polymers for extrusion-based 3D printing*. Usually, the feedstock material is a continuous filament. For the filament production, quantities of several kilograms are required. To overcome this issue, efficient small-scale screening and testing method, which requires only 10 to 50 g is essential to screen and further develop materials for extrusion-based 3D printing. This issue was solved in this thesis by using a mini compounder and a mini injection molding machine to produce short filament rods which were joint together and used as feedstock in the 3D printer. Also, a particular test specimen, in the form of a printed free-standing square tube consisting of only a single-material-line stack was used for evaluation of critical performance parameters of the printed parts, in particular warp deformation and interlayer bonding quality. By this advanced

method, the required time and material consumption are significantly reduced. To validate the method, three different grades of polypropylene are processed into filament rods and compared to two commercially available PP filaments and a commercial ABS filament.

The second topic deals with *tailoring polypropylene for extrusion-based 3D printing*. Polypropylene is one of the most commonly applied semi-crystalline thermoplastic in consumer and technical products and, therefore, a promising candidate for 3D printing. However, at the beginning of the thesis, only a limited number of commercial PP filaments were available, which suffer from relatively high volume shrinkage and warp deformation. Therefore, different PPs grades were selected and modified with the aim to reduce warp deformation and to reduce the anisotropic properties by improving the interlayer bonding quality. Two commercially available grades of polypropylene/ethylene random copolymers with a lower degree of crystallization were explored. To modify these grades, a β -nucleating agent was selected as an additive, and several amorphous polypropylenes (aPP) and one linear low-density polyethylene (LLDPE) were chosen as a blend component. The achieved results demonstrate that the crystallization behavior and E-modulus of polypropylene play a significant role in reducing warp deformation. An outstanding interlayer bonding strength was obtained in blends with raco PP/aPP. The improvement of the interlayer quality was confirmed by tensile tests, optical microscope, and visualized by the jumping of a 3D printed frog.

In the third topic, a new class of *(AB)_n segmented copolyetherimides for 3D and 4D printing* was developed. The (AB)_n segmented copolyetherimides consist of perylene segments and poly(ethylene glycol) segments were synthesized and characterized regarding their thermal, rheological, and mechanical properties in view of 3D printing. The perylene imide segments act as reversible physical crosslinks, which disassemble at temperatures between 100 and 200°C. The existing crystallinity of PEG segments improves the stiffness of produced filament rods, which is essential to feed them smoothly into the 3D printer. The results demonstrate that this type of (AB)_n segmented copolyetherimides combine good 3D printing performance with low warp deformation and excellent interlayer bonding. The PEG segments exhibit a low melting temperature around 40 to 60 °C and are semi-crystalline at room temperature, which could act as switching domains for shape memory programming. With a blend of two synthesized (AB)_n segmented copolyetherimides, shape memory effect is realized by tuning the thermal transitions. By 3D printing this blend, 4D printing is achieved and demonstrated.

Kurzzusammenfassung

Die Motivation für diese Doktorarbeit begründet sich aus dem schnell wachsenden Bereich der additiven Fertigung. Unter den 3D-Drucktechnologien ist die extrusionsbasierte additive Fertigung, auch bekannt als Fused Deposition Modeling (FDM) oder Fused Filament Fabrication (FFF), eines der am weitesten verbreiteten Verfahren. Hier bietet ein thermoplastisches Extrusionsverfahren in Kombination mit computergestützter Verarbeitung eine kostengünstige Schicht-für-Schicht-Herstellung von 3D-Druckobjekten. Allerdings besteht ein sehr großer Bedarf an einer gezielten Materialentwicklung für den extrusionsbasierten 3D-Druck. In diesem Zusammenhang behandelt diese Doktorarbeit (i) ein effizientes Material-Screening-Verfahren für die Entwicklung und Prüfung von Polymeren für den extrusionsbasierten 3D-Druck, (ii) die maßgeschneiderte Modifikation von Polypropylen für die extrusionsbasierte additive Fertigung und (iii) eine neue Klasse von $(AB)_n$ segmentierten Copolyetherimiden für den 3D- und 4D-Druck.

Die Einführung gibt einen kurzen Überblick über gängige 3D-Drucktechnologien mit besonderem Schwerpunkt auf den extrusionsbasierten 3D-Druck. Die Prinzipien, Herausforderungen und am häufigsten verwendeten Polymere werden diskutiert. Ein besonderes Augenmerk wird auf das teilkristalline Polypropylen gelegt, das im extrusionsbasierten 3D-Druck trotz seines herausragenden breiten Eigenschaftsprofils unterrepräsentiert ist. Darüber hinaus werden „Smart Materials“ mit Formgedächtniseffekten für den 4D-Druck vorgestellt.

Diese kumulative Doktorarbeit beschäftigt sich mit drei Themen, aus denen bereits zwei Veröffentlichungen und ein Manuskript hervorgegangen sind. Eine Übersicht über die Arbeit und eine Zusammenfassung der wesentlichen Erfolge finden Sie im Kapitel *Synopsis*.

Das erste Thema befasst sich mit der Entwicklung einer effizienten Material-Screening-Methode zur Identifizierung und Optimierung thermoplastischer Polymere für den extrusionsbasierten 3D-Druck. Normalerweise ist das Ausgangsmaterial ein kontinuierliches Filament. Für die Filamentherstellung werden Mengen von mehreren Kilogramm benötigt. Die Lösung dieses Problems wäre ein effizientes materialsparendes Screening- und Testverfahren, das nur 10 bis 50 g erfordert. Dieses Problem wurde in dieser Arbeit angegangen und gelöst, indem kurze Filamentstäbchen mit Hilfe einer Mini-Compoundieranlage und einer Mini-Spritzgießmaschine hergestellt wurden. Die spritzgegossenen Filamentstäbchen wurden anschließend miteinander

verbunden und als Druckmaterial im 3D-Drucker verwendet. Außerdem wurde ein spezieller Prüfkörper in Form eines 3D-gedruckten freistehenden Vierkantrohrs (Würfel ohne Boden und Deckel), das nur aus einem einzelnen übereinander gedruckten Linienstapel besteht, zur Auswertung der entscheidenden Optimierungsparameter der gedruckten Teile, insbesondere dem Verzug und der Haftung der übereinander gedruckten Schichten, entwickelt und verwendet. Durch diese weiterentwickelte Methode werden Zeit- und Materialverbrauch erheblich reduziert. Zur Validierung dieser Methode wurden drei verschiedene Polypropylen zu Filamentstäbchen verarbeitet und mit zwei im Handel erhältlichen PP-Filamenten und einem handelsüblichen ABS-Filament verglichen.

Das zweite Thema befasst sich mit der *maßgeschneiderten Modifikation von Polypropylen für den extrusionsbasierten 3D-Druck*. Polypropylen ist einer der am häufigsten verwendeten teilkristallinen Thermoplaste, wird unter anderem in großen Mengen in Konsumgüter und technischen Produkten eingesetzt und ist daher ein vielversprechender Kandidat für den 3D-Druck. Zu Beginn der Doktorarbeit war jedoch nur eine begrenzte Anzahl von handelsüblichen PP-Filamenten verfügbar und diese verursachten einen relativ hohen Volumenschwund und Verzug in den davon 3D-gedruckten Objekten. Daher wurden verschiedene PP-Typen ausgewählt und modifiziert, um den Verzug und die anisotrope Eigenschaft der 3D-gedruckten Objekte durch eine verbesserte Haftung zwischen den Schichten zu verringern. Es wurden zwei im Handel erhältliche Typen von Polypropylen / Ethylen-Random-Copolymere mit geringen Kristallisationsgraden untersucht. Um diese Polymere zu modifizieren, wurde ein β -Nukleierungsmittel als Additiv, mehrere amorphe Polypropylentypen (aPP) und ein lineares Polyethylen mit niedriger Dichte (LLDPE) als Mischungskomponenten ausgewählt und eingearbeitet. Die erzielten Ergebnisse zeigen, dass das Kristallisationsverhalten und der E-Modul des eingesetzten Polypropylens eine wichtige Rolle bei der Verringerung des Verzugs spielen. Eine hervorragende Haftung zwischen den 3D-gedruckten Schichten wurde in Mischungen mit Raco PP/aPP erhalten. Die im Rahmen dieser Arbeit erreichten Erfolge in Bezug auf die Haftung zwischen den Schichten sind mit Hilfe von Zugversuchen und der optischen Mikroskopie dokumentiert und anhand des Springens eines 3D-gedruckten Frosches eindrucksvoll demonstriert.

Im dritten Thema wurde eine *neue Klasse von $(AB)_n$ -segmentierten Copolyetherimiden für den 3D- und 4D-Druck* entwickelt. Die synthetisierten $(AB)_n$ -segmentierten Copolyetherimide bestehen aus Perylen- und Poly(ethylenglykol)-Segmenten und wurden hinsichtlich ihrer thermischen,

rheologischen und mechanischen Eigenschaften im Hinblick auf den 3D-Druck charakterisiert. Die Perylenimidsegmente wirken als reversible physikalische Vernetzungspunkte, die sich bei Temperaturen zwischen 100 und 200 °C reversibel auflösen. Die vorhandene Kristallinität der PEG-Segmente verbessert die Steifigkeit der hergestellten Filamentstäbchen, was für eine reibungslose Förderung der Filamente im 3D-Drucker extrem vorteilhaft ist. Die Ergebnisse zeigen, dass die synthetisierten (AB)_n-segmentierten Copolyetherimiden sich sehr gut 3D drucken lassen, einen geringen Verzug und eine hervorragende Haftung zwischen den gedruckten Schichten aufweisen. Die PEG-Segmente weisen einen niedrigen Schmelztemperaturbereich zwischen 40 bis 60 °C auf und sind bei Raumtemperatur teilkristallin. Diese Eigenschaft qualifiziert sie zur Verwendung als „Switching Domains“ für die Formgedächtnisprogrammierung in 4D-gedruckten Objekten. Die Realisation des Formgedächtniseffektes gelang allerdings erst mit einer Blend Mischung aus zwei synthetisierten (AB)_n-segmentierten Copolyetherimiden, in der die thermischen Übergänge über das Mischungsverhältnis eingestellt werden konnten. Durch den 3D-Druck dieser optimierten Blend Mischung wurde der 4D-Druck erfolgreich durchgeführt und demonstriert.

1. Introduction

The term “3D printing” is nowadays used for a technology that enables the instant production of 3D objects without conventional tooling. It opens up a completely new era for digital design and intelligent manufacturing which will play an important role in the next industry evolution (industry 4.0). The developments of new tailored polymer materials are the most challenging task for driving this emerging technology to be used by nearly all branches of industry. In this work, a well-designed feedstock material development approach for 3D printing is investigated and established. Firstly, an overview of important 3D printing technologies consists of concepts, typical examples, evolution history, and outlooks will be shown (**Chapter 1.1**). Then, from all 3D printing technologies, the focus is on extrusion-based 3D printing, often referred to as fused filament fabrication (FFF), fused layer manufacturing (FLM), or fused deposition modeling (FDM), which is one of the most widely-used and representative 3D printing technique. Here, the advantages and drawbacks of extrusion-based 3D printing are explained with respect to the process principle and applied material (**Chapter 1.2**). For 3D printed thermoplastics, the degree of crystallinity is essential and critical for the final object quality (**Chapter 1.3.1**). The semi-crystalline polypropylene, which is one of the promising materials for extrusion-based 3D printing must be optimized to overcome the issues mainly caused by crystallization (**Chapter 1.3.2**). At last, based on the combination of 3D printing and smart materials, 4D printing is demonstrated with time as additional 4th dimension. The applied smart material with a shape memory effect is based on (A-B)_n segmented copolyetherimides (**Chapter 1.3.3**). In summary, the introduction aims to achieve a better understanding of 3D printing technologies and used materials.

1.1 Overview of important 3D printing technologies

1.1.1 Rapid prototyping and additive manufacturing

The idea of producing complex 3D objects within a very short time but without the need of sophisticated tooling in the American automotive industry is regarded as the first initiator of the later blooming of rapid prototyping (RP) technology [1]. However, in that early time, the RP concept was still far beyond the reality due to lack of computational capabilities before the introduction of three-dimensional computer-aided design (CAD) until the early 1980s. From that time now, RP started to own its “spirit” and was capable of serving this promising idea. Rapid prototyping (RP), also reported as “additive manufacturing” (AM) or “3D printing”, was defined as a number of technologies that enable the idea above: objects to be produced instantly without conventional tooling [1]. During the last decades, numerous additive manufacturing

technologies and 3D printers, each with their own specific advantages, were rapidly developed to shorten the production development cycle and produce customized parts with defined functionality and individuality [2,3]. *Figure 1* is an illustration of additive manufacturing processes of building a three-dimensional object (a square tube) from the respective digital model (CAD designed square tube) with the help of a 3D printer that is capable of producing freestanding 3D objects layer by layer without any tooling.

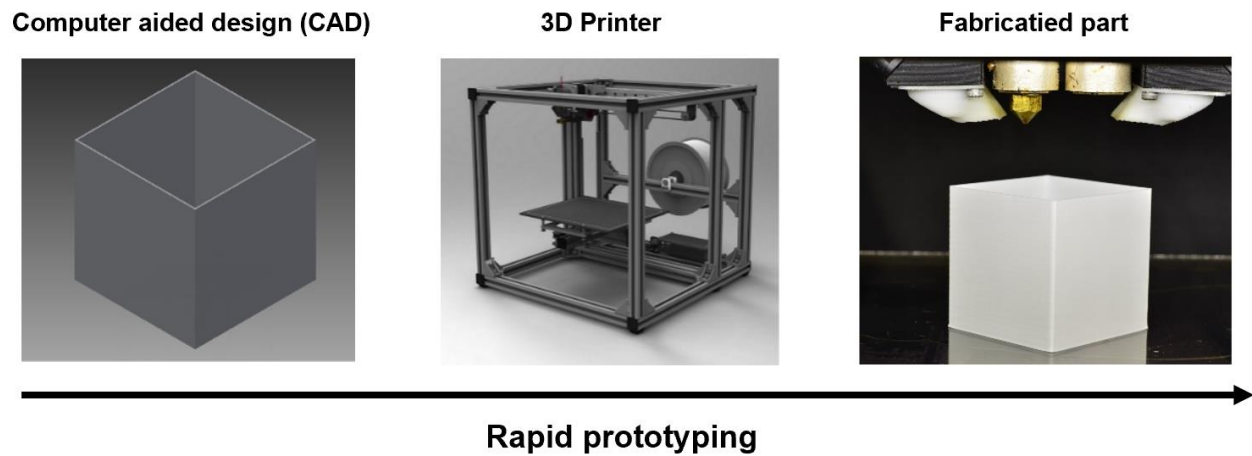


Figure 1: Schematic illustration of rapid prototyping (RP) utilizing 3D printing. With the help of computer-aided design (CAD) and a 3D printer, an object (here a square tube) can be rapidly produced without any tooling.

Contrary to subtractive manufacturing methods, e.g., computer numerical control (CNC) with a milling machine, additive manufacturing produces objects by fusing materials layer by layer according to given three-dimensional digital model data [4]. For a typical additive manufacturing or 3D printing process, after the model design with CAD, a special slicing software is necessary to “slice” the CAD file into a series of horizontally digital slices and to send the generated G-code-file to a 3D printer. The G-code-file is a simple text-code that tells the 3D printer how to print the object layer by layer. Each printed layer is directly added following certain contact or bonding principles and mechanisms on top of the previous layer (see also **Chapter 1.1.2**). The key difference of 3D printing compared with 2D printing is that the dried flat ink on the paper is now a 3D manufactured object on the 3D printer desk produced by a series of 2D printed layer stacks. *Figure 2* illustrates the main concept of additive manufacturing: layer by layer. Here, a squared tube was firstly designed by CAD and then converted to layer file, the 3D printer (FFF printer, see **Chapter 1.2**) printed the square tube layer by layer according to the layer information.

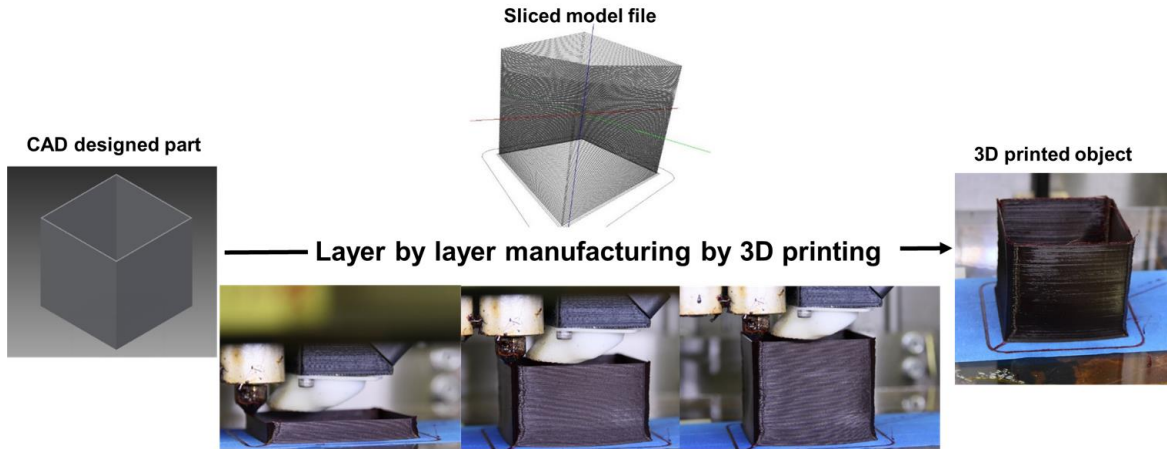


Figure 2: Schematic illustration of additive manufacturing concept: layer by layer. Concept starts from CAD software designed digital model (a square tube), which is then transformed into respective sliced model file, 3D printed by the controlled layer by layer movement of an extrusion-based 3D printer head to obtain the final 3D printed object on a build-up platform.

1.1.2 Typical 3D printing technologies

Shortly after the first 3D printer was invented in 1984, over 40 different kinds of 3D printing concepts have been developed until 1999 [1]. After a further 20 years, a large number of RP and AM processes are well established [1]. 3D printing is nowadays able to manufacture individual designed objects or prototypes for new production methods and inventions. More rapidly and additionally cheaper produced prototypes compared with the conventional manufacturing (e.g., injection molding and extrusion) can save not only precious time in the early stage of production design but also become a valuable communication tool to connect with all departments of engineering, manufacturing, marketing and purchasing or even the customers along the production chain. 3D printing offers an early preview on new products during the design phase. At the same time, meaningful modifications basing on the feedback from all the production chain can be achieved within a short time at low cost [3]. In some cases, 3D printing can also provide direct manufacturing of functional or semi-functional components [4,5]. For some other cases, where the traditional manufacturing processes are restricted, the layered construction could also solve the problem of complex cavities such as in sophisticated artworks [4]. Not only the blooming of technology itself, with the explosion of material innovations, 3D printing will also lead to a larger impact in areas such as medical applications and architecture. Printed live tissue, organs, or even bridges on the river are no longer scientific fictions.

All 3D printing technologies differ themselves in the way how the layers are deposited and bonded to produce the parts, and the materials they use [6]. Some methods sinter or melt the printing materials in order to form layers, e.g., selective laser sintering (SLS) and extrusion-based additive manufacturing. While other techniques cure liquid materials by laser or ultraviolet light (UV) exposure, e.g., stereolithography (SL) and continuous liquid interface production (CLIP). Some of the 3D printers use a binder for binding together the powdered starting material e.g. binder jetting printing. Some others just deposits without any binding agent. The material is plotted directly, holds together and sticks to itself, e.g., ink jetting/bio-printing. Each method has its advantages and limitations. For choosing the suitable RP technology, it mainly depends on the applied materials and requirements of end-user. Here, a taxonomy is used, and 3D printing technologies are divided into three main groups according to the layer bonding mechanism. *Figure 3* is a tree map of 3D printing technologies based on different layer bonding mechanisms.

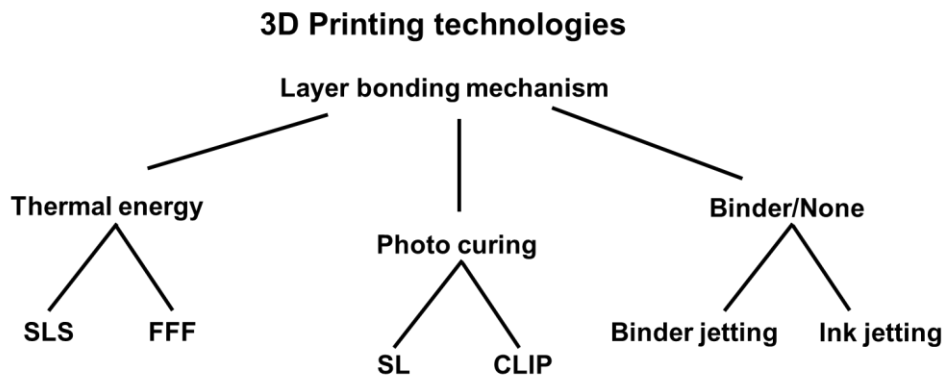


Figure 3: Taxonomy of 3D printing technologies based on layer bonding mechanism. The main bonding mechanisms are based on thermal energy, photo curing, and the use of a binder. For each group, exemplarily two 3D printing techniques are listed.

Selective laser sintering and extrusion-based additive manufacturing

Selective laser sintering (SLS) and extrusion-based additive manufacturing (extrusion-based AM) are the most widely used 3D printing techniques in terms of the thermal energy bonding mechanism category. Used materials for SLS are normally plastic, ceramic, or metal fine powders, which are heated and sintered together with a CO₂ laser [7]. Each layer is built up with the help of the laser, which scans the powder bed according to the sliced model file. The printing chamber is heated just a few degrees Celsius below the melting temperature of the material in order to minimize a temperature gradient and to facilitate fusion to the previous layer [8]. After the final sintering of one layer, a new powder layer is spread evenly. The laser-sintered powder forms the object, and the unsintered powder supports the structural geometry of the object.

However, the obtained object has to be bared, and its surface cleaned extensively [9]. The clear advantage of this technology is the available material diversity, especially for engineering applications [7]. The drawback of this technology is the use of fine powders, which are difficult and time-consuming to obtain, as well as the expensive machine costs.

Extrusion-base AM is one of the most widely-used 3D printing technology [5]. The technique combines a simplified thermoplastic extrusion process with CNC technology and thus provides a cost-effective layered production of 3D printed parts (see **Chapter 1.2.1**). For extrusion-based AM thermoplastic materials supplied as a continuous feedstock filament are usually needed [10]. The main advantage of this technique is the availability of cheap desktop setups with a wide range of available materials (see **Chapter 1.3.1**). However, relatively restricted dimensional accuracy and the anisotropic property of 3D printed layered objects are the drawbacks of the extrusion-based AM technology (details see **Chapter 1.2.2**)

Stereolithography and continuous liquid interface production

Stereolithography (SL) is the most popular 3D printing process among currently available RP technologies. The main concept is applying a photosensitive monomer resin by forming a solidified polymer material when exposed to ultraviolet light or laser [11,12]. An SL machine consists of a build platform that is in a filled resin vat. The build platform is very close to the resin surface but covered by a thin film of resin. The first layer is imaged when this thin resin film is exposed by the light source according to slicing information. Once the first slice has been scanned and polymerized, the platform is lowered for one-layer height and the build platform with the printed layer again covered by resin flow. The next layer could then be scanned, and thus layer by layer the part is growing until it is finished.

Recently, continuous liquid interface production (CLIP) was introduced by utilizing the inhibition effect of oxygen by free-radical photopolymerization [13,14]. Different from the traditional SL process with a layer by layer polymerization of applied resin, a thin oxygen-containing zone was managed at the bottom of the vat. The oxygen-containing zone creates a liquid interface in the CLIP printer where radical polymerization is quenched and the liquid resin monomer can flow. Due to this principle, the printed object can be pulled out of the resin monomer vat while it is exposed and thus continuously growing slightly above the bottom of the vat. Compared with traditional SL, the uncured liquid monomer layer between the growing object and the invented transparent bottom of vat allows the simultaneous production of the part, the renewal of the resin, and the movement of the build platform elevator for a faster production [13,14]. The advantages of CLIP are the high resolution, the fast speed, and the relative isotropic mechanical properties of 3D printed objects. The drawbacks are the restricted photo-curable materials and the high setup costs [13].

Binder jetting and ink jetting

Binder jetting is similar to SLS. But here, the powdered material is glued together with the help of a binder sprayed through a nozzle to defined points [15]. Once the part is completed, it will be heated to evaporate binder excess. Similar to SLS, the unused powder supports the structural geometry of the object. A final printed part is usually be tempered or finally carefully sintered to improve mechanical properties [15]. The obtained resolution mainly depends on the size of applied binder droplets and powder grains. Binder jetting printers are expensive, and applied materials are very restricted and time-consuming in production due to the powder form. There exists a related technique widely used in bio-fabrication, which uses ink instead of a binder. The deposition-based ink-jetting 3D printing deposits a defined small amount (1–100 picolitres) of bio-ink on a substrate and thus offers a high resolution and precision [16]. Applied bioinks normally consist of hydrogels which allow cell carrying and offer suitable rheological properties for inkjet processing [17,18]. To date, with the help of medical CT (computed tomography) or MRI (magnetic resonance imaging), live tissues and organs could already be medically analyzed, scanned, and printed for patients on a customized basis [19].

1.1.3 3D printing in the future

In addition to conventional fabrication processes (e.g., injection molding and extrusion) additive manufacturing concepts and 3D printing technologies are opening up a new era for digital design and manufacturing and impact our life in almost all aspects.

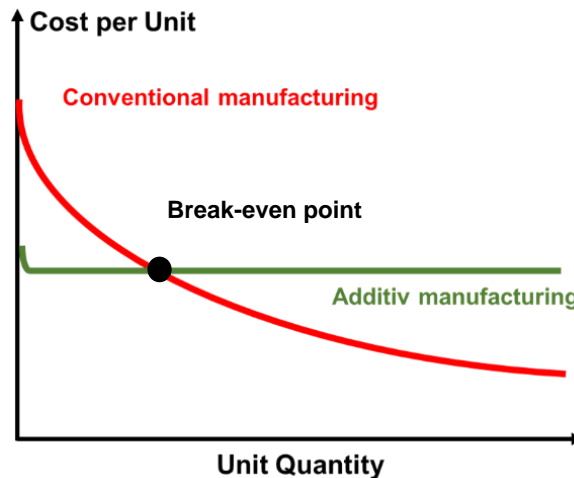


Figure 4: Schematic comparison of cost per unit as a function of unit quantity between conventional and additive manufacturing. Additive manufacturing demonstrates clear cost advantages at lower unit quantities due to the expensive mold and tooling costs of conventional manufacturing. The break-even point depends on production complexity, volume and material. [20,21]

The drawbacks of 3D printing are also obvious in fabrication speed, part quality and fabrication cost in larger unit quantity makes 3D printing an ideal complementary of conventional fabrication processes. With the innovation of new materials for 3D printing, more and more applications rely on 3D printing, where conventional fabrication methods are often too expensive or limited. Printed live tissues and organs are no longer scientific fictions but already built up layer by layer from cells and tissue [19,22]. In the near future, automation and 3D printing will play a considerable role in branches such as architecture, civil engineering, building construction, and even aerospace with the advantages of less time-consuming and more human work and environmentally friendly production without waste [23–26]. Smart factories that can respond to customer demands for tailored products involving 3D printers, cloud computing, and big data are future trends [27,28]. A totally new environment consists of smart factories, and intelligent manufacturing processes will lead to further implementation of Industry 4.0 (the fourth industrial revolution) [29].

As a summary, rapid prototyping and 3D printing technologies are faster, cheaper, and smarter manufacturing concepts for many cases. These new techniques are not direct competitors to conventional manufacturing technologies but acting as complementary production facilities, and will encourage and drive all technical innovations and change the world in the near future [1]. In the following paragraph, the evolution of 3D technology over the last 30 years will be discussed with the help of the “hype cycle” [30].

Hype cycle

The hype cycle is a branded graphical presentation of company Gartner for studying and demonstrating the maturity, adoption, and social application (i.e., life-cycle) of emerging technologies [30,31]. The hype cycle provides a five phases theory and gives you a view of how a technology or application will evolve to maturity over time [30,31]. The first phase is called “innovation trigger”, it is the beginning of a potential technology in publicity, but the commercial viability is unproven. For 3D printing, this phase started around the late 1980s, which is the time *Stratasys* introduced the first FDMTM printer. Then the technology comes to the phase of “peak of inflated expectations”. Here, the early generation of 3D printers produced several success stories, but the limits of the technology itself were still being discussed. In the hyper cycle of the year 2011, 3D printing technology is located exactly at the beginning of the phase “peak of inflated expectations”, which means many people have heard and recognized 3D printing. Most of the reported stories about 3D technologies are positive, and therefore the expectations for 3D printing are getting higher and higher. Many enterprises, universities, and even hobby makers purchase 3D printers for part production, research, or development. In Hyper cycle 2011, the 3D bioprinting started just its “innovation trigger phase” and will draw more scientific attention due to the unique advantages of 3D printing utilized for tissue engineering [32].

In 2014, the hype cycle was quite different from 2011 [34]. However, the 3D bioprinting is still in the “innovation trigger phase”. 3D printing technology was split into two production segments, and one is called *consumer 3D printing* and the other *enterprise 3D printing combined with 3D scanning*. Consumer 3D printing, e.g., utilizing commercially available FDM™ desktop 3D printers, was at this time in the phase of “trough of disillusionment”. Because of its simplified setup and low cost, the drawbacks and limitations of consumer 3D printer were accepted by their users. In a consequence, people gain a more overall and deeper understanding of 3D printing technologies. At the same time, enterprise 3D printing succeeded into the stage of “slope of enlightenment”. After years of experience dealing with certain 3D printing technologies, enterprises start to understand how this technology can benefit both the company and the customer. Increased research funds, new projects, and detailed feedback from early researches pushed the development of a new generation of 3D printers. With the progress of 3D scanning (also in hype cycle 2014, together with enterprise 3D printing), non-modeling & non-tooling manufacturing or reverse manufacturing and engineering were available at this time [33]. At last, the 3D printing technology was heading to the last phase in the hype cycle [35], called “plateau of productivity”. After years of development, the mainstream adopted this “matured” technology. The viability and applicability are clearly demonstrated by plenty of successful cases and commercially available 3D printed products and services.

After passing through the five phases of the hype cycle, the further development of 3D printing in the future will drive the blooming of this modern technology in almost every technical branches and other areas of life. More and more brilliant ideas, which may be impossible before, are becoming a reality. Skilled 3D model designers and printing software programmers will build a fundamental frame consists of highly developed 3D printing systems. Their simple use could allow ideas generated in the human brain to be turned into tailor-made physical objects with the help of intelligent manufacturing systems [28]. In hype cycle 2018, we find that the 3D printing technology and even 3D bioprinting is no longer listed, indicating that the rapid prototyping technology is fully mature since its birth in the 1980s. However, a brand new technology, based on 3D printing, named 4D printing emerged in the hype cycle of the year 2018.

4D printing

With the development of 3D printing technology, material development was always the most powerful driving force along the time axis of hype cycle. In recent years, one class of materials with distinct advantages came into the spotlight for 3D printing, which is called smart or intelligent materials [36–38]. By applying smart materials for 3D printing, the printed part is no longer “lifeless”, thus the new term “4D

printing” was created. *Figure 5* shows the schematic illustration of the 4D printing concept using a printed “Eiffel Tower” to demonstrate the shape memory effect of an applied smart polymer material [38–40].

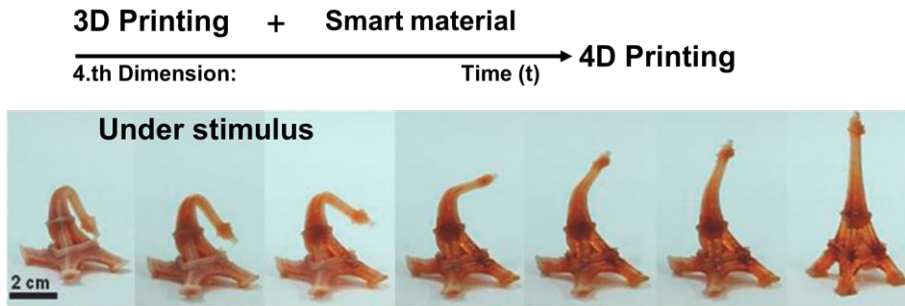


Figure 5: Schematic illustration of 4D printing concept. The 3D printed Eiffel Tower from smart material that reverts to its original shape over time in response to an external stimulus (exposed to 70 °C). (Figure 5 modified from reference[38], reprint and reuse with permission from John Wiley and Sons.)

The 4D printing could be defined as a process of creating a physical object using a smart material by a 3D printing technology. In this context, the used smart material allows a controllable response to a stimulus from the environment by changing shape or properties over time [41]. 4D printing opens new paths for creating diverse shape-shifting concepts and functionalities for tissue engineering, biomedical devices, soft robotics and biomedical devices, and drug delivery [39,41,42]. The key element of 4D printing, the smart materials is discussed in detail in **Chapter 1.4**.

1.2 Extrusion-based 3D printing

1.2.1 Setup and principle

Extrusion-based 3D printing or also known as extrusion-based additive manufacturing, was firstly introduced by *Scott Crump* in the late 1980s and commercialized in 1990 by the company *Stratasys* [43]. It is nowadays one of the most widely-used and representative technique of rapid prototyping technologies. Extrusion-based 3D printing combines a simplified mini-extruder with computer-numerical-controlled (CNC) technology, which provides cost-effective layered processing of thermoplastics. The printed part is built by extruding a small amount of a molten thermoplastic polymer from a hot nozzle to form each layer [10]. The figure below shows a schematic illustration of a setup typically used for extrusion-based 3D printing with details of filament passing through the feeding system and liquefier. Thermoplastic materials supplied as a continuous feedstock filament is driven by a feeding system equipped with driving wheels into the liquefier. From the liquefier, the softened and melted material is then deposited through a nozzle, which is attached to an integrated 2-axis motor system that moves the nozzle in X and Y directions [2]. A digital model file, which contains the tool path information of each layer, controls the movements of the nozzle.

When the current layer is finished, the next layer starts on top of the previous layer after lifting the nozzle or lowering the worktable by just one layer step height in the Z-axis (*Figure 6* (left)).

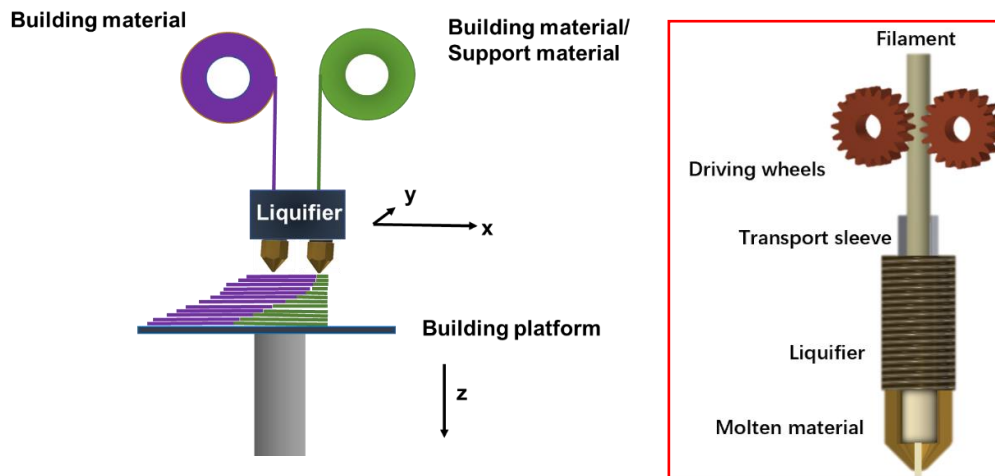


Figure 6: Schematic illustration of the printing principle of extrusion-based 3D printing (left). The filament is fed by driving wheels into liquifier, there melted and finally extruded through a nozzle (right).

When using a 3D printer offering dual extrusion nozzles, build filament material with another color or support filament material can be extruded alternately through the second nozzle. Sometimes for some complex geometric objects with huge cavities and steep overhangs, a support material is required to prevent deposited materials from collapsing or deformation. Typical support materials can be easily removed either mechanically or chemically. Compared with other 3D printing techniques like SLS and SL, extrusion-based 3D printing is a clean, simple and office-friendly 3D printing technique. Many thermoplastic components can be processed by extrusion-based 3D printers offering outstanding mechanical properties and moderate surface finishing. Normally, a certain surface roughness of a layered profile is obtained, which can be eliminated by post-treatment, e.g., solvent vapor bath [44–46]. The overall printed parts quality mainly depends on the materials, printer setups, and process parameters. The optimization of processing variables such as nozzle temperature, worktable temperature, as well as nozzle path and printing speed is crucial as they influence the performance of the final printed part (see **Chapter 1.2.2**) [47–49].

All extrusion-based 3D printers can be subdivided into three different price segments. The high-end segment is highly productive enterprise 3D printer system series designed for larger prototypes and end-use grade industrial productions. The middle-class segment is based on professional printers but with much smaller printing chamber volumes, which aim to realized ideas in design, manufacturing and marketing departments. They are also very productive and can produce printed parts of high quality after a precise optimization of printing variables, but usually realizable printing volumes are relatively smaller compared to the industrial

production-grade. The third class is the compact desktop or consumer 3D printer's class for artists and hobby makers. In recent years, lots of low-cost, compact, consumer-grade extrusion-based 3D printers were developed and are available on the market driven by the interest of many people who want to print their own imagination. This freedom of access to 3D printers is also the long-time goal of *Scott Crump*: "A reliable, capable, accurate, and easy to use a 3D printer on every engineer's desk". Nowadays, many consumer-grade extrusion-based 3D printer manufacturers in the USA, Europe, and even China want to participate on this new market. *MakerBot* (USA), *Ultimaker* (Netherland), *Raise3D* (China) has rapidly complemented their extrusion-based 3D printer production lines with colorful filaments and even easy-to-use 3D scanners [50–52]. Online shops of consumer 3D printer companies also provide personal 3D printing service, and interest people can share their ideas within the fans' community or even use cloud share. It is obvious that this new part of the extrusion-based 3D printing market will bring more benefits for both the 3D printer manufacturers and consumers. The ongoing competition to continually improve printing quality and reduce production prices will become even tougher in the future. Based on this well-developed technology and the availability of various thermoplastics, lots of innovative ideas are becoming realities utilizing extrusion-based 3D printing technology. However, for this technology, some issues due to layered production must still be addressed.

1.2.2. Challenges of extrusion-based 3D printing

In this chapter, drawbacks and issues of extrusion-based 3D printing technologies are discussed. Because of the layer by layer manufacturing principle, the optical (surface) and mechanical properties of printed objects are not quite equal to traditional injection molded or extruded ones. Thus, in this chapter, selected issues of extrusion-based 3D printing are reported.

Process concept induced anisotropic property

For extrusion-based 3D printing, there are many processing variables and material-dependent parameters that influence the printed part quality and performance, such as surface finishing, dimensional accuracy, and mechanical strength. For an easier understanding of important process variables, they are divided into two groups: (i) building strategy specific and (ii) print setting specific variables. For (i) building strategy specific variables, building initial direction, infill strategy including layer height, deposition orientation, infill pattern, and raster angle are the main variables, which can be defined in most common slicing software before 3D printing. The (ii) print setting specific variables include such as extrusion temperature, build platform temperature, extrusion flow rate, and print speed and can be controlled either before 3D printing by slicing software or during 3D printing via the interface of the printer. The most known issue using

extrusion-based 3D printing is related to all the process variables during production and referred to the anisotropic property.

For building strategy specific variables, for example, we want to print a tensile test specimen, a so-called dog-bone. As usual, we first have to draw the 3D sketch of the aimed dog-bone with CAD software, and then the obtained 3D dog-bone model has to be sliced into “printable” layer information, a G-code file, which can be read by every 3D printer. *Figure 7* (left) demonstrates the natural coordinate system X, Y, and Z-axes used in 3D printing systems: the layer building direction is along the Z-axis, and the layer deposition plane is defined by X and Y axes. Within the 3D coordinate system, there are numerous possibilities to set and print the dog-bone. Typically and intuitively, the dog bone is positioned orthogonal to the coordinate system. Therefore, the initial positions A, B, and C are shown in *Figure 7* (left), which represents the most typical building position for extrusion-based 3D printing. Due to the 3D printing of dog-bones in the different A, B, and C positions, the loading direction for mechanical testing of achieved dog-bones shows different angles concerning the printed layer deposition direction (*Figure 7* (right)). For a dog-bone printed in position A the layer deposition direction is vertical (90°) to the mechanical loading direction. In comparison, while for dog-bones printed in positions B or C, it is parallel (0°).

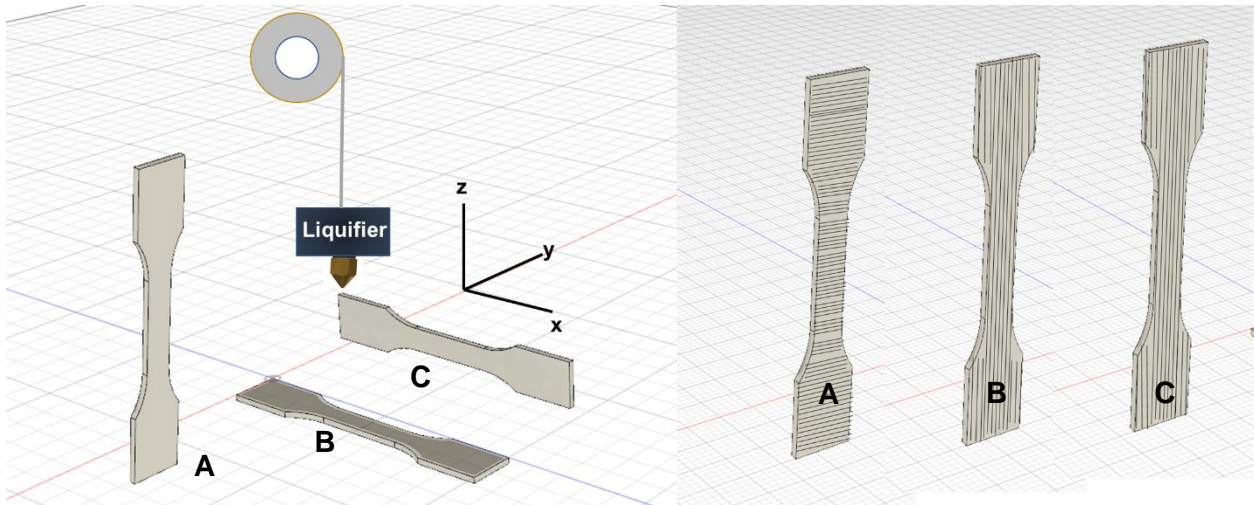


Figure 7: (left) Possible model orientations and (right) obtained layer orientation (fine black line in dog-bone) A, B, and C of dog-bone specimen processed by extrusion-based 3D printing. X, Y, and Z define the nature 3D coordinate

system used by 3D printing systems. The layer building direction is along Z-axis and the layer deposition plane is defined by X and Y axes.

To investigate the influence of the model orientation on the mechanical properties of printed part, Bagsik et.al printed three different dog-bone in each A, B, and C dog-bone orientations (*Figure 7* (left)) [48]. The obtained results of respective tensile measurements demonstrated significant differences of mechanical properties, which could be explained by different layer construction directions with respect to the tensile loading directions used for mechanical testing (*Figure 7* (right)). The specimens printed in the B and C direction show higher elongations at break because of the parallel material layer extrusion direction to the tensile load. The achieved properties are similar to injection-molded specimens. For the specimen 3D printed in the A orientation, a much earlier fracture was observed because of the 90° angle of layer deposition direction to tensile load. Here the interlayer bonding quality of the layered printed part was tested [48].

Not merely the different building orientation of a model, but also the other building strategy specific variables clearly influence the mechanical properties of a printed part. The layer deposition principle within one layer is usually printing first the contour of the current layer and then filling the inner area by a line pattern. For example, building orientation B is fixed; the layer deposition can still be realized in several ways (*Figure 8*). Different filled dog-bones result in obviously different mechanical properties because of the different mesostructures within the resulting printed part.

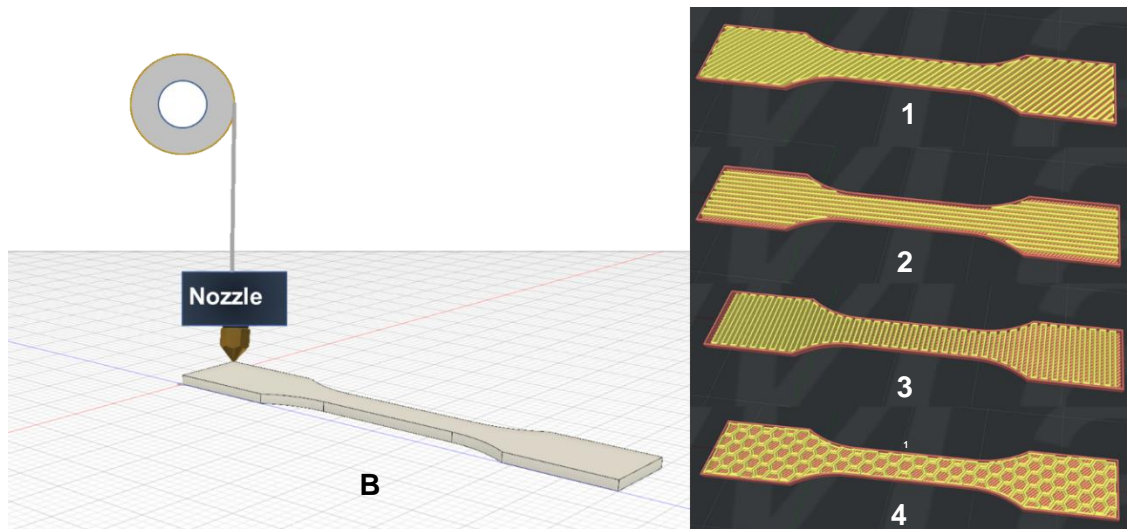


Figure 8: Illustration of different layer deposition strategies by printing a dog-bone oriented flat on the build surface (model orientation B, see Figure 7). Shown different infills strategies 1-4 result in different mechanical properties because of the anisotropic property of extrusion-based 3D printed objects.

Many scientific types of research have studied the anisotropic material properties of extrusion-based 3D printed objects caused by different deposition strategies [2,53–55]. In conclusion, besides material properties of used materials for extrusion-based 3D printing process variables such as extrusion width, filling density, filing angle, and printing temperature were identified as crucial variables. A series of samples was produced by extrusion-based 3D printing with various process variables and then the mechanical properties of the specimens evaluated. The results achieved showed that the variables of filling strategy are of major importance for resulting mechanical properties [56,57].

Besides the (i) building strategy specific variables, the (ii) print setting specific variables of extrusion-based 3D printing also have significant influences on the properties of a 3D printed part e.g., extrusion and printer chamber temperature and printing speed [2]. Temperature and speed variables influence the thermal history and molecular diffusion of the extruded material, which are important for the bonding mechanism during the 3D printing process. This observation indicates that all temperature settings on the utilized 3D printer are critical variables affecting the printed part properties (see also **Chapter 1.2.2 Bonding mechanism induced anisotropic property**). In this context, the Design of experiment (DoE) is a recommended tool for systematic and efficient optimization of concurrent, multiple, and interacting variables.

Bonding mechanism induced anisotropic property

Besides the process variables, the origin of the anisotropic property also results in the special layer construction and layer bonding mechanism of extruded polymer lines during extrusion-based 3D printing [47]. In the case of polymer extrusion or injection molding, the polymer is molded or extruded at the isotropic molten state and subsequently cooled to obtain its shape. In contrast, extrusion-based 3D printers deposit melted polymer lines with relatively insufficient residual thermal energy to fuse entirely with lines of the previously deposited layer underneath. Due to this unique layered fabrication concept, the successively deposited material lines are fused together by thermal energy and mechanical pressure of the moving hot nozzle during printing [10]. A special material bonding and fusion process take place driven by thermal energy [47,58,59]. The formation of the bonding among extruded polymer lines in extrusion-based 3D printed parts is mainly achieved by homopolymer mixing and polymer chain diffusion of extruded molten material [2,47]. The history of temperature at interfaces among the deposited lines plays a crucial role in the bonding quality, and thus, the mechanical properties of the final printed part [60]. The bonding quality is influenced by the diffusion and mixing of polymer chains across the interface [2,47]. Thus, a higher extrusion temperature and higher printer chamber temperature should delay the cooling of extruded lines and therefore result in an enhanced bonding between printed lines. Besides the print setting specific variables, the inherent properties of used material itself, such as thermal conductivity, specific heat capacity,

and viscosity, also influence the bonding quality, which is also extensively discussed by the polymer welding theory [61,62]. *Figure 9* shows the fundamental difference between an injection molded part and an extrusion-based 3D printed one. Here, the extrusion-based 3D printed part shows the obtained mesostructures consist of many partially fused material lines.

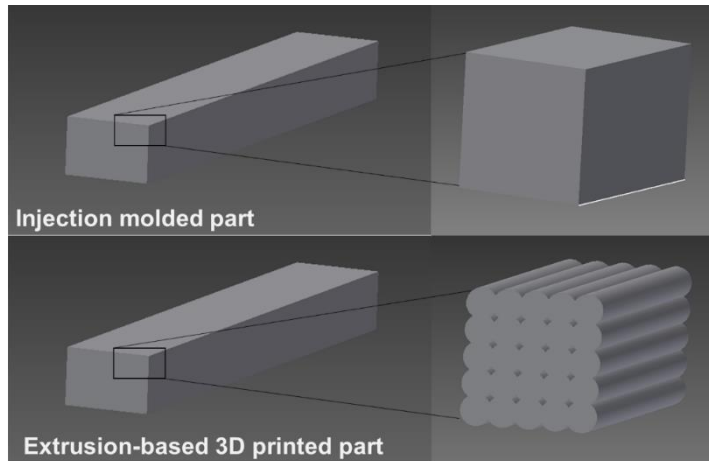


Figure 9: Specimens prepared by injection molding (upper sketch) and extrusion-based 3D printing (lower sketch). The injection-molded part shows isotropic mechanical properties, while the extrusion-based 3D printed part shows anisotropic properties due to the mesostructures of extruded, partially fused, and oriented material lines.

The resulting interface of fused lines is always the critical area of extrusion-based 3D printed parts caused by limited polymer chain intermixing and reduced formation of entanglements or crystals at this interface within the short time period of the melted state. Thus, the resulting interface bonding quality, which is mainly controlled by the thermal history of each extruded line [63,64]. For example, ABS extrusion-based 3D printed parts show at most 80% of the strength of solid ABS parts produced by injection modeling, and the properties mainly depend on the filling strategies. Compared with injection molding, the extrusion-based 3D printed part exhibits an anisotropic mechanical property [65,66]. A mesostructured extrusion-based 3D printed part consists of three different structural elements. The first is the bulk area of deposited material lines; this part is typically isotropic. The second part is the contact areas where the bonding or fusing of deposited lines is situated; this part is usually anisotropic with different bonding qualities that depend on achieved bonding area sections (lines are bonded vertically to upper and lower lines or bonded horizontally to adjacent lines). The third part is the air voids among all deposited lines. In comparison to injection molded parts, the produced bonding areas and existing air voids influence the mechanical properties and thus result in the anisotropic mechanical property of extrusion-based 3D printed parts.

Warp deformation and shrinkage

A further major issue doing extrusion-based 3D printing is the part warp deformation and shrinkage. Compared with injection molding, where mold pressure and cooling system are optimized to produce accurate part dimensions within a very short time, extrusion-based 3D printed parts are prepared without any mold. The aimed object is produced layer by layer by executing a digital file [67,68]. The melted and extruded thermal plastic material is deposited, fused, cooled, and solidified layer by layer to form a freestanding part. Its shape and dimension are obtained without any external holding pressure or material compensation dealing with shrinkage. Since the material was heated over the melting point for the extrusion through the nozzle and cools to printer chamber temperature for solidification, a material shrinkage is inevitable. The shrinkage induced inner stresses during the cooling of the deposited material affects the printed part size dimensions and could lead to part warp, inner-layer delaminating or cracking, and even production failure [10]. Reducing the warpage and improving the shape accuracy of the 3D printed parts is beside the anisotropic property, one of the most important topics in extrusion-based 3D printing.

1.3 Polymers for extrusion-based 3D printing

1.3.1 Commonly used thermoplastic materials

Thermoplastics are polymer materials that can be melt-processed several times or re-casted by utilizing their melting and re-solidification properties [69,70]. The thermoplastic market occupies over 10 % of the global market in the chemical industry and over 90 % of all polymer materials. In addition, the thermoplastic market belongs to the most rapidly growing part of the world economy. Nowadays, a new driving force for the blooming of thermoplastic development is occurring due to the emergence of revolutionary technologies: 3D printing technologies [71,72]. For example, SLS sinters and extrusion-based 3D printing melts the applied materials to produce objects layer by layer. Therefore, thermoplastics are ideal material candidates and provide a wide range of mechanical and chemical properties. Typically used feedstock materials are powdered materials with the particle size of 50 μm for SLS and filaments with diameters of 1.75 mm or 2.85 mm for extrusion-based 3D printing, which are similar to standard plastic welding sticks [73–77]. Thermoplastic polymeric materials can be divided into three different classes according to their performance: commodity plastics, engineering plastics, and high-performance plastics, which are assembled systematically in the pyramid of thermoplastic materials. This pyramid could be further divided into two hemi-pyramids consisting of amorphous and semi-crystalline polymeric materials (*Figure 10* (left)). *Figure 10* (right) summarizes commercially available thermoplastics used for extrusion-based 3D printing.

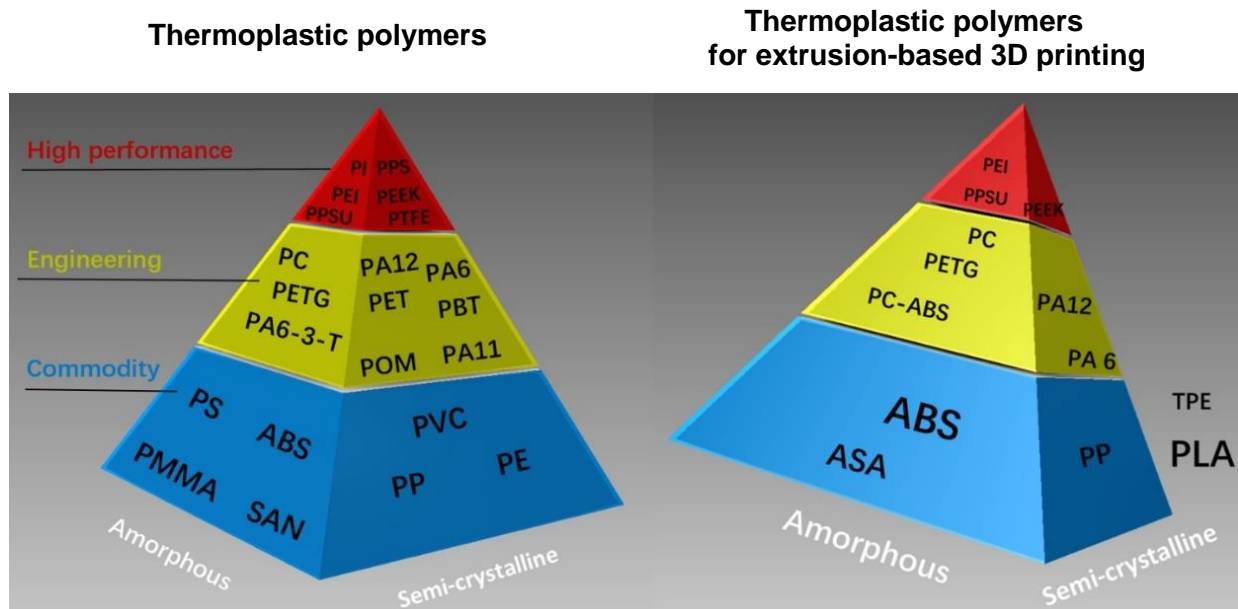


Figure 10: Pyramid of thermoplastic materials (left) and availability of the materials as filaments for extrusion-based 3D printers (right).

The most widely used thermoplastics for extrusion-based 3D printing are ABS, PLA, Nylon, and some high-performance polymers [2,54,78,79]. Acrylonitrile butadiene styrene (ABS) and their blends with other polymers are the most used extrusion-based 3D printing material, suitable for various applications [2,53,80–82]. ABS printed parts are very accurate, and printed details are at a moderate level. Normally it shows some warpage by printed parts and requires a heated printer chamber or at least a heated printer bed at around 100 °C [10]. Polylactide (PLA) is the most popular extrusion-based 3D printing material. Compared with other polymers, PLA offers much less warpage [54,69,83–85]. It can be successfully printed without the need for a heated printer bed or chamber [86,87]. If actively cooled, much sharper details can be realized on printed corners without any interlayer cracking or warping. In addition, PLA is also environmentally friendly and biodegradable, but due to its low service temperature range (below 60°C), PLA is defined as thermoplastic semi-crystalline aliphatic polyester but not in the group of commodity polymers [88,89]. Polyamide (PA or Nylon) and Polycarbonate (PC) are typically used for more sophisticated parts, such as conceptual parts, small series of parts and functional parts due to their excellent mechanical properties [79,90,91]. Some other thermoplastics like PEEK (Polyetheretherketone), ULTEM (PEI, Polyetherimide), and PPSU (Polyphenylsulfone) with outstanding mechanical properties and high-temperature resistance are 3D printed in some special applications such as automobile and aerospace industry or in the medical sector [23,48,55,78].

For all thermoplastics, commodity plastics are used in the largest quantities due to their cost-effectiveness in combination with mid-range mechanical properties [71]. Most notably, polyethylene (PE), polypropylene (PP), poly(vinyl chloride) (PVC), and their copolymers are used as commodity plastics and constitute already more than 50% of total thermoplastic materials consumption [69]. However, typical commodity plastics have not been favored for extrusion-based 3D printing due to the relatively high material-related crystallinity. Already discussed in **Chapter 1.2.2**, for extrusion-based 3D printing, the melted polymer is extruded through a nozzle and deposited on the build platform layer by layer. After deposition, the material is cooled down from extrusion temperature (above melting temperature T_{melt}) to the printing chamber temperature T_{chamber} and to room temperature T_{room} after the completion of the print. This temperature difference leads to a significant specific volume shrinkage. Preferred materials should feature less material shrinkage to offer high part dimensional accuracy and less fabrication failure. Here, typical semi-crystalline thermoplastics show a relatively high volumetric shrinkage when compared with amorphous polymers. Based on studies of Wang et al. the shrinkage-induced warpage depends on the nature and properties of the utilized materials, especially with regard to shrinkage coefficient and stiffness [10,92]. Amorphous polymers such as ABS, PC (polycarbonate), or PETG (poly(ethylene terephthalate) glycol-modified) exhibit a more linear and less steep decrease of the specific volume during cooling. While the drop of the specific volume due to the crystallization of semi-crystalline polymers leads typically to extensive warpage of 3D

printed part [92,93]. *Figure 11* shows the typical specific volume change of amorphous and semi-crystalline polymers from extrusion temperature to room temperature [94].

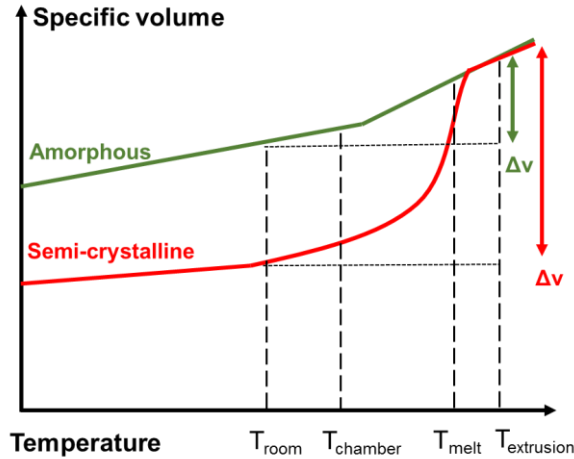


Figure 11: Schematic graphic plot of typical specific volume course of amorphous and semi-crystalline polymers as a function of temperature. The change of specific volume of the amorphous polymer (green line) shows a kink at the glass transition temperature, while of semi-crystalline polymer (red line) shows a clear step at the melting range. (Figure 11 modified from reference [94])

However, most of the amorphous thermoplastics exhibit compared with semi-crystalline thermoplastic relative low toughness, a small range of service temperatures, and low chemical resistance. In consequence, more and more semi-crystalline polymers are in the focus of the scientific investigation to improve their printed part performances. In addition, the formed crystals at the bonding interface play an important role in the extrusion-based 3D printed part as they could increase interlayer bonding strength [2,95] (*Figure 12*).

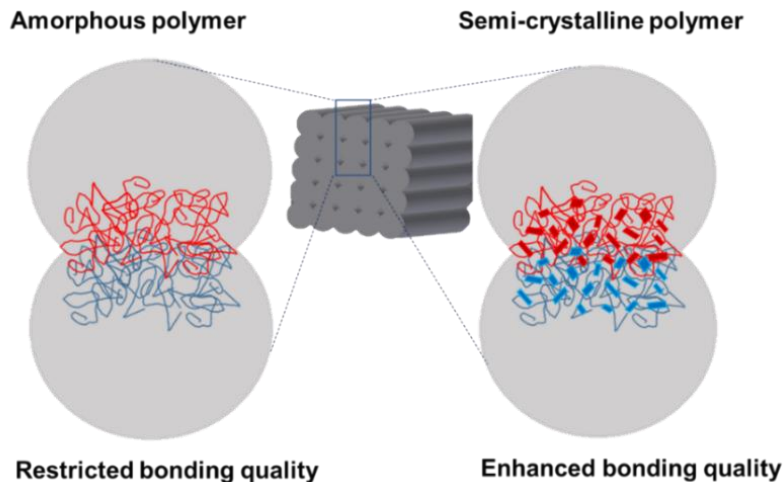


Figure 12: Schematic illustration of the bonding interface area of 3D printed lines of an amorphous (left) and a semi-crystalline (right) polymer. Semi-crystalline polymers gain interface reinforcement thanks to their thermally reversible crosslinks caused by crystals at the interface, which results in enhanced interlayer bonding quality. (Figure 12 inspired and further developed from reference [47])

Already talked in **Chapter 1.2.2**, the interface of fused lines is always the most critical area of extrusion-based 3D printed parts, which results in anisotropic properties. Therefore, a balance between bonding strength and part shrinkage should be optimized. Nylon 12 is a good example with the balance of high bonding strength and less part shrinkage [96]. However, for the most widely used commodity material PE and PP, tailored modifications and optimizations are still required to achieve filaments offering a high performance of 3D printed parts.

1.3.2 Polypropylene for extrusion-based 3D printing

In **Chapter 1.3.1**, the overview of thermoplastic for FFF (extrusion-based 3D printing) is given with the help of the pyramid of thermoplastic materials. Recently, commercially available thermoplastics materials for FFF have increased considerably, e.g., PP based FFF material. Among the all commodity thermoplastics in ground flow, polypropylene (PP) is the most common semi-crystalline thermoplastic applied in consumer and technical products due to its exceptional mechanical properties, processing ability, and low cost. In addition, through copolymerization as well as by compounding with additives and fillers, PP can be successfully modified and tailored for various applications and is promising for FFF [97–103]. However, PP based FFF materials always faced shrinkage and layer adhesion issue, in the year 2014, the first commercial PP filament was released with unperfect printing results [104,105]. The main disadvantage of PP in extrusion-based 3D printing is the strong shrinkage induced warp part deformation. As semi-crystalline PP melt comes out from extrusion-based 3D printing hot nozzle and cools down, the specific volume of the polymer decreases due to the crystallization process forming dense crystal structures [92,106–108]. Shrinkage induced contractile force results in residual inner stresses and excessive part warpage. Additionally, because of the poor adhesion ability of PP to typically used build platforms, extrusion-based 3D printed PP parts also tend to detach easily from platforms due to contractile force and thus lead to printing failures [94,109–111]. More and more research studies have focused on extrusion-based 3D printing utilizing PP and tried to address and solve the issues. All the previous studies could be divided into two groups, in one the focus was on the investigation of process variables and in the other, the optimization of PP filament materials.

Firstly, the process variables are discussed. Several studies focused on the optimization of process variables for solving the printed part warpage issue. Printing platform, printing chamber, and extrusion temperature, which have an influence on the thermal history of extruded lines, are identified as the most crucial process variables for the warpage as well as for mechanical properties optimization [94,112,113]. All these factors influence temperature distribution and temperature gradient within and between printed lines. Therefore, a higher chamber temperature results in an improved dimensional accuracy due to the lower specific volume

decrease and less inner stress due to softened material [87,107]. Another solution is to modify the CAD data or slice data with optimized interior infill design, e.g., frequent changes of directions and a higher number of layers [10]. Due to the restricted adhesion of the first printed layer to common build platforms, an improved PP adhesion on more tailored platforms would lead to reduced warpage [109,110,114]. In this context, a promising novel build platform designed for extrusion-based 3D printing utilizing polyolefin has recently become commercially available [115].

For PP material optimization, Carneiro et al. were the first to investigate the printability and mechanical property of glass-fiber-filled injection molding grade isotactic polypropylene (iPP). From printed parts, high shrinkage and warpage were observed [73]. After that, many studies on various fillers or fibers for extrusion-based AM have been reported with improved mechanical, rheological, or thermal properties [116,117]. However, only a few of them focused on reducing the warpage of 3D printed parts. Wang et al. studied the crystallization kinetics of iPP by adding spray-dried cellulose nanofibrils (SDCNF) targeting retarding the crystallization rate and lowering the degree of crystallization for reduced warpage [118]. The authors claimed that the degree of crystallization is critical for semi-crystalline polymers inspired by applied PLA filament grades with a very low degree of crystallization, which exhibit almost no warp and shrinkage. However, even after adding different amounts of SDCNF, the achieved reduction of crystallization rate and the corresponding degree of crystallization indicates that the decrease in material shrinkage is mainly due to the low degree of crystallization [118]. As for material optimization of feedstock filaments typically a high amount of novel developed materials is required for the production, we developed an effective screening method utilizing injection-molded short rods and 3D printed square tube specimens [105]. Applying this screening method, we investigated several iPP, polypropylene-ethylene random copolymers (raco PP), and PP/PE blends. As a result, the geometric deformation was reduced with decreasing crystallinity, indicating that raco PP, with its lower degree of crystallinity, causes less warpage. The lower degree of crystallinity is due to the ethylene co-units, making these PP grades very promising for extrusion-based 3D printing [105,119,120]. Based on this knowledge, *Spoerk* et al. selected a raco PP grade with a low degree of crystallization as base PP material for many of their studies [106,110,121–124]. In addition, *Spoerk* et al. optimized the shrinkage of used raco PP by adding expanded spherical perlite fillers and also one amorphous polyolefin to reduce the brittleness of produced filaments. By adding increased contents of the inorganic expanded spherical perlite filler, the volumetric shrinkage clearly decreases. As the topically modified fillers are homogeneously distributed in the polymer matrix, they support internal stress adsorption results in decreased warpage. Not only spherical filler but also short carbon fibers demonstrated outstanding warpage reduction [124]. However, although the fillers and fibers managed to decrease part shrinkage, negative effects due to the high contents such as complex crystallization kinetic, reduced maximum tensile strength, and shortened elongation of modified raco PP filaments were also observed [106,122,123].

For further lowering the degree of crystallization and eliminating the side effects of incorporated inorganic fillers, PP crystal structure modification or PP blending with polyolefins seems to be a promising way to decrease the geometric deformation of 3D printed parts [10,105,106,125,126]. Amorphous PP (aPP) or amorphous polyolefins can be blended in a wide range with isotactic PP as a softening agent, and therefore they can be used to tailor the properties of PP blends [114,125,127]. Following a similar principle, ethylene-containing PP copolymers or PP blends with polyethylene (PE) are also used to improve the performance of PP [106,128]. Additives such as clarification and nucleation agents are very popular in the industry to improve the optical and mechanical properties of PP [129–132]. Among the different known modifications of polypropylene in relation to the crystalline form, the monoclinic α and the hexagonal β modifications draw the most attention in both scientific research and industrial applications [130,132–134]. The α form is the most common modification under regular crystallization conditions, while the β crystal form is observed in the presence of β -nucleating agents or after applying a special cooling and processing condition [129,132,135,136]. Compared to the α -phase, the β -phase is tougher but less dense and stiff [137,138]. For extrusion-based 3D printing materials, lower stiffness and density of formed crystals could reduce the inner stress caused by material shrinkage upon cooling [10] and thus may lead to enhanced printing performance [10,130,132,135,139,140]. Some studies have reported preliminary results of incidentally observed β -PP crystals obtained in extrusion-based 3D printed parts due to special thermal conditions during the printing process. However, a systematic study of the influence of β -form crystals on shrinkage was still missing [112,122,141]. As a summary, the influence of additives and fillers are well investigated on PP for improving the warp and shrinkage. Nevertheless, a detailed investigation of the critical interlayer bonding quality was still missing for PP. Thanks to the semi-crystalline nature of PP, a high isotropic property is expected due to formed crystallites at line interfaces during layer bonding. However, an effective and reliable evaluation method to report the interlayer bonding strength has to be developed first and established.

1.4 Smart material for 4D printing

In **Chapter 1.1.3**, the hype cycle is explained with an outlook on 3D printing technology. Here, 4D printing emerged in the year 2018. Besides obtained mechanical isotropy and dimensional accuracy of the extrusion-based 3D printed part, one category of materials is in the spotlight for 3D printing as they offer distinct advantages: smart materials. By applying smart materials for 3D printing a new term was created: ‘4D printing’ [36,37,39,40,142,143].

Shape memory polymers (SMPs) are a highly interesting class of smart materials that are defined as polymers that can memorize and recover from a temporary fixed shape to a programmed original shape under appropriate conditions [83,144]. 3D printing of SMPs provides 4D printing with high strain recovery, low cost, and simple programming by 3D printing. Moreover, SMPs can also be modified chemically to achieve further applications [145]. A trigger (temperature, pH, moisture, etc.) is necessary to allow the transformation from the temporary shape to the programmed original shape [145,146]. As the shape memory is often a thermally induced process, these materials are called thermosensitive SMPs [146]. For the shape memory effect, three requirements are important: (i) crosslinks acting as fixation of the original shape, and (ii) a second type of physical crosslinks acting as defeasible fixation of the temporary shape allowing the reversible switching, and (iii) a certain degree of elasticity as shape recovery driving force [147,148]. The first type of crosslinks could be either chemically (covalent bonds) or physically (intermolecular interactions) [146]. Chemically crosslinked SMPs can be achieved by crosslinking chemistry to form thermoset polymers [146]. For physical crosslinks, SMPs require a polymer morphology that consists of at least two separated domains, e.g., a crystalline and an amorphous phase. Another polymer morphology with physical crosslinks is present in $(AB)_n$ segmented copolymers and thermoplastic elastomers. Here, segments of copolymer chain form separated domains (hard segments) act as crosslinks and break (dissemble) at an elevated temperature ($T_{\text{trans,(high)}}$). For shape switching, a second type of reversible physical crosslinking is needed at a lower temperature ($T_{\text{trans,(low)}}$). This transition is important for the fixation of the temporary shape. The transition at $T_{\text{trans,(low)}}$ can be either melting/crystallization (T_m) or glass transition (T_g) of domains formed by the more flexible segments. Thus, heating above $T_{\text{trans,(low)}}$, a certain elasticity is reached, and in combination with stored inner energy, the transformation from temporary shape to original shape occurs. Therefore, these domains are often called switching domains [148]. A good SMP example is the thermoplastic polyurethane (TPU), a typically segmented block copolymer with microphase separation from alternating sequences of hard and soft segments [149]. When the temperature goes up above the glass transition temperature (T_g) of the soft segment, the polymer is in a rubber-like and elastic state and could be easily deformed. If the temperature goes down below this T_g , the deformed shape will be retained until the temperature rises higher than T_g again. Here, the frozen elastic energy will be released and act as shape recovery driving force [40].

Another possibility is the dual-component blend of Poly(ϵ -caprolactone) (PCL) and TPU (based on PCL-diol), here the switch domain is formed by the crystalline phase of PCL with the trigger of reversible melting and crystallization of PCL chain segment [40,83,149]. *Figure 13* shows a schematic illustration of a SMP consists of crystallized flexible segment chains (blue) forming the reversible switching domain. Here, the shape transition temperature $T_{\text{trans.}(low)}$ is the melting and crystallization temperature of flexible segment chains. When heating over $T_{\text{trans.}(low)}$, the sample could be shape transformed by applying a force. By cooling down below $T_{\text{trans.}(low)}$, this temporary shape can be fixed. Because of the existing crosslinks of the hard segment domains (red), restoring energy is stored due to the elastic deformation. Then, if the transformed shape is heated again over $T_{\text{trans.}(low)}$, the crystallized flexible segments are again melted, the stored energy is released, which drives the sample to return it to its programmed original shape [150].

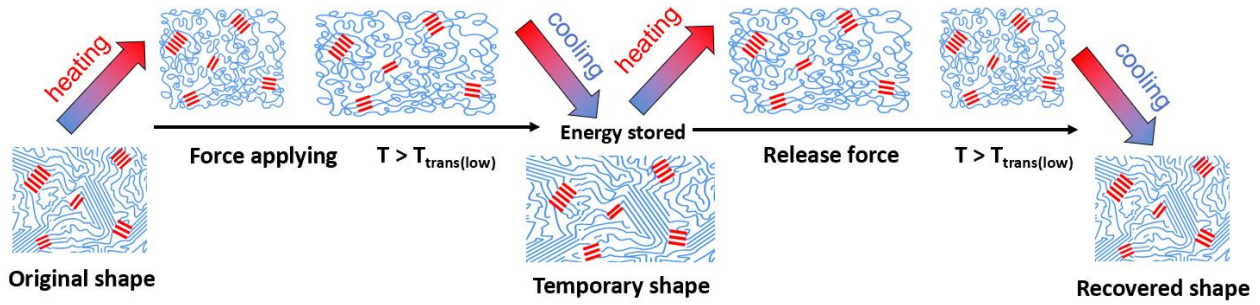


Figure 13: Schematic illustration of phase transitions during 4D printing of a shape memory polymer with crystallizable flexible chain segments as switching domain (blue). The hard segments (red) act as higher thermally stable crosslinks and fix the original shape (Figure 13 inspired and further developed from reference [150]).

In recent years, many research activities have been reported on 4D printing utilizing, e.g., TPU materials in combination with extrusion-based additive manufacturing [40,142]. However, the feeding issue of soft materials by extrusion-based 3D printing could not be ignored. Elkins et al. firstly reported the feeding issue of a soft thermoplastic elastomer [151]. However, using such soft filament materials is a big challenge for feeding systems of 3D printers. The low stiffness combined with a high melt viscosity can cause filament buckling [151]. For pharmaceutical and drug delivery materials, the obtained filaments are often too soft to be extrusion-based 3D printed [151,152]. Several previous studies indicate that stiffness, hardness, and melt viscosity of soft materials are very critical to processability in extrusion-based 3D printers [105,153]. Consequently, TPU based soft SMP with higher stiffness and a certain hardness, e.g., two-component systems with crystalline switching domain, show clear advantages for 3D and 4D printing. In this context, Visser et al. firstly synthesized copolyetherimides consisting of pyromellitic dianhydride and amino-functionalized poly(ethylene glycol) (PEG) aiming at creating polyurethane-like polymers with enhanced chemical and thermal stability [153]. Polyimides exhibit excellent thermal stability and mechanical,

chemical, and electrical properties, which make polyimides applicable in a wide range of applications such as microelectronics, adhesives, biomaterials, aerospace, and solar cells [154–157]. The incorporated PEG segments should act as soft segments, while the polyimide units formed the hard segments due to the π - π interactions. However, the PEG segment with a longer chain length exhibited low elasticity because of the crystallization of these PEG segments [153]. A further TPU-like polyimide was synthesized utilizing perylene-3,4,9,10-tetracarboxylic dianhydride and poly(ethylene glycol) or poly(propylene glycol) based diamines. The photochemical properties of perylene segments and increased solubility of these flexible spacers, allowed the application of copolymers in the research field of organic photovoltaics [158–162]. Based on this knowledge, in this work, aimed at 3D and 4D printing, perylene imide segments should act as reversible physical crosslinks disassembling at elevated temperatures while the PEG segments should be semi-crystalline at room temperature and melt around 50 °C to enable shape switching. In addition, the crystallinity of PEG segments should improve the filament quality concerning the feeding issue in extrusion-based 3D printing.

1.5 Reference

Reference list

- [1] S. Upcraft and R. Fletcher, “The rapid prototyping technologies,” *Assembly Automation*, vol. 23, no. 4, pp. 318–330, 2003.
- [2] S. - H. Ahn, M. Montero, D. Odell et al., “Anisotropic material properties of fused deposition modeling ABS,” *Rapid Prototyping Journal*, vol. 8, no. 4, pp. 248–257, 2002.
- [3] P. Afonso, M. Nunes, A. Paisana et al., “The influence of time-to-market and target costing in the new product development success,” *International Journal of Production Economics*, vol. 115, no. 2, pp. 559–568, 2008.
- [4] I. Gibson, D. Rosen, and B. Stucker, *Additive manufacturing technologies: 3D printing, rapid prototyping and direct digital manufacturing*, Springer, New York, Heidelberg, Dodrecht, London, 2015.
- [5] P. Dudek, “FDM 3D Printing Technology in Manufacturing Composite Elements,” *Archives of Metallurgy and Materials*, vol. 58, no. 4, 2013.
- [6] D. T. Pham and S. S. Dimov, “Rapid Prototyping Processes,” in *Rapid Manufacturing*, D. T. Pham and S. S. Dimov, Eds., vol. 9, pp. 19–42, Springer London, London, 2001.
- [7] Alkhair A. Mousa, “The Effects of Content and Surface Modification of Filler on the Mechanical Properties of Selective Laser Sintered Polyamide12 Composites,” *Jordan Journal of Mechanical and Industrial Engineering*, vol. 8, no. 5, pp. 265–274, 2014.
- [8] F. Klocke, T. Celiker, and Y. - A. Song, “Rapid metal tooling,” *Rapid Prototyping Journal*, vol. 1, no. 3, pp. 32–42, 1995.
- [9] D.T. Pham and R.S. Gault, “A comparison of rapid prototyping technologies,” *International Journal of Machine Tools and Manufacture*, vol. 38, 10-11, pp. 1257–1287, 1998.
- [10] T.-M. Wang, J.-T. Xi, and Y. Jin, “A model research for prototype warp deformation in the FDM process,” *The International Journal of Advanced Manufacturing Technology*, vol. 33, 11-12, pp. 1087–1096, 2007.
- [11] K. Renap and J. P. Kruth, “Recoating issues in stereolithography,” *Rapid Prototyping Journal*, vol. 1, no. 3, pp. 4–16, 1995.
- [12] P. F. Jacobs, *Rapid prototyping & manufacturing: Fundamentals of stereolithography*, Published by Society of Manufacturing Engineers, in cooperation with the computer and Automated Systems Association of SME; McGraw-Hill, Dearborn, MI, New York, 1993], 1992.

- [13] R. Januszewicz, J. R. Tumbleston, A. L. Quintanilla et al., “Layerless fabrication with continuous liquid interface production,” *Proceedings of the National Academy of Sciences of the United States of America*, vol. 113, no. 42, pp. 11703–11708, 2016.
- [14] J. R. Tumbleston, D. Shirvanyants, N. Ermoshkin et al., “Additive manufacturing. Continuous liquid interface production of 3D objects,” *Science (New York, N.Y.)*, vol. 347, no. 6228, pp. 1349–1352, 2015.
- [15] E. Sachs, M. Cima, J. Cornie et al., “Three-Dimensional Printing: The Physics and Implications of Additive Manufacturing,” *CIRP Annals - Manufacturing Technology*, vol. 42, no. 1, pp. 257–260, 1993.
- [16] P. Calvert, “Materials science. Printing cells,” *Science (New York, N.Y.)*, vol. 318, no. 5848, pp. 208–209, 2007.
- [17] B. Guillotin and F. Guillemot, “Cell patterning technologies for organotypic tissue fabrication,” *Trends in biotechnology*, vol. 29, no. 4, pp. 183–190, 2011.
- [18] N. E. Fedorovich, W. Schuurman, H. M. Wijnberg et al., “Biofabrication of osteochondral tissue equivalents by printing topologically defined, cell-laden hydrogel scaffolds,” *Tissue engineering. Part C, Methods*, vol. 18, no. 1, pp. 33–44, 2012.
- [19] J. Reynolds and N. Diaz, “Heart Models in 3D Print,” in *VII Latin American Congress on Biomedical Engineering CLAIB 2016, Bucaramanga, Santander, Colombia, October 26th -28th, 2016*, I. Torres, J. Bustamante, and D. A. Sierra, Eds., vol. 60, pp. 537–540, Springer Singapore, Singapore, 2017.
- [20] B. P. Conner, G. P. Manogharan, A. N. Martof et al., “Making sense of 3-D printing: Creating a map of additive manufacturing products and services,” *Additive Manufacturing*, 1-4, pp. 64–76, 2014.
- [21] B. Westerweel, R. J.I. Basten, and G.-J. van Houtum, “Traditional or Additive Manufacturing? Assessing Component Design Options through Lifecycle Cost Analysis,” *European Journal of Operational Research*, vol. 270, no. 2, pp. 570–585, 2018.
- [22] H. Saijo, K. Igawa, Y. Kanno et al., “Maxillofacial reconstruction using custom-made artificial bones fabricated by inkjet printing technology,” *Journal of artificial organs : the official journal of the Japanese Society for Artificial Organs*, vol. 12, no. 3, pp. 200–205, 2009.
- [23] S. C. Joshi and A. A. Sheikh, “3D printing in aerospace and its long-term sustainability,” *Virtual and Physical Prototyping*, vol. 10, no. 4, pp. 175–185, 2015.
- [24] S.-J. Jung and T.-H. Lee, “Study of Trends in The Architecture and The Economic Efficiency of 3D Printing Technology,” *Journal of the Korea Academia-Industrial cooperation Society*, vol. 15, no. 10, pp. 6336–6343, 2014.
- [25] Cotteleer, M., & Joyce, J., *Cotteleer, Mark, and Jim Joyce. "3D opportunity: Additive manufacturing paths to performance, innovation, and growth,* 2014.

- [26] M. Kreiger and J. M. Pearce, "Environmental Life Cycle Analysis of Distributed Three-Dimensional Printing and Conventional Manufacturing of Polymer Products," *ACS Sustainable Chemistry & Engineering*, vol. 1, no. 12, pp. 1511–1519, 2013.
- [27] K. Zhou, T. Liu, and L. Zhou, "Industry 4.0: Towards future industrial opportunities and challenges," in *2015 12th International Conference on Fuzzy Systems and Knowledge Discovery (FSKD)*, pp. 2147–2152, IEEE, 2015/8/15 - 2015/8/17.
- [28] J. Mai, L. Zhang, F. Tao et al., "Customized production based on distributed 3D printing services in cloud manufacturing," *The International Journal of Advanced Manufacturing Technology*, vol. 84, 1-4, pp. 71–83, 2016.
- [29] F. Almada-Lobo, "The Industry 4.0 revolution and the future of Manufacturing Execution Systems (MES)," *Journal of Innovation Management*, vol. 3, no. 4, pp. 16–21, 2016.
- [30] Gartner Research, "Gartner Hype Cycle: Interpreting technology hype"
<https://www.gartner.com/en/research/methodologies/gartner-hype-cycle>.
- [31] D. E. O'Leary, "Gartner's hype cycle and information system research issues," *International Journal of Accounting Information Systems*, vol. 9, no. 4, pp. 240–252, 2008.
- [32] Gartner Research, "Hype Cycle for Emerging Technologies 2011,"
<https://www.gartner.com/en/documents/1754719/hype-cycle-for-emerging-technologies-2011>.
- [33] M. Paulic, T. Irgolic, J. Balic et al., "Reverse Engineering of Parts with Optical Scanning and Additive Manufacturing," *Procedia Engineering*, vol. 69, pp. 795–803, 2014.
- [34] Gartner Research, "Hype Cycle for Emerging Technologies 2014"
<https://www.gartner.com/en/documents/2809728/hype-cycle-for-emerging-technologies-2014>.
- [35] Gartner Research, "5 Trends Emerge in the Gartner Hype Cycle for Emerging Technologies, 2018,"
<https://www.gartner.com/smarterwithgartner/5-trends-emerge-in-gartner-hype-cycle-for-emerging-technologies-2018/>.
- [36] Z. X. Khoo, J. E. M. Teoh, Y. Liu et al., "3D printing of smart materials: A review on recent progresses in 4D printing," *Virtual and Physical Prototyping*, vol. 10, no. 3, pp. 103–122, 2015.
- [37] S. K. Leist and J. Zhou, "Current status of 4D printing technology and the potential of light-reactive smart materials as 4D printable materials," *Virtual and Physical Prototyping*, vol. 11, no. 4, pp. 249–262, 2016.
- [38] M. Zarek, M. Layani, I. Cooperstein et al., "3D Printing of Shape Memory Polymers for Flexible Electronic Devices," *Advanced materials (Deerfield Beach, Fla.)*, vol. 28, no. 22, pp. 4449–4454, 2016.
- [39] Q. Ge, A. H. Sakhaei, H. Lee et al., "Multimaterial 4D Printing with Tailorable Shape Memory Polymers," *Scientific reports*, vol. 6, p. 31110, 2016.

- [40] M. D. Monzón, R. Paz, E. Pei et al., “4D printing: processability and measurement of recovery force in shape memory polymers,” *The International Journal of Advanced Manufacturing Technology*, vol. 89, 5-8, pp. 1827–1836, 2017.
- [41] A. S. Gladman, E. A. Matsumoto, R. G. Nuzzo et al., “Biomimetic 4D printing,” *Nature materials*, vol. 15, no. 4, pp. 413–418, 2016.
- [42] A. Lendlein and R. Langer, “Biodegradable, elastic shape-memory polymers for potential biomedical applications,” *Science (New York, N.Y.)*, vol. 296, no. 5573, pp. 1673–1676, 2002.
- [43] C. K. Chua, K. F. Leong, and C. S. Lim, *Rapid prototyping*, World Scientific Publ. Co, New Jersey, 2004.
- [44] B. Graybill, *Development of a Predictive Model for the Design of Parts Fabricated by Fused Deposition Modeling: Master Thesis*, 2010.
- [45] A. Garg, A. Bhattacharya, and A. Batish, “On Surface Finish and Dimensional Accuracy of FDM Parts after Cold Vapor Treatment,” *Materials and Manufacturing Processes*, vol. 31, no. 4, pp. 522–529, 2016.
- [46] A. Garg, A. Bhattacharya, and A. Batish, “Chemical vapor treatment of ABS parts built by FDM: Analysis of surface finish and mechanical strength,” *The International Journal of Advanced Manufacturing Technology*, vol. 89, 5-8, pp. 2175–2191, 2017.
- [47] Q. Sun, G. M. Rizvi, C. T. Bellehumeur et al., “Effect of processing conditions on the bonding quality of FDM polymer filaments,” *Rapid Prototyping Journal*, vol. 14, no. 2, pp. 72–80, 2008.
- [48] A. Bagsik, V. Schöppner, and E. Klemp, “FDM part quality manufactured with Ultem* 9085,” *14th international scientific conference on polymeric materials*, Vol. 15, 2010.
- [49] A. S. El-Gizawy, S. Corl, and B. Graybill, “Process-induced properties of fdm products,” *In Proceedings of the ICMET, International Conference on Mechanical Engineerings and Technology Congress & Exposition*, 2011.
- [50] Raise 3D, “Homepage Raise 3D,” <https://www.raise3d.com/>.
- [51] Ultimaker, “Homepage Ultimaker,” <https://ultimaker.com/>.
- [52] Makerbot Co., “Hopage Makerbot,” <https://www.makerbot.com/>.
- [53] C. Ziemian, M. Sharma, and S. Ziemian, “Anisotropic mechanical properties of ABS parts fabricated by fused deposition modelling,” *Mechanical engineering. InTech*, 2012.
- [54] M. F. Afrose, S. H. Masood, P. Iovenitti et al., “Effects of part build orientations on fatigue behaviour of FDM-processed PLA material,” *Progress in Additive Manufacturing*, vol. 1, 1-2, pp. 21–28, 2016.
- [55] R. J. Zaldivar, D. B. Witkin, T. McLouth et al., “Influence of processing and orientation print effects on the mechanical and thermal behavior of 3D-Printed ULTEM® 9085 Material,” *Additive Manufacturing*, vol. 13, pp. 71–80, 2017.

- [56] B. H. Lee, J. Abdullah, and Z. A. Khan, "Optimization of rapid prototyping parameters for production of flexible ABS object," *Journal of Materials Processing Technology*, vol. 169, no. 1, pp. 54–61, 2005.
- [57] R. Anitha, S. Arunachalam, and P. Radhakrishnan, "Critical parameters influencing the quality of prototypes in fused deposition modelling," *Journal of Materials Processing Technology*, vol. 118, 1-3, pp. 385–388, 2001.
- [58] C. T. Bellehumeur, M. K. Bisaria, and J. Vlachopoulos, "An experimental study and model assessment of polymer sintering," *Polymer Engineering & Science*, vol. 36, no. 17, pp. 2198–2207, 1996.
- [59] J. Corney, S. H. Masood, and W. Q. Song, "Thermal characteristics of a new metal/polymer material for FDM rapid prototyping process," *Assembly Automation*, vol. 25, no. 4, pp. 309–315, 2005.
- [60] J. Gonzalez-Gutierrez, S. Cano, S. Schuschnigg et al., "Additive Manufacturing of Metallic and Ceramic Components by the Material Extrusion of Highly-Filled Polymers: A Review and Future Perspectives," *Materials (Basel, Switzerland)*, vol. 11, no. 5, 2018.
- [61] R. P. Wool, B.-L. Yuan, and O. J. McGarel, "Welding of polymer interfaces," *Polymer Engineering & Science*, vol. 29, no. 19, pp. 1340–1367, 1989.
- [62] T. Ge, F. Pierce, D. Perahia et al., "Molecular dynamics simulations of polymer welding: strength from interfacial entanglements," *Physical review letters*, vol. 110, no. 9, p. 98301, 2013.
- [63] C. Bellehumeur, L. Li, Q. Sun et al., "Modeling of Bond Formation Between Polymer Filaments in the Fused Deposition Modeling Process," *Journal of Manufacturing Processes*, vol. 6, no. 2, pp. 170–178, 2004.
- [64] C. G. Schirmeister, T. Hees, E. H. Licht et al., "3D printing of high density polyethylene by fused filament fabrication," *Additive Manufacturing*, vol. 28, pp. 152–159, 2019.
- [65] M. Spoerk, F. Arbeiter, H. Cajner et al., "Parametric optimization of intra- and inter-layer strengths in parts produced by extrusion-based additive manufacturing of poly(lactic acid)," *Journal of Applied Polymer Science*, vol. 134, no. 41, p. 45401, 2017.
- [66] F. Ning, W. Cong, J. Qiu et al., "Additive manufacturing of carbon fiber reinforced thermoplastic composites using fused deposition modeling," *Composites Part B: Engineering*, vol. 80, pp. 369–378, 2015.
- [67] C. J. Yu and J. E. Sunderland, "Determination of ejection temperature and cooling time in injection molding," *Polymer Engineering & Science*, vol. 32, no. 3, pp. 191–197, 1992.
- [68] A. H. Nickel, D. M. Barnett, and F. B. Prinz, "Thermal stresses and deposition patterns in layered manufacturing," *Materials Science and Engineering: A*, vol. 317, 1-2, pp. 59–64, 2001.
- [69] C. C. Ibeh, *Thermoplastic Materials: Properties, Manufacturing Methods, and Applications*, Taylor and Francis, Hoboken, 2014.

- [70] A. V. Shenoy and D. R. Saini, *Thermoplastic melt rheology and processing*, Dekker, New York, NY, 1996.
- [71] O. Olabisi and K. P. Adewale, eds., *Handbook of thermoplastics*, CRC Press Taylor & Francis Group, Boca Raton, London, New York, 2016.
- [72] B. Wendel, D. Rietzel, F. Kühnlein et al., “Additive Processing of Polymers,” *Macromolecular Materials and Engineering*, vol. 293, no. 10, pp. 799–809, 2008.
- [73] O. S. Carneiro, A. F. Silva, and R. Gomes, “Fused deposition modeling with polypropylene,” *Materials & Design*, vol. 83, pp. 768–776, 2015.
- [74] Orbi-Tech, “Orbi-Tech PLA white 3mm filament,” <https://orbi-tech.de/shop/3D-Filamente/PLA/3-mm-PLA/PLA-Filament-3-mm-750-g-Weiss:::257.html>.
- [75] R. Singh, S. Singh, and F. Fraternali, “Development of in-house composite wire based feed stock filaments of fused deposition modelling for wear-resistant materials and structures,” *Composites Part B: Engineering*, vol. 98, pp. 244–249, 2016.
- [76] R. Singh and N. Ranjan, “Experimental investigations for preparation of biocompatible feedstock filament of fused deposition modeling (FDM) using twin screw extrusion process,” *Journal of Thermoplastic Composite Materials*, vol. 31, no. 11, pp. 1455–1469, 2018.
- [77] S.H. Masood and W.Q. Song, “Development of new metal/polymer materials for rapid tooling using Fused deposition modelling,” *Materials & Design*, vol. 25, no. 7, pp. 587–594, 2004.
- [78] C. Yang, X. Tian, D. Li et al., “Influence of thermal processing conditions in 3D printing on the crystallinity and mechanical properties of PEEK material,” *Journal of Materials Processing Technology*, vol. 248, pp. 1–7, 2017.
- [79] R. Singh and S. Singh, “Development of Nylon Based FDM Filament for Rapid Tooling Application,” *Journal of The Institution of Engineers (India): Series C*, vol. 95, no. 2, pp. 103–108, 2014.
- [80] S. Dul, L. Fambri, and A. Pegoretti, “Fused deposition modelling with ABS–graphene nanocomposites,” *Composites Part A: Applied Science and Manufacturing*, vol. 85, pp. 181–191, 2016.
- [81] O. A. Mohamed, S. H. Masood, J. L. Bhowmik et al., “Effect of Process Parameters on Dynamic Mechanical Performance of FDM PC/ABS Printed Parts Through Design of Experiment,” *Journal of Materials Engineering and Performance*, vol. 25, no. 7, pp. 2922–2935, 2016.
- [82] J. F. Rodríguez, J. P. Thomas, and J. E. Renaud, “Mechanical behavior of acrylonitrile butadiene styrene (ABS) fused deposition materials. Experimental investigation,” *Rapid Prototyping Journal*, vol. 7, no. 3, pp. 148–158, 2001.
- [83] X. Jing, H.-Y. Mi, H.-X. Huang et al., “Shape memory thermoplastic polyurethane (TPU)/poly(ϵ -caprolactone) (PCL) blends as self-knotting sutures,” *Journal of the mechanical behavior of biomedical materials*, vol. 64, pp. 94–103, 2016.

- [84] M. A. Cuiffo, J. Snyder, A. M. Elliott et al., “Impact of the Fused Deposition (FDM) Printing Process on Polylactic Acid (PLA) Chemistry and Structure,” *Applied Sciences*, vol. 7, no. 6, p. 579, 2017.
- [85] A. Rodríguez-Panes, J. Claver, and A. M. Camacho, “The Influence of Manufacturing Parameters on the Mechanical Behaviour of PLA and ABS Pieces Manufactured by FDM: A Comparative Analysis,” *Materials (Basel, Switzerland)*, vol. 11, no. 8, 2018.
- [86] J. Torres, J. Coteló, J. Karl et al., “Mechanical Property Optimization of FDM PLA in Shear with Multiple Objectives,” *JOM*, vol. 67, no. 5, pp. 1183–1193, 2015.
- [87] L. Xinhua, L. Shengpeng, L. Zhou et al., “An investigation on distortion of PLA thin-plate part in the FDM process,” *The International Journal of Advanced Manufacturing Technology*, vol. 79, 5-8, pp. 1117–1126, 2015.
- [88] Stratasys Co., “FDM Thermoplastics: Find your FDM thermoplastic”
<http://www.stratasys.com/de/materialien/fdm>.
- [89] Makerbot Co., “Makerbot Homepage,” 8/21/2018, <https://www.makerbot.com/>.
- [90] K. G. Mostafa, C. Montemagno, and A. J. Qureshi, “Strength to cost ratio analysis of FDM Nylon 12 3D Printed Parts,” *Procedia Manufacturing*, vol. 26, pp. 753–762, 2018.
- [91] S. H. Masood, K. Mau, and W. Q. Song, “Tensile Properties of Processed FDM Polycarbonate Material,” *Materials Science Forum*, 654-656, pp. 2556–2559, 2010.
- [92] J. M. Fischer, *Handbook of molded part shrinkage and warpage*, Plastics Design Library/William Andrew Pub, Norwich, NY, 2003.
- [93] P. K. Gurralla and S. P. Regalla, “Multi-objective optimisation of strength and volumetric shrinkage of FDM parts,” *Virtual and Physical Prototyping*, vol. 9, no. 2, pp. 127–138, 2014.
- [94] J. Hämäläinen, *Semi-crystalline polyolefins in fused deposition modeling: Master Thesis*, Tampere University of Technology, 2017.
- [95] V. Kishore, C. Ajinjeru, A. Nycz et al., “Infrared preheating to improve interlayer strength of big area additive manufacturing (BAAM) components,” *Additive Manufacturing*, vol. 14, pp. 7–12, 2017.
- [96] F. Knoop, and V. Schoeppner, “Mechanical and thermal properties of FDM parts manufactured with polyamide 12,” *Proceeding of SFF symposium*, pp. 935–948, 2015.
- [97] D. B. Malpass and E. I. Band, *Introduction to industrial polypropylene: Properties, catalysts, processes*, Wiley, Salem, Mass, Hoboken, N.J, 2012.
- [98] J. Karger-Kocsis (editor), *Polypropylene structure, blends and composites: Volume 3 composites*, Springer Science & Business Media, 1995.
- [99] T. Hayashi, Y. Inoue, and R. Chujo, “Ethylene-propylene copolymerization mechanism based on the sequence distributions determined by carbon-13 NMR spectra,” *Macromolecules*, vol. 21, no. 11, pp. 3139–3146, 1988.

- [100] J.-W. Housmans, M. Gahleitner, G. W.M. Peters et al., “Structure–property relations in molded, nucleated isotactic polypropylene,” *Polymer*, vol. 50, no. 10, pp. 2304–2319, 2009.
- [101] J.-Z. Liang and R.K.Y. Li, “Brittle–ductile transition in polypropylene filled with glass beads,” *Polymer*, vol. 40, no. 11, pp. 3191–3195, 1999.
- [102] C. Mathieu, A. Thierry, J. C. Wittmann et al., “Specificity and versatility of nucleating agents toward isotactic polypropylene crystal phases,” *Journal of Polymer Science Part B: Polymer Physics*, vol. 40, no. 22, pp. 2504–2515, 2002.
- [103] J. W. Teh, “Structure and properties of polyethylene–polypropylene blend,” *Journal of Applied Polymer Science*, vol. 28, no. 2, pp. 605–618, 1983.
- [104] German RepRap, “PP Polypropylen Filament”
<https://www.germanreprap.com/produkt.aspx?WPParams=50C9D4C6C5D2E6BDA5A98392A9>.
- [105] M. Jin, R. Giesa, C. Neuber et al., “Filament Materials Screening for FDM 3D Printing by Means of Injection - Molded Short Rods,” *Macromolecular Materials and Engineering*, vol. 303, no. 12, p. 1800507, 2018.
- [106] M. Spoerk, J. Sapkota, G. Weingrill et al., “Shrinkage and Warpage Optimization of Expanded-Perlite-Filled Polypropylene Composites in Extrusion-Based Additive Manufacturing,” *Macromolecular Materials and Engineering*, vol. 12, p. 1700143, 2017.
- [107] M. Spoerk, C. Holzer, and J. Gonzalez - Gutierrez, “Material extrusion - based additive manufacturing of polypropylene: A review on how to improve dimensional inaccuracy and warpage,” *Journal of Applied Polymer Science*, vol. 137, no. 12, p. 48545, 2020.
- [108] S. Hertle, M. Drexler, and D. Drummer, “Additive Manufacturing of Poly(propylene) by Means of Melt Extrusion,” *Macromolecular Materials and Engineering*, vol. 301, no. 12, pp. 1482–1493, 2016.
- [109] M. Spoerk, J. Gonzalez-Gutierrez, J. Sapkota et al., “Effect of the printing bed temperature on the adhesion of parts produced by fused filament fabrication,” *Plastics, Rubber and Composites*, vol. 47, no. 1, pp. 17–24, 2017.
- [110] M. Spoerk, J. Gonzalez-Gutierrez, C. Lichal et al., “Optimisation of the Adhesion of Polypropylene-Based Materials during Extrusion-Based Additive Manufacturing,” *Polymers*, vol. 10, no. 5, p. 490, 2018.
- [111] J. Balart, V. Fombuena, R. Balart et al., “Optimization of adhesion properties of polypropylene by surface modification using acrylic acid photografting,” *Journal of Applied Polymer Science*, vol. 15, NA-NA, 2010.
- [112] L. Wang, J. E. Sanders, D. J. Gardner et al., “Effect of fused deposition modeling process parameters on the mechanical properties of a filled polypropylene,” *Progress in Additive Manufacturing*, vol. 3, no. 4, pp. 205–214, 2018.

- [113] D. Annicchiarico and J. R. Alcock, "Review of Factors that Affect Shrinkage of Molded Part in Injection Molding," *Materials and Manufacturing Processes*, vol. 29, no. 6, pp. 662–682, 2014.
- [114] M. Jin, C. Neuber, and H.-W. Schmidt, "Tailoring polypropylene for extrusion-based additive manufacturing," *Additive Manufacturing*, vol. 33, p. 101101, 2020.
- [115] PPprint GmbH, "PPprint," <https://www.ppprint.de/>.
- [116] N. Mohan, P. Senthil, S. Vinodh et al., "A review on composite materials and process parameters optimisation for the fused deposition modelling process," *Virtual and Physical Prototyping*, vol. 12, no. 1, pp. 47–59, 2017.
- [117] P. Parandoush and D. Lin, "A review on additive manufacturing of polymer-fiber composites," *Composite Structures*, vol. 182, pp. 36–53, 2017.
- [118] L. Wang, W. Gramlich, D. Gardner et al., "Spray-Dried Cellulose Nanofibril-Reinforced Polypropylene Composites for Extrusion-Based Additive Manufacturing: Nonisothermal Crystallization Kinetics and Thermal Expansion," *Journal of Composites Science*, vol. 2, no. 1, p. 7, 2018.
- [119] M. Gahleitner, P. Jääskeläinen, E. Ratajski et al., "Propylene-ethylene random copolymers: Comonomer effects on crystallinity and application properties," *Journal of Applied Polymer Science*, vol. 95, no. 5, pp. 1073–1081, 2005.
- [120] W. Tang, J. Tang, H. Yuan et al., "Crystallization behavior and mechanical properties of polypropylene random copolymer/poly(ethylene-octene) blends," *Journal of Applied Polymer Science*, vol. 122, no. 1, pp. 461–468, 2011.
- [121] B. Kaynak, M. Spoerk, A. Shirole et al., "Polypropylene/Cellulose Composites for Material Extrusion Additive Manufacturing," *Macromolecular Materials and Engineering*, vol. 303, no. 5, p. 1800037, 2018.
- [122] M. Spoerk, F. Arbeiter, I. Raguž et al., "Polypropylene Filled With Glass Spheres in Extrusion-Based Additive Manufacturing: Effect of Filler Size and Printing Chamber Temperature," *Macromolecular Materials and Engineering*, vol. 303, no. 7, p. 1800179, 2018.
- [123] M. Spoerk, C. Savandaiah, F. Arbeiter et al., "Optimization of mechanical properties of glass-spheres-filled polypropylene composites for extrusion-based additive manufacturing," *Polymer Composites*, vol. 83, p. 768, 2017.
- [124] M. Spoerk, C. Savandaiah, F. Arbeiter et al., "Anisotropic properties of oriented short carbon fibre filled polypropylene parts fabricated by extrusion-based additive manufacturing," *Composites Part A: Applied Science and Manufacturing*, vol. 113, pp. 95–104, 2018.
- [125] R. A. Phillips, "Macromorphology of polypropylene homopolymer tacticity mixtures," *Journal of Polymer Science Part B: Polymer Physics*, vol. 38, no. 15, pp. 1947–1964, 2000.

- [126] J. Varga, "Modification change during spherulitic growth of polypropylene," *Angewandte Makromolekulare Chemie*, vol. 104, no. 1, pp. 79–87, 1982.
- [127] J. Karger-Kocsis, "Amorphous or atactic polypropylene," in *Polypropylene*, J. Karger-Kocsis, Ed., vol. 2, pp. 7–12, Springer Netherlands, Dordrecht, 1999.
- [128] J. Z. Jinneng Xie, *Polypropylene for 3D printing, polyethylene composite consumable and preparation method thereof*, 2014.
- [129] B. Fillon, A. Thierry, J. C. Wittmann et al., "Self-nucleation and recrystallization of polymers. Isotactic polypropylene, β phase: B- α conversion and β - α growth transitions," *Journal of Polymer Science Part B: Polymer Physics*, vol. 31, no. 10, pp. 1407–1424, 1993.
- [130] J. Karger-Kocsis and J. Varga, "Effects of β - α transformation on the static and dynamic tensile behavior of isotactic polypropylene," *Journal of Applied Polymer Science*, vol. 62, no. 2, pp. 291–300, 1996.
- [131] J. Karger-Kocsis, ed., *Polypropylene*, Springer Netherlands, Dordrecht, 1999.
- [132] D. Libster, A. Aserin, and N. Garti, "Advanced nucleating agents for polypropylene," *Polymers for Advanced Technologies*, vol. 18, no. 9, pp. 685–695, 2007.
- [133] A. T. Jones, J. M. Aizlewood, and D. R. Beckett, "Crystalline forms of isotactic polypropylene," *Die Makromolekulare Chemie*, vol. 75, no. 1, pp. 134–158, 1964.
- [134] B. Lotz, " α and β phases of isotactic polypropylene: a case of growth kinetics 'phase reentrancy' in polymer crystallization," *Polymer*, vol. 39, no. 19, pp. 4561–4567, 1998.
- [135] József Varga, " β -MODIFICATION OF ISOTACTIC POLYPROPYLENE: PREPARATION, STRUCTURE, PROCESSING, PROPERTIES, AND APPLICATION," *Journal of Macromolecular Science, Part B*, vol. 2002, Volume 41 2002 - Issue 4-6.
- [136] C. Grein, C.J.G. Plummer, H.-H. Kausch et al., "Influence of β nucleation on the mechanical properties of isotactic polypropylene and rubber modified isotactic polypropylene," *Polymer*, vol. 43, no. 11, pp. 3279–3293, 2002.
- [137] J. Kotek, M. Raab, J. Baldrian et al., "The effect of specific: beta-nucleation on morphology and mechanical behavior of isotactic polypropylene," *Journal of Applied Polymer Science*, vol. 85, no. 6, pp. 1174–1184, 2002.
- [138] G.-y. Shi, B. Huang, and J.-y. Zhang, "Enthalpy of fusion and equilibrium melting point of the beta-form of polypropylene," *Die Makromolekulare Chemie, Rapid Communications*, vol. 5, no. 9, pp. 573–578, 1984.
- [139] J. Výchoňová, V. Habrová, M. Obadal et al., "Crystallization of polypropylene with a minute amount of β -nucleator," *Journal of Thermal Analysis and Calorimetry*, vol. 86, no. 3, pp. 687–691, 2006.

- [140] H.B. Chen, J. Karger-Kocsis, J.S. Wu et al., “Fracture toughness of α - and β -phase polypropylene homopolymers and random- and block-copolymers,” *Polymer*, vol. 43, no. 24, pp. 6505–6514, 2002.
- [141] L. Wang and D. J. Gardner, “Effect of fused layer modeling (FLM) processing parameters on impact strength of cellular polypropylene,” *Polymer*, vol. 113, pp. 74–80, 2017.
- [142] C. M. González-Henríquez, M. A. Sarabia-Vallejos, and J. Rodríguez-Hernandez, “Polymers for additive manufacturing and 4D-printing: Materials, methodologies, and biomedical applications,” *Progress in Polymer Science*, vol. 94, pp. 57–116, 2019.
- [143] J. Carrell, G. Gruss, and E. Gomez, “Four-dimensional printing using fused-deposition modeling: a review,” *Rapid Prototyping Journal*, ahead-of-print, ahead-of-print, 2020.
- [144] J. Leng, X. Lan, Y. Liu et al., “Shape-memory polymers and their composites: Stimulus methods and applications,” *Progress in Materials Science*, vol. 56, no. 7, pp. 1077–1135, 2011.
- [145] C. Liu, H. Qin, and P. T. Mather, “Review of progress in shape-memory polymers,” *Journal of Materials Chemistry*, vol. 17, no. 16, p. 1543, 2007.
- [146] M. D. Hager, S. Bode, C. Weber et al., “Shape memory polymers: Past, present and future developments,” *Progress in Polymer Science*, 49-50, pp. 3–33, 2015.
- [147] H. TOBUSHI, S. HAYASHI, and S. KOJIMA, “Mechanical Properties of Shape Memory Polymer of Polyurethane Series : Basic Characteristics of Stress-Strain-Temperature Relationship,” *JSME international journal. Ser. 1, Solid mechanics, strength of materials*, vol. 35, no. 3, pp. 296–302, 1992.
- [148] D. Ratna and J. Karger-Kocsis, “Recent advances in shape memory polymers and composites: a review,” *Journal of Materials Science*, vol. 43, no. 1, pp. 254–269, 2008.
- [149] Y. Mosleh, N. G. Ebrahimi, A. Mahdavian et al., “TPU/PCL/nanomagnetite ternary shape memory composites: studies on their thermal, dynamic-mechanical, rheological and electrical properties,” *Iranian Polymer Journal*, vol. 23, no. 2, pp. 137–145, 2014.
- [150] Q. Zhao, H. J. Qi, and T. Xie, “Recent progress in shape memory polymer: New behavior, enabling materials, and mechanistic understanding,” *Progress in Polymer Science*, 49-50, pp. 79–120, 2015.
- [151] Elkins, Kurt, et al, ed., *Soft Elastomers for Fused Deposition Modeling*, 1997.
- [152] J. M. Nasereddin, N. Wellner, M. Alhijaj et al., “Development of a Simple Mechanical Screening Method for Predicting the Feedability of a Pharmaceutical FDM 3D Printing Filament,” *Pharmaceutical research*, vol. 35, no. 8, p. 151, 2018.
- [153] A. C. de Visser, D. E. Gregonis, and A. A. Driessen, “Segmented copolyether-imides,” *Die Makromolekulare Chemie*, vol. 179, no. 7, pp. 1855–1859, 1978.
- [154] A. Ghosh, S. K. Sen, S. Banerjee et al., “Solubility improvements in aromatic polyimides by macromolecular engineering,” *RSC Advances*, vol. 2, no. 14, p. 5900, 2012.

- [155] Y. Hou, G. Chen, X. Pei et al., “Synthesis and characterization of novel optically transparent and organosoluble polyimides based on diamines containing cyclohexane moiety,” *Journal of Polymer Research*, vol. 19, no. 9, p. 1275, 2012.
- [156] S. Luo, K. A. Stevens, J. S. Park et al., “Highly CO₂-Selective Gas Separation Membranes Based on Segmented Copolymers of Poly(Ethylene oxide) Reinforced with Pentiptycene-Containing Polyimide Hard Segments,” *ACS applied materials & interfaces*, vol. 8, no. 3, pp. 2306–2317, 2016.
- [157] A. S. Mathews, I. Kim, and C.-S. Ha, “Synthesis, characterization, and properties of fully aliphatic polyimides and their derivatives for microelectronics and optoelectronics applications,” *Macromolecular Research*, vol. 15, no. 2, pp. 114–128, 2007.
- [158] Z. Liang, R. A. Cormier, A. M. Nardes et al., “Developing perylene diimide based acceptor polymers for organic photovoltaics,” *Synthetic Metals*, vol. 161, 11-12, pp. 1014–1021, 2011.
- [159] Z. Liang, R. A. Cormier, A. M. Nardes et al., “Solution Processable n-Type Perylene Diimide Copolymers for Organic Photovoltaics,” *MRS Proceedings*, vol. 1286, 2011.
- [160] E. Rostami-Tapeh-Esmail, M. Golshan, M. Salami-Kalajahi et al., “Perylene-3,4,9,10-tetracarboxylic diimide and its derivatives: Synthesis, properties and bioapplications,” *Dyes and Pigments*, p. 108488, 2020.
- [161] T. Sakurai, N. Orito, S. Nagano et al., “Electron-transporting foldable alternating copolymers of perylenediimide and flexible macromolecular chains,” *Materials Chemistry Frontiers*, vol. 2, no. 4, pp. 718–729, 2018.
- [162] G. Hernández, N. Casado, A. M. Zamarayeva et al., “Perylene Polyimide-Polyether Anodes for Aqueous All-Organic Polymer Batteries,” *ACS Applied Energy Materials*, vol. 1, no. 12, pp. 7199–7205, 2018.
- [163] J. Z. Jinneng Xie, *Polypropylene for 3D printing, polyethylene composite consumable and preparation method thereof*, 2014.
- [164] C. Liu, J. Yuan, X. Luo et al., “Folate-decorated and reduction-sensitive micelles assembled from amphiphilic polymer-camptothecin conjugates for intracellular drug delivery,” *Molecular pharmaceuticals*, vol. 11, no. 11, pp. 4258–4269, 2014.
- [165] M. Iijima, D. Ulkoski, S. Sakuma et al., “Synthesis of PEGylated poly(amino acid) pentablock copolymers and their self-assembly,” *Polymer International*, vol. 65, no. 10, pp. 1132–1141, 2016.
- [166] Sigma Aldrich, “Jeffamine® ED-900”
<https://www.sigmaaldrich.com/catalog/product/aldrich/14527?lang=de®ion=DE>.

2. The objective of this thesis

The main objective of this thesis is to establish an efficient small-scale feedstock material development method for extrusion-based 3D printing. Usually, the feedstock material is a continuous filament, and quantities of several kilograms are required for filament production. In the development stage, the number of polymers and additives available for scientific studies is usually limited. Thus, there is a demand for small-scale targeted material development for extrusion-based 3D printing. Here, the objectives and motivations are summarized into the following three topics: (i) *effective material screening method*, (ii) *tailoring polypropylene for extrusion-based 3D printing*, and development of (iii) *(AB)_n segmented copolyetherimides for 3D and 4D printing*.

Effective material screening method for extrusion-based 3D printing

Continuous filament extrusion is the conventional feedstock material processing method for extrusion-based 3D printing, where the amount of required raw material is around 1-5 kg. Thus, time and material consumption are high for the development of new materials or formulations.

Therefore, the first topic of this thesis is to present *an effective material screening method for extrusion-based 3D printing* to evaluate the printing performances of polymer materials. For that, by using a mini compounder and a mini injection molding machine, an alternative feedstock filament short rods fabrication method with less material input (from 10-50 g) has to be developed, which can joint together and to be fed in the same way as continuous feedstock filament. At the same time, a particular miniature printing specimen has to be designed for the evaluation of printing performances in particular material-shrinkage-induced warp deformation and interlayer bonding quality. Also, a systematic evaluating method should be established for revealing the printing performances from printed specimens. At last, different polypropylene raw materials should be processed into filament rods and compared to two commercially available filaments and a commercial ABS filament for validating this method

Tailoring polypropylene for extrusion-based 3D printing

Polypropylene is the most common applied semi-crystalline thermoplastic in consumer and technical products with exceptional mechanical properties, processing and modification ability, and low cost. Semi-crystalline materials could gain reinforcement by crystals at layer interfaces and thus are fascinating materials for extrusion-based 3D printing. However, limited commercial PP filaments were available at the beginning of this thesis due to its volume shrinkage and part warpage.

The second topic is about *polypropylene tailoring for extrusion-based 3D printing* with optimized formulations and printing performances combined with the developed small-scale feedstock material development method. Based on the first topic, two candidates of commercially available grades of polypropylene/ethylene random copolymers (raco PP) should be modified. The modifications aimed to reduce warp deformation caused by shrinkage and, at the same time, reduce the anisotropic property by improving the interlayer bonding quality. Here it is planned to use nucleating agents as additives and amorphous polypropylenes (aPP) and polyethylene (PE) as blend components and to investigate their influence concerning warpage and mechanical properties of the printed parts. The performance should be compared with commercially available PLA and ABS filaments.

(AB)_n segmented copolyetherimides for 3D and 4D printing

(AB)_n segmented copolyetherimides consisting of perylene and poly(ethylene glycol) are applied in fields of all-organic polymer batteries and organic photovoltaics. With crystallized PEG segments, such (AB)_n segmented copolyetherimides are promising candidates for 4D printing by utilizing 3D printing in combination with a shape memory property.

The third topic deals with the development of *(AB)_n segmented copolyetherimides for 3D and 4D printing*. For this, the flexible PEG segments should be able to crystallize above room temperature, and the perylene bisimides segments should be able to form physical crosslinks via π - π interactions at higher temperatures. The synthesized (AB)_n segmented copolyetherimides are expecting to have two transitions to enable a shape memory effect for 4D printing. Besides, the crystallized PEG segments should improve the filament stiffness to overcome the feeding issue in an extrusion-based 3D printer. Therefore, characterizations regarding their thermal, rheological, and mechanical properties in view of 3D printing have to be investigated. At last, the shape memory effect should be investigated, and a successful 4D printing should be demonstrated.

3. Synopsis

3.1 Overview of the Thesis

The objective of this thesis is to establish a fast and efficient small-scale material development method for extrusion-based 3D and 4D printing. The objective covers three main topics (i) *an efficient material screening method for extrusion-based 3D printing*, (ii) *tailoring polypropylene for extrusion-based 3D printing*, and development of a new class of (iii) *(AB)_n segmented copolyetherimides for 3D and 4D printing*.

The three topics were addressed stepwise and resulted in two publications and one submitted manuscript. *Figure 14* illustrates schematically how the three topics are connected, and therefore they are structured in a pyramid-like schema.

The fundamental approach: the miniature feedstock short filament rods fabrication by using a mini compounder and a mini injection molding machine from a limited polymer amount (10-50g). The special printing specimen (square tube) was designed for identifying and testing the 3D printed part performances. *Small-scale processing and testing* methods were developed.

Topic 1: Based on the miniature material processing and well-established testing approach, an effective material screening method to evaluate printing performances of thermoplastic polymers for extrusion-based additive manufacturing was developed (*Figure 14, I*). The findings of this topic are published as a full paper article.

Topic 2: Furthermore, the expertise was extended to tailor the promising semi-crystalline material polypropylene for obtaining optimized formulations and printing performances (*Figure 14, II*). The findings of this topic are published as a full paper article.

Topic 3: Last, the acquired know-how was transferred to develop a new class of (AB)_n segmented copolyetherimides consisting of perylene bisimide and poly(ethylene-glycol) segments which provide a shape memory effect used for 4D printing (*Figure 14, III*). The results of this topic are presented in a manuscript that will be submitted shortly.

The following chapters of the synopsis will give an overview of the major findings and results of each topic, all literature references can be found in the attached publications and manuscript.

Material development for extrusion-based 3D printing

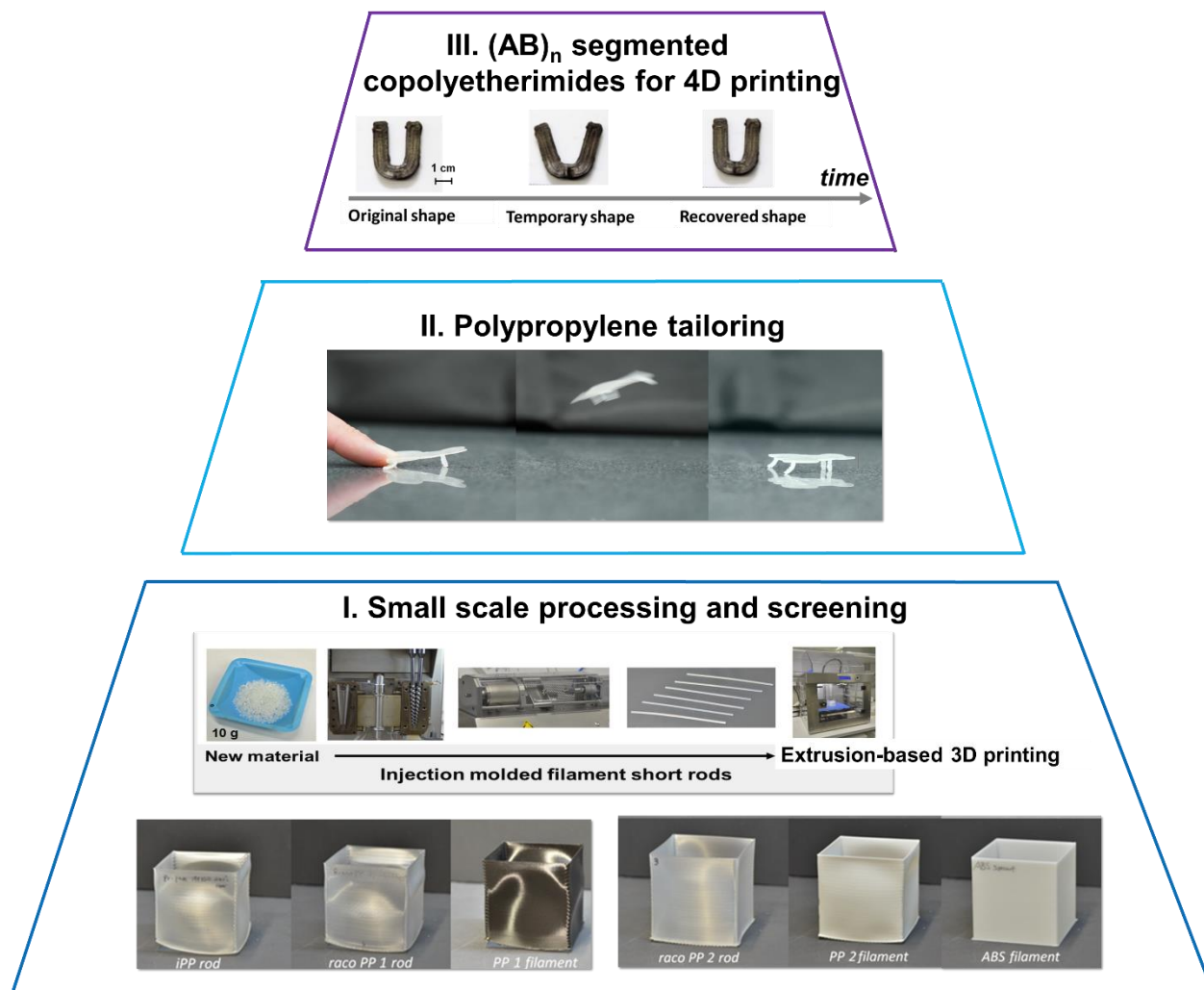


Figure 14: Overview of the thesis: I). Effective material screening method to evaluate 3D printed part performances of thermoplastic polymers for extrusion-based additive manufacturing. The mini compounder and mini injection molding machine allow the fabrication of feedstock short filament rods from limited material amount. The printed square tube allows the identification of 3D printed part performances. The combination of small-scale processing and testing methods is the fundamental approach for all three topics. II). The promising semi-crystalline material polypropylene was tailored for with respect to optimized formulations and printed part performances. III). A new class of $(AB)_n$ segmented copolyetherimides consisting of perylene bisimides and poly(ethylene-glycol) segments was developed for 3D and 4D printing.

3.2 Filament materials screening for FDM by means of injection molded short rods¹

In this paper, efficient small-scale screening and testing method, which requires only 10 to 50 g is developed to enhance materials for the extrusion-based 3D printing. This was achieved in this paper by using a mini compounder and a mini injection molding machine to produce short filament rods which were joint together and used as feedstock material in the 3D printer. Also, a particular test specimen, in the form of a printed freestanding square tube consisting of only a single-material-line stack, was used for the evaluation of critical performance parameters of printed parts, in particular warp deformation and interlayer bonding quality.

Filament short rod processing

Figure 15 shows the entire processing sequence from raw material to feedstock filament short rods and their use as extrusion-based 3D printing material. The main advantage of the presented method is shown in the fabrication of rods with a well-defined and reproducible geometry, requiring only a small amount of raw material useable for the extrusion-based 3D printing process. Three different PP grades were processed into rods (*iPP rod*, *raco PP1 rod*, and *raco PP2 rod*) and 3D printed.

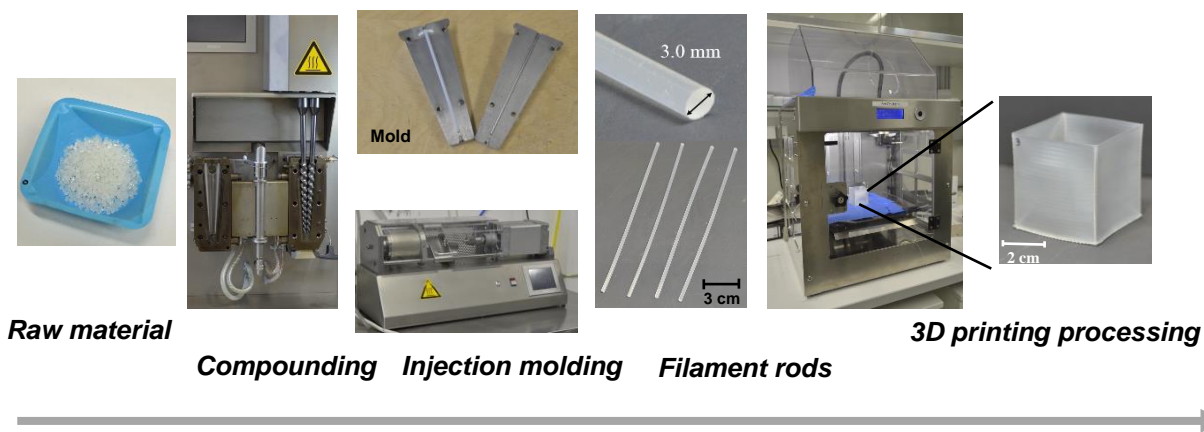


Figure 15: Sequence of the fabrication of rods for extrusion-based 3D printing material screening. The raw material is first compounded in a mini mixer and then injection-molded into Teflon[®] tubing, fabricating individual filament rods. These are then fed into an FDM 3D printer and printed into square tubes. (© 2018 Authors)

¹This part of the thesis was published as a full paper article in the journal *Macromolecular Materials and Engineering* **2018** 303(12), 1800507, see also **Chapter 4.3**, reprint and reuse of full paper with permission from *John Wiley and Sons*.

Printed square tube for printing performances evaluation

For comparison, commercial continuous filaments (*ABS filament*, *PP1 filament* and *PP2 filament*) were also printed into square tubes via extrusion-based 3D printing. The geometry of the square tube was selected due to its simplicity and a small amount of material consumption. With this thin-wall, single-layer geometry, the side-wall warp deformation is greatly pronounced and allows the visualization and quantitative evaluation using simple geometric measurements. Additionally, tensile tests of specimens along and perpendicular to the printing direction will provide direct information about the layer bonding strength. In *Figure 16*, images of extrusion-based 3D printed square tubes are depicted. Here, the extent of warp deformation is clearly visible, with PP exhibiting pronounced warp deformation and ABS, a common reference filament material for extrusion-based 3D printing, being almost warp-free.

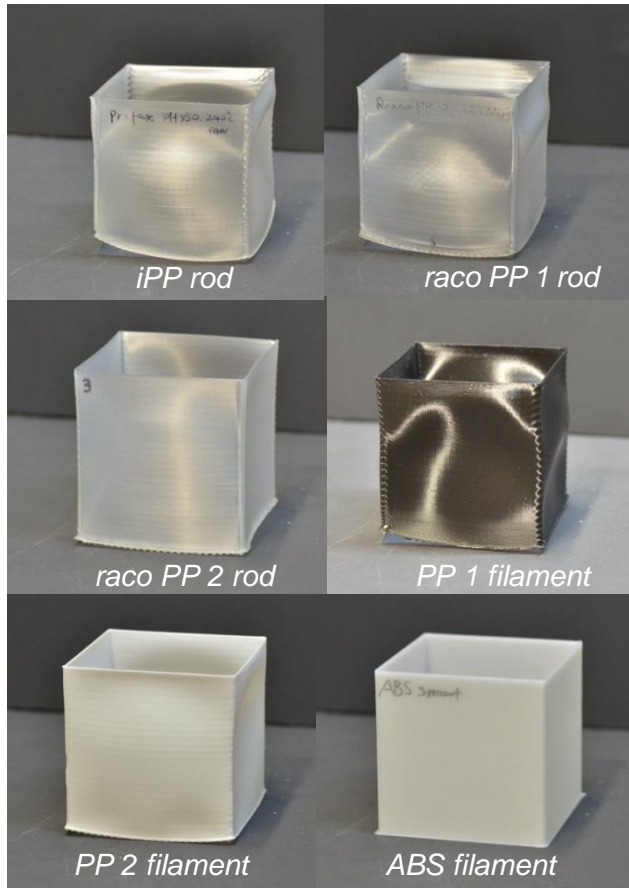


Figure 16: Extrusion-based 3D printed square tube geometries of different polypropylene grades compared with amorphous ABS. PP exhibits significant warp deformation whereas ABS can be printed without visible warp deformation. (© 2018 Authors)

Geometric deformation

Figure 17 (left) depicts the sidewall warp deformation from a top view (*raco PP 2 rod*). The distance between the maximum deformation point (white dashed line) and the ideal non-deformation contour (black line) corresponds to the warp deformation value, noted as d_{warp} . Figure 17 (right) summarizes the measured averaged values of warp deformation (d_{warp}) for all sidewalls. The data demonstrate that d_{warp} correlates with the degree of crystallization. In summary, small lab-scale filament short rod manufacturing in combination with FDM printing into a single layer square tube geometry, offers a fast and efficient evaluation of geometric warp deformation of new feedstock materials.

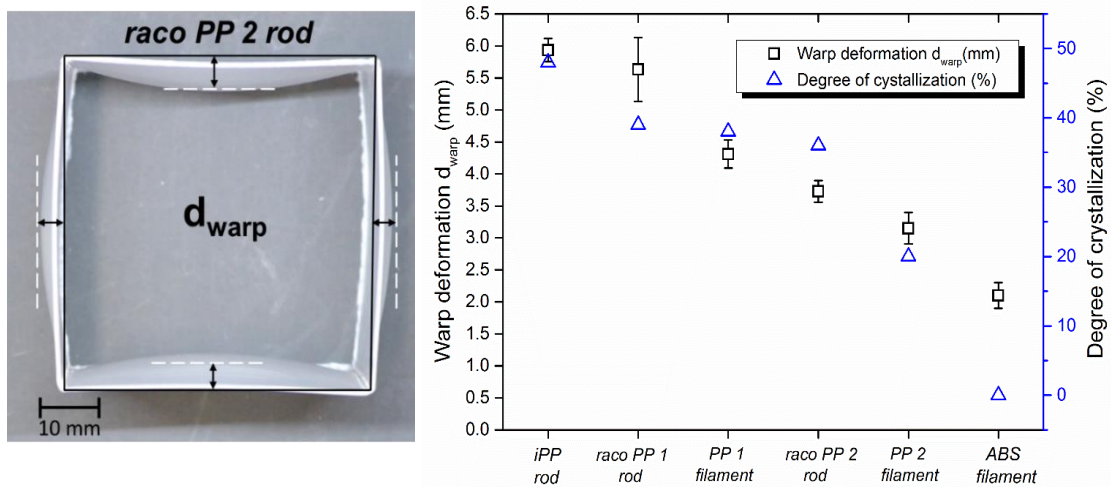


Figure 17: (left) Definition of warp deformation as observed from the top view of a printed square tube of *raco PP 2 rod*. The distance between the ideal non-deformation square contour (black line) and the maximum deformation position of each sidewall (white dashed line) was measured and averaged for the reported geometric deformations, noted as d_{warp} . (right): Warp deformation (d_{warp}) and degree of crystallization (measured by DSC) of different grades of PPs, raco PPs, and reference filament ABS. (© 2018 Authors)

Mechanical properties

From each sidewall of the 3D printed square tube a maximum of five dog bones as test specimens (*Figure 18*) were punched out with angles of 90° and 0° to the layer deposition direction (X- and Y-axis). Due to this dog-bone punching, the complexity of contour and infill deposition techniques for producing discrete test specimens is avoided and thus allows the reliable measurement of mechanical properties. For 90° specimens, the tensile loading direction is perpendicular to the layer deposition direction, and the load is applied to the interlayer bonding area. For the 0° specimen, the load is longitudinal to the deposited layer

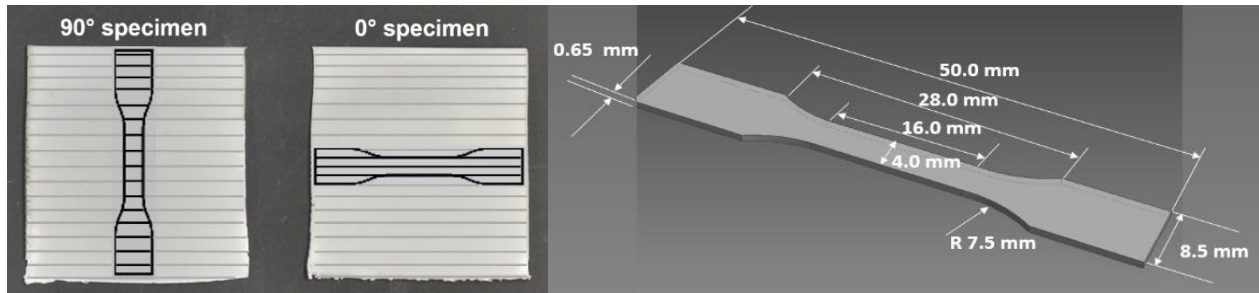


Figure 18: Specimens (nominal tensile specimen dimensions according to DIN 53504-S3a standard) were punched out of 3D printed square tube sidewalls, resulting in two different tensile specimens for evaluating the interlayer bonding quality. (© 2018 Authors)

Mechanical characterization was conducted using three selected square tubes printed from *PP 1 filament*, *PP 2 filament*, and *raco PP 2 rod* showing the lowest geometric deformations. *Figure 19* depicts representative strength-strain curves of different PPs.

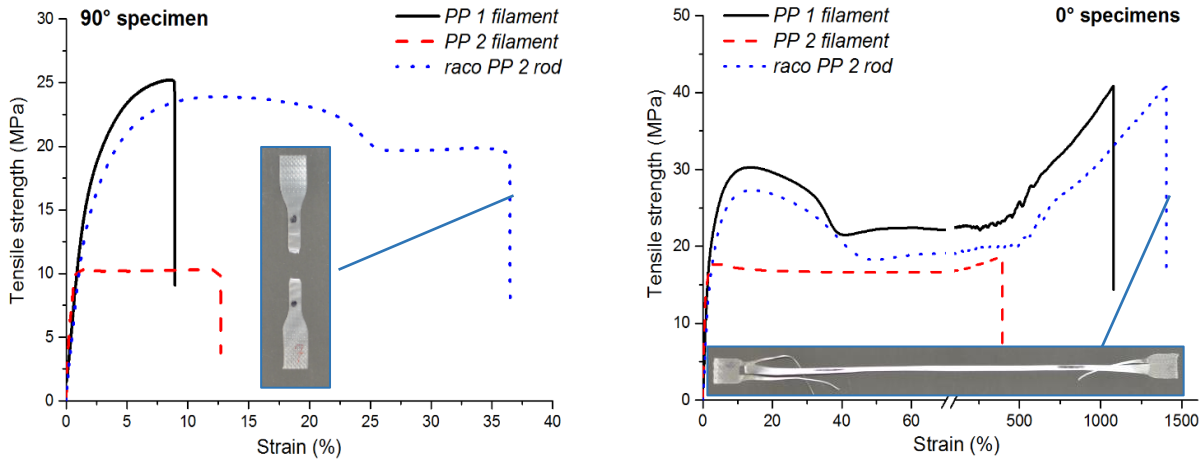


Figure 19: (a) Tensile curves of 90° specimens and (b) 0° specimens of three different PP grades (PP 1 filament: solid line, PP 2 filament: dashed line, raco PP 2 rod: dotted line) and images of failed dog bones (from raco PP 2 rod). (© 2018 Authors)

3.3 Tailoring polypropylene for extrusion-based additive manufacturing²

The second paper reports on the tailoring of polypropylene (PP) feedstock material towards extrusion-based 3D printing. To achieve this, two commercially available grades of polypropylene/ethylene random copolymers (raco PP) were modified (see *Table 1*), aiming to reduce warp deformation caused by shrinkage and at the same time to reduce the anisotropic property by improving the interlayer bonding quality of 3D printed parts processed by extrusion-based 3D printing. A β -nucleating agent, several amorphous polypropylenes (aPP) and one linear low-density polyethylene (LLDPE) were selected as additive or blending component to reduce shrinkage. The polypropylene feedstock material optimization was conducted by a combination of a lab-scale filament rod processing method and utilizing printed square tubes to optimize 3D printing performance. Investigated materials (see *Table 1*) were compounded and injection-moulded into filament rods instead of using conventional continuous feedstock filaments.

Table 1: Composition of polymer blends comprising a β -nucleating agent, amorphous PP or LLDPE.

PP	Additive/aPPs	Concentration
<i>raco PP 1</i>	β -nucleating agent	100, 500, 1000 ppm
<i>raco PP 1</i>	<i>aPP 1</i>	1.0, 5.0, 10.0 wt%
<i>raco PP 2</i>	<i>aPP 1</i>	10.0, 15.0, 20.0 wt%
<i>raco PP 2</i>	<i>aPP 2-6</i>	10.0 wt%
<i>raco PP 2</i>	LLDPE	10.0 wt%

β -nucleating agent and LLDPE as blend component

The achieved results demonstrate that the crystallization behavior and E-modulus of polypropylene play significant roles for warp deformation in extrusion-based 3D printed parts. The β -nucleating agent alters the crystallization behavior towards an increased β -crystal content, even a slightly negative influence on the warp deformation was observed. The investigated polymer blend of raco PP and LLDPE shows no significant contribution to reduce the warpage and also impairs also the interlayer bonding strength.

Amorphous PP as blend component

The most promising results were achieved by blending raco PP with selected amorphous PPs. With two aPP grades, warp deformation could be drastically reduced. In addition, the interlayer bonding quality is remarkably enhanced in these blends in spite of slight decreases in stiffness and strength. In conclusion, the

²This part of the thesis was published as a full paper article in the journal *Additive Manufacturing* **2020** 33, 101101, see also **Chapter 4.4**, reprint and reuse of full paper with permission from *Elsevier*.

optimized raco PP/aPP blend feedstock material features less warp deformation, high stiffness and, most importantly, outstanding interlayer bonding strength. To compare the performance of 3D printed parts of the investigated two raco PP grades and their optimized blends with aPPs, we selected neat *raco PP 1* and *2*, the blends of *raco PP 1* and 10 wt% of *aPP 1*, and *raco PP 2* and 10 wt% of *aPP 2*. For reference purposes, we selected four commercially available PP filaments denoted as *PP 1-4*.

Results of PP filament optimization

From *Figure 20* (left), the measured geometric deformation demonstrates that the values could be clearly reduced by blending the investigated raco PP grades with 10 wt% of an aPP (visualized by arrows in *Figure 20*), and optimized values are at a very similar level to those of the commercially available filaments *PP 2* and *3*.

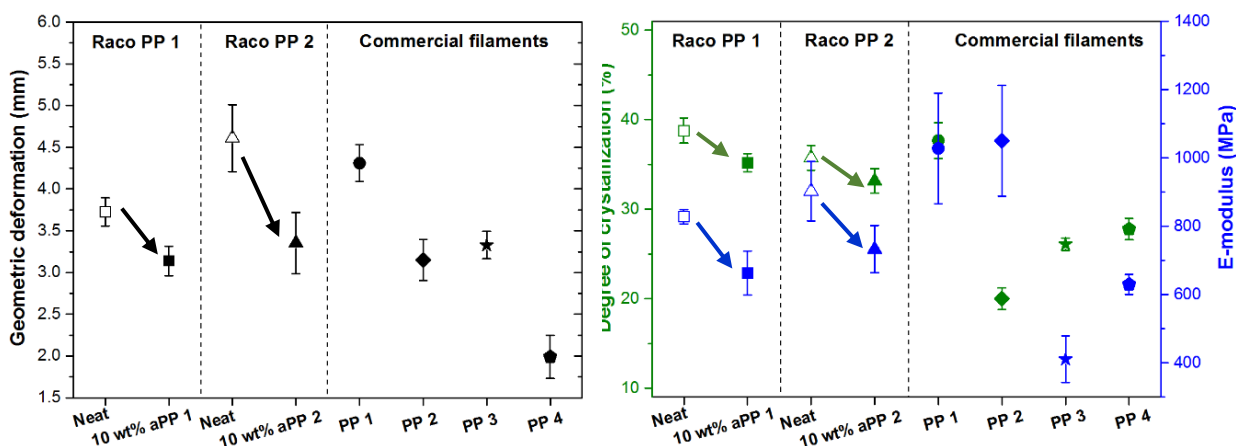


Figure 20: (left) Geometric deformation and (right) degree of crystallization and E-moduli (90° orientation) of printed square tube specimens of raco PP 1 and 2, the blends of raco PP 1 and 10 wt% of aPP 1, raco PP 2 and 10 wt% of aPP 2, and selected commercial PP filaments (hollow cube: raco PP 1, solid cube: raco PP 1 with 10 wt% aPP 1, hollow triangle: raco PP 2, solid triangle: raco PP 2 with 10 wt% aPP 2, filled circle: commercial PP 1, filled diamond: commercial PP 2, filled star: commercial PP 3, filled pentagon: commercial PP 4, arrows: tendency from neat raco PP to modified raco PP by blending with 10 wt% of aPP 1 or aPP 2). (© 2020 Authors)

While the commercial *PP 1* shows higher geometric deformation, the commercial *PP 4* demonstrates the best value for this property among all investigated PP specimens. From *Figure 20* (right), the degree of crystallization is slightly higher for blending *raco PP 1* with *aPP 1* compared with *raco PP 2* blended with *aPP 2*, while the E-modulus decrease trend is reversed. The E-moduli of modified PPs are around 700 MPa, which is similar to that of the commercial *PP 4*. The commercial *PP 1* has the highest E-modulus and degree of crystallization, which lead to the highest geometric deformation value. The commercial *PP 2* and *PP 4* show very interesting properties. *PP 2* shows the lowest degree of crystallization but a significantly higher E-modulus, resulting in a relatively low geometric deformation value, which indicates that the influence of

the degree of crystallization is very important concerning part geometric deformation. In comparison, *PP 4* offers a higher degree of crystallization and lower E-modulus and features the lowest geometric deformation. In conclusion, these observations confirm that the combination of degree of crystallization and stiffness causes the final geometric deformation of 3D printed parts. *Figure 21* demonstrates the mechanical properties of neat raco PP grades and optimized raco PP blends compared with the commercial PP filaments.

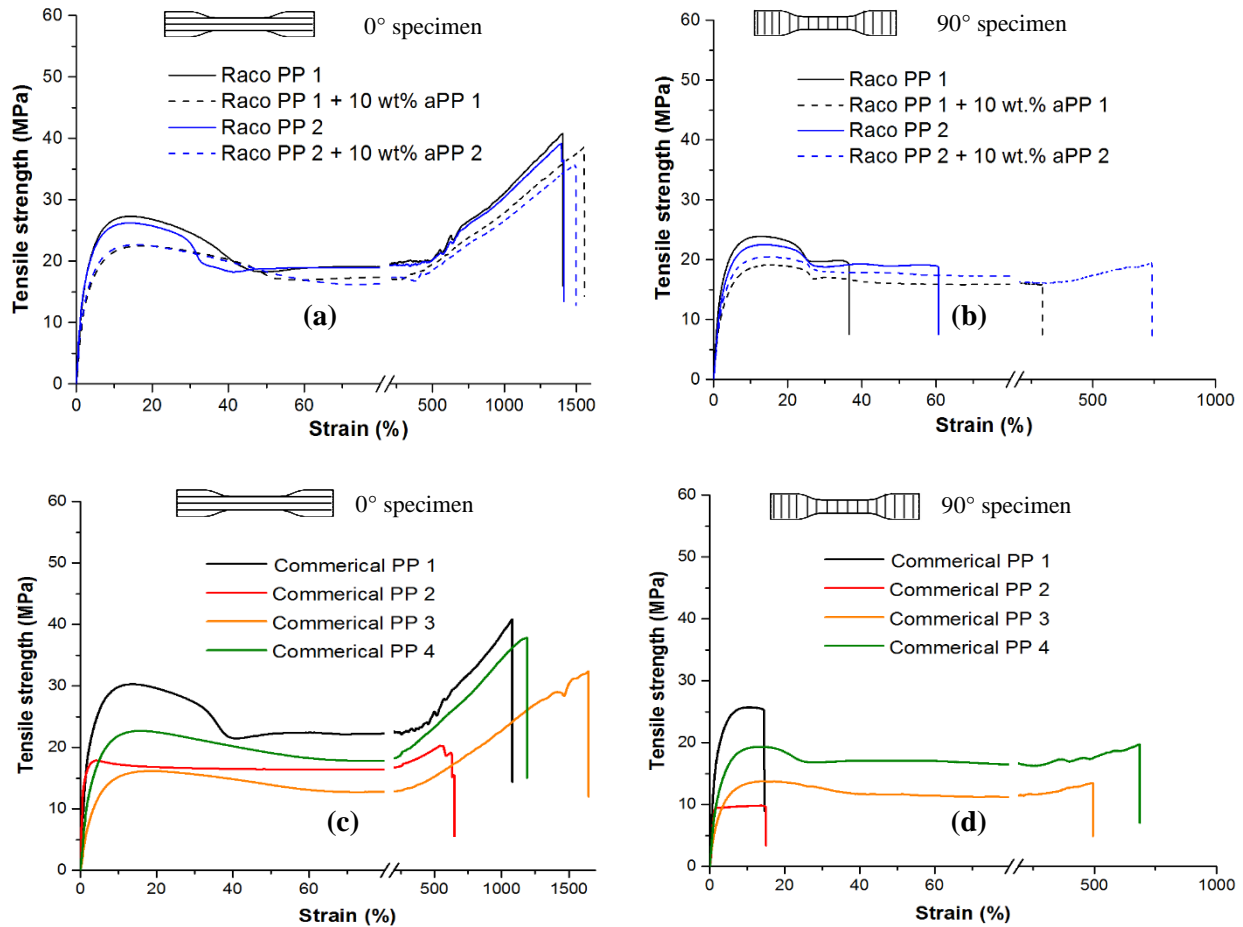


Figure 21: Stress-strain curves of **a)** 0° specimens and **b)** 90° specimens of raco PP 1, raco PP 1 with 10 wt% aPP 1, raco PP 2, and raco PP 2 with 10 wt% aPP 2 (raco PP 1: solid black line, raco PP 1 with 10 wt% aPP 1: black dashed line, raco PP 2: solid blue line, raco PP 2 with 10 wt% aPP 2: blue dashed line). Stress-strain curves of **c)** 0° specimens and **d)** 90° specimens of commercial PP filaments (commercial PP 1 to 4: black, red, orange, and solid green lines). All shown stress-strain curves are a representative example of an actual measurement out of at least 10 specimens. (© 2020 Authors)

From *Figure 21(a)*, for 0° specimens, the tensile curves for neat raco PPs are very similar, and the curves of the blended raco PPs show a similar progression, too. The general trend is that E-moduli and strengths decline from neat to blended raco PPs, while high strains of above 1400 % are obtained for all specimens.

In contrast, the strains of 90° specimens show clear differences and are dramatically improved for the blended *raco* PPs compared with the neat specimens, which means the interlayer strain bonding quality is significantly enhanced by adding 10 wt% *aPP*. This trend is especially observed when blending *raco PP 2* with *aPP 2*, as here the 90° specimen's measured tensile strain is approximately 50 % of that of the corresponding 0° specimen. For neat *raco PP 2*, this anisotropic behavior only allows a value of less than 5 %. As expected, a drop of tensile strength and E-modulus is observed for blended *raco* PPs due to the smoothness of amorphous polyolefin chains, which could act as a plasticizer. In *Figure 21* (c) and (d), the mechanical properties of all commercial PP filaments are compiled. The commercial *PP 1* demonstrates the highest tensile modulus and strength for the 0° specimen, but also the lowest strain interlayer bonding for the 90° specimen. Commercial *PP 2* and *3* show similar tensile strengths, but commercial *PP 2* exhibits significantly lower tensile strain. The commercial *PP 4* offers the strongest interlayer bonding among all commercial PPs and excellent mechanical properties as well. The observed differences in mechanical properties may be explained by the different chemical nature of the investigated PP grades, as there is a huge discrepancy between commercially available PP filaments. In conclusion, the key criteria for optimizing a PP filament for extrusion-based 3D printing are the degree of crystallization, high mechanical properties, excellent interlayer bonding, as well as identifying the optimal balance of these three.

3.4 (AB)_n segmented copolyetherimides for 4D printing³

In the third topic, a new class of (AB)_n segmented copolyetherimides for 3D and 4D printing was developed. The polymer requires two separate transitions at different temperatures, $T_{\text{trans.}(low)}$ and $T_{\text{trans.}(high)}$, in order to provide processability for extrusion-based 3D printing with the additional shape memory effect. In this respect, the (AB)_n segmented copolyetherimides **1a** and **1b** consist of polyethylene glycol segments that crystallize above room temperature and of perylene bisimides segments, which are responsible for forming physical crosslinks via π - π interactions at higher temperatures.

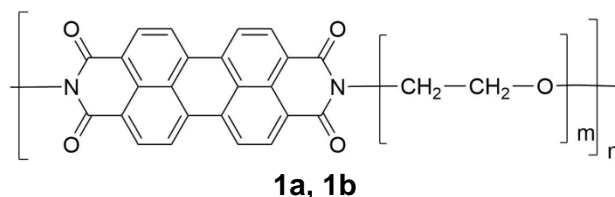


Figure 22: Chemical structure of synthesized (AB)_n segmented polymers **1a** and **1b** with rigid perylene bisimide segments and flexible polyethylene glycol (PEG) segments (**1a**: $m = 45$, **1b**: $m = 182$).

Thermal and rheological characterization

The thermal and rheological properties of synthesized (AB)_n segmented copolyetherimides were investigated to determine their transition temperatures.

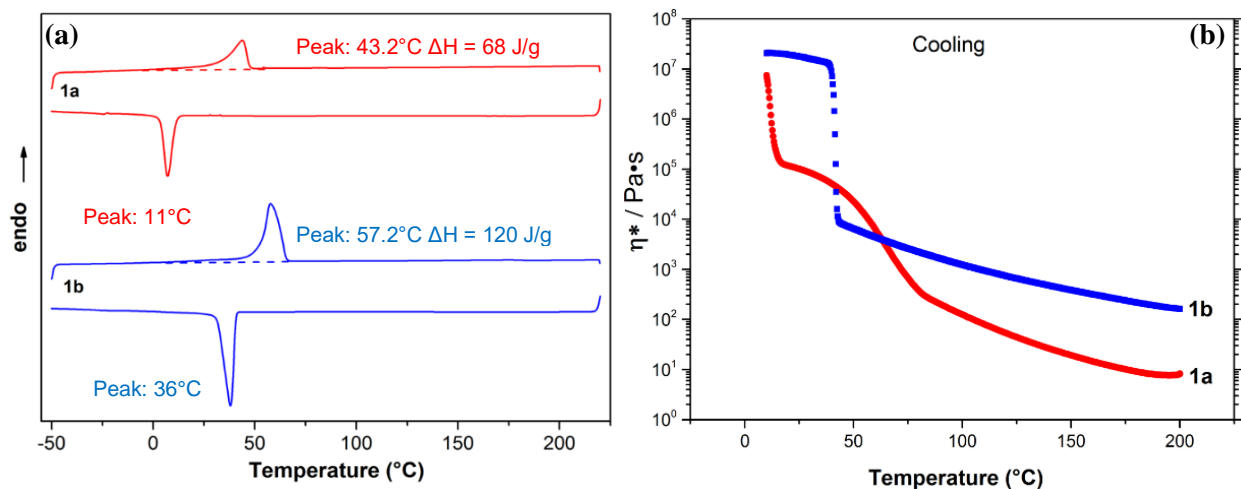


Figure 23: (a) DSC second heating and cooling curves (rate 10 K/min) with corresponding melting temperatures and enthalpies and recrystallization temperatures of polyethylene glycol segments (b) oscillatory shear rheology measurements upon cooling of the (AB)_n segmented copolyetherimides **1a** and **1b**.

³This part of the thesis was submitted to the journal *Macromolecular Materials and Engineering*, see manuscript **Chapter 4.5**.

In *Figure 23* (a), DSC 2nd heating and cooling curves of **1a** and **1b** are shown. Both curves show one endothermic transition between 40 °C and 60 °C representing the melting of the crystallized PEG segments. In rheology measurements upon cooling (*Figure 23* (b)). Here both copolyetherimides **1a** and **1b** show a low melt viscosity at above 200 °C, which should allow easy extrusion-based 3D printing. A clear increase in viscosity is observed at about 40 °C, and 10 °C, respectively, and they fit well to corresponding recrystallization temperatures of PEG segments as measured by DSC measurements. However, from both DSC and rheology curves of **1a** and **1b**, the formation of physical crosslinks by the perylene bisimide units cannot be clearly identified in the temperature range from 150 to 220 °C.

3D printing

For efficient transport through the driving wheels and the feeding zone, soft materials need a particular filament column strength. Therefore, tensile tests of fabricated filament rods were carried out. Stress-strain curves of injection-molded filament rods of **1a** and **1b** are shown in *Figure 24(a)*. The measured high E-Moduli of **1a** and **1b** provide sufficient stiffness required for feeding by extrusion-based 3D printers. In *Table 2*, mechanical properties of copolymer **1b** investigated on injection-molded filament rods, dog-bones punched out of compression-molded films, and dog-bones punched out of 3D printed square tube sidewalls are summarized. The E-moduli from different tensile specimens are very similar.

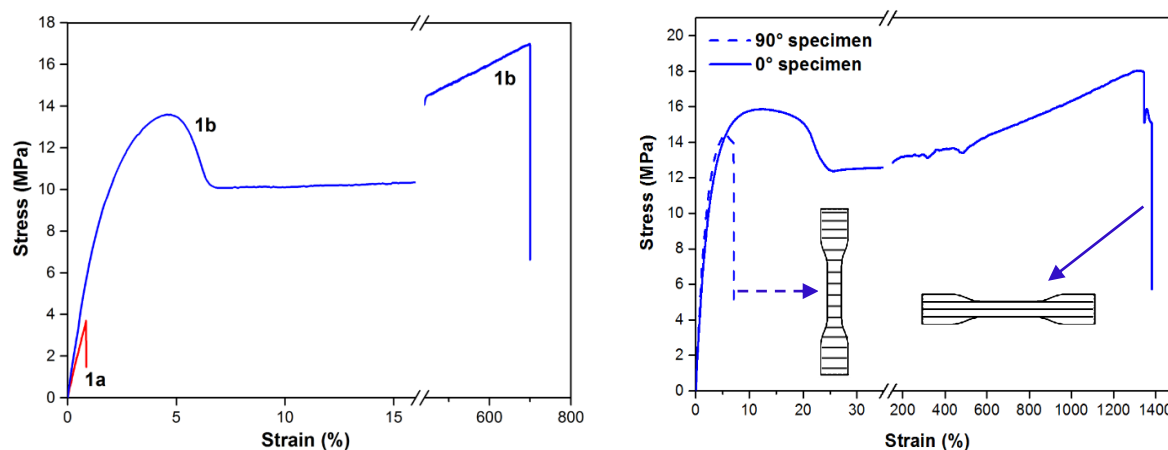


Figure 24: (left) Stress-strain curves of injection-molded filament rods of $(AB)_n$ segmented copolyetherimides **1a** and **1b**, (right) 90° and 0° test specimens punched out of sidewalls of a printed square tube with different orientation to z-direction

Table 2: Comparison of mechanical properties of 3D printed part with compression-molded films of $(AB)_n$ segmented copolyetherimides **1b**.

Sample	E [MPa] ^{a)}	σ_{br} [MPa] ^{b)}	ϵ_{br} [%] ^{c)}
3D printed part 90° ^{d)}	644 (54) ^{e)}	14.4 (0.2)	7.2 (0.2)
3D printed part 0°	659 (66)	18.2 (0.2)	1400 (60)
Compression-molded film ^{f)}	613 (51)	12.5 (0.3)	35 (0.5)

a) E-modulus; b) strength at break; c) elongation at break; d) orientation of tensile loading direction to layer deposition direction of punched dog-bones from 3D printed square tube; e) standard deviation in parentheses; f) Compression-molded film = dog-bone punched out of a compression-molded film;

4D printing

For a successful realization of a shape memory effect utilizing a thermoplastic material, two thermal transition temperatures are needed. The low thermal transition, $T_{trans.(low)}$, should be clearly above room temperature that fixation of a temporary shape is easily possible. The second thermal transition, $T_{trans.(high)}$, should be at a distinct higher temperature that the physical crosslinks are sufficiently stable at $T_{trans.(low)}$. To increase the aggregation of perylene bisimide segments, an additional polyetherimide with a higher perylene bisimide content, and Jeffamine® ED-900 segments was synthesized (see Figure 25). As **1b** showed excellent 3D printing performance and mechanical properties, a blend of **1b** and **2** was prepared in a 1:1 ratio (named as blend **3**) and processed into filament rods for 4D printing.

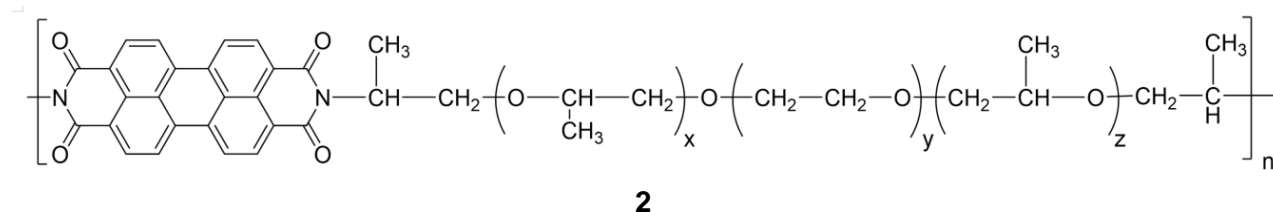


Figure 25: Chemical structure of synthesized $(AB)_n$ segmented copolyetherimide **2** with perylene bisimide and Jeffamine® ED-900 segments.

Rheological properties of blend **3** were measured and compared with **1b** and **2** in Figure 26. Blend **3** shows a combination of both properties by featuring a low and a high thermal transition, $T_{trans.(low)}$ and $T_{trans.(high)}$. The two transitions are at around 40 °C and 180 °C and should allow 3D printing above $T_{trans.(high)}$ and 4D printing between $T_{trans.(low)}$ and $T_{trans.(high)}$. Each thermal transition is observed as an evident change in viscosity within a narrow temperature range.

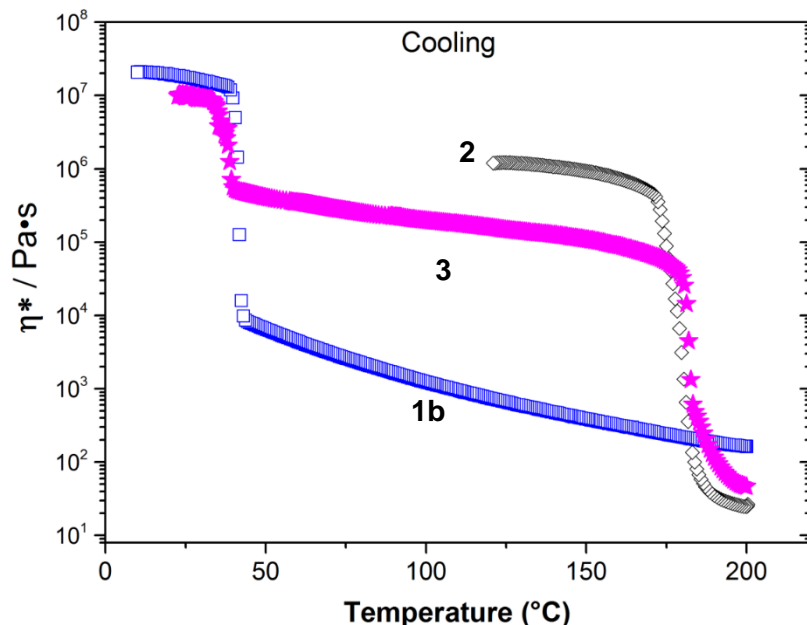


Figure 26: Oscillatory shear rheology measurements upon cooling of copolyetherimides blend **3**. The complex viscosity as function of the temperature is plotted for the blend components **1b** and **2**, as well as for the blend **3** itself.

In summary, the copolyetherimide blend **3** demonstrates a material properties combination of **1b** and **2**, features relative low melt viscosity, and thus allows 3D and 4D printing. To demonstrate 4D printing, a ring-shaped self-biting snake was 3D printed in its original shape utilizing blend **3**. From rheology measurements, $T_{\text{trans.}(low)}$ was determined below 60 °C as at this temperature crystallized PEG segments are completely melted. After heating at 60 °C for 5 min in an oven, the 3D printed ring-shaped snake was transferred into the temporary shape, an open ring-shaped snake, and in this shape cooled down in a refrigerator at about 5 °C (*Figure 27* middle). Due to physical crosslinks of aggregated perylene bisimide segments and recrystallized PEG segments, the achieved elastic deformation could be fixed as open ring-shaped snake. When the temporary shape is reheated at 60 °C for 3 min, the crystallized PEG segments are melted again, the stored elastic energy is released, and the original shape recovered (*Figure 27* right).



Figure 27: Demonstration of shape memory effect of 3D printed “U” form. The utilized 3D printing material is the blend of $(AB)_n$ segmented copolymers **1b** and **2** in a 1:1 ratio, named blend **3**.

4. Publications and manuscripts

4.1 List of publications and manuscripts

Publication 1:

“Filament materials screening for FDM 3D printing by means of injection molded short rods”

Minde Jin, Reiner Giesa, Christian Neuber and Hans-Werner Schmidt

published in *Macromolecular Materials and Engineering* **2018**, 303(12), 1800507

reprint and reuse of full paper with permission from *John Wiley and Sons*.

Publication 2:

“Tailoring polypropylene for extrusion-based additive manufacturing”

Minde Jin, Christian Neuber and Hans-Werner Schmidt

published in *Additive Manufacturing* **2020**, 33, 101101

reprint and reuse of full paper with permission from *Elsevier*.

Manuscript 3:

“(AB)_n segmented copolyetherimides for 4D printing”

Minde Jin, Markus Stihl, Reiner Giesa, Christian Neuber, Hans-Werner Schmidt

Submitted to *Macromolecular Materials and Engineering*.

4.2 Individual contributions to the publications

In the following section, the individual contributions of each author are specified. Work contributed by myself was carried out at the chair of Macromolecular Chemistry I at the University of Bayreuth and Key-lab of Bavarian Polymer Institute.

Publication 1: Filament materials screening for FDM 3D printing by means of injection molded short rods

Macromolecular Materials and Engineering **2018**, 303(12), 1800507

Minde Jin, Reiner Giesa, Christian Neuber and Hans-Werner Schmidt

The first manuscript was submitted for publication as a full paper article for establishing an efficient materials screening method for extrusion-based 3D printing by means of injection molded short filament rods. The processing and testing method presented in this manuscript was performed by myself. The 3D printed geometry and printing performances evaluation tests were developed together with Reiner Giesa and Christian Neuber. The first draft of the manuscript was written by myself with all data evaluation. Reiner Giesa, Christian Neuber, and Hans-Werner Schmidt were involved in scientific discussions of the results and finalizing of the manuscript.

Publication 2: Tailoring polypropylene for extrusion-based additive manufacturing

Additive Manufacturing **2020**, 33, 101101

Minde Jin, Christian Neuber and Hans-Werner Schmidt

The second manuscript was published as a full paper article and describes the tailoring of polypropylene for extrusion-based additive manufacturing. All investigated materials were firstly compounded and then fabricated into filament short rods. Compounding, processing, 3D printing, and testing methods presented in this manuscript were performed by myself with all data evaluation. I wrote the first draft of the manuscript. Christian Neuber and Hans-Werner Schmidt were involved in scientific discussions of the results and finalizing of the manuscript.

Manuscript 3: (AB)_n segmented copolyetherimides for 4D printing

Submitted to *Macromolecular Materials and Engineering*

Minde Jin, Markus Stihl, Reiner Giesa, Christian Neuber and Hans-Werner Schmidt

The third manuscript is intended for submission as a full paper article. Markus Stihl synthesized one copolymer, and I synthesized the other copolymers and prepared the copolymer blend. Analysis of copolymers by DSC, TGA, and DMA was done in joint work with Markus Stihl. Reiner Giesa investigated the rheological properties. The filament short rods were fabricated by myself using synthesized copolymers for mechanical testing. The 3D printing and all corresponding data evaluation were also done by myself. I wrote the first draft of the manuscript. Christian Neuber, Reiner Giesa, Markus Stihl, and Hans-Werner Schmidt were involved in scientific discussions of the results and finalizing of the manuscript.

4.3 Filament materials screening for FDM 3D printing by means of injection molded short rods

Filament Materials Screening for FDM 3D Printing by Means of Injection-Molded Short Rods



Minde Jin, Reiner Giesa, Christian Neuber,* and Hans-Werner Schmidt*

A miniature small-scale material processing and testing approach is developed as a screening method to evaluate polymer materials for fused deposition modeling (FDM). This method is suitable for a small material input of less than 10 g using a mini compounder in combination with an injection molding machine to manufacture short rods usable as FDM feedstock material. Compared with conventional continuous filament extrusion, where the amount of raw material required is around 1–5 kg, time and material consumption are both significantly reduced for the investigation of FDM filament materials or formulations. In order to demonstrate this method, three different polypropylene grades are processed into rods and compared to commercially available continuous filaments. In addition to warp deformation, interlayer bonding properties are also measured on test specimens punched out of FDM-printed square tubes. The presented rod preparation and square tube printing offer fast and efficient material screening and optimization for new FDM material development.

is usually supplied by a continuous feedstock filament spool driven by a material feeding system into the liquefier, where the material is softened and melted. A nozzle at the end of the liquefier extrudes and deposits the molten material in the X–Y plane.^[2] A computer which handles the layer construction information of the digital model file typically controls the movement of the nozzle. When one layer is finished, the nozzle starts to deposit new material on top of the previous layer by either lifting the nozzle or lowering the worktable by exactly one layer step height in the Z axis. Extruded material lines are fused together by mechanical pressure and thermal energy of the moving hot nozzle during printing.^[5] Processing variables such as nozzle temperature, nozzle path, and speed, as well as worktable temperature, are also adjustable by FDM setups and are critical for printed part performance.^[6]

1. Introduction

The idea in the American automotive industry of producing complex components within a very short time but without the need for sophisticated tooling is regarded as the first initiator of rapid prototyping (RP).^[1] Nowadays, numerous RP technologies are established which reduce the production time-to-market cycle and allow for more customized characteristics.^[2] The key principle of RP is summarized as layered manufacturing by sequential deposition of material in layers.^[3] Among all RP technologies, material extrusion additive manufacturing offers plunger-based, screw-based, and filament-based processing methods. However, filament-based fused deposition modeling (FDM) is one of most widely used processes due to its cost-effectiveness and simplicity.^[4] The FDM technology is supported and implemented by a simplified thermoplastic extrusion process combined with computer-numerical-controlled technology. This process utilizes the melting and resolidification properties of thermoplastic materials in heating and cooling.^[5] The material

Typical FDM materials are common thermoplastic polymers such as polylactic acid (PLA), acrylonitrile-butadiene-styrene (ABS), and polyetherimide (PEI, Ultem). These are the most representative examples targeting hobby and all-purpose markets as well as high-performance engineering parts.^[7–9] However, for functional applications, the anisotropic mechanical property caused by layer manufacturing is a typical drawback and limitation of FDM-fabricated parts compared to conventionally extruded and injection-molded objects.^[2,10]

Most popular FDM materials are amorphous (ABS, PEI, acrylonitrile-styrene-acrylate-copolymers (ASA), polycarbonate). Only a few semi-crystalline polymers with a low degree of crystallinity (PLA and Nylon) are available as FDM filaments.^[7,11–14] Hence, there is a need for commodity semi-crystalline plastic for FDM technology.

In this context, polypropylene (PP) is the most common semi-crystalline thermoplastic polymer material used in consumer and technical products. It features exceptional mechanical properties, outstanding processability, high chemical resistance, low density, and all this at reasonable costs. In addition, PP can be readily modified for various applications.^[15] These modifications can be performed by copolymerization with ethylene, as well as by compounding with additives and fillers.^[16] Polypropylene-ethylene random copolymers (raco PP) play an important role in applications such as film and rigid packing.^[17] The advantages of raco PP are improved transparency, relative softness, and better impact strength at lower temperatures due to lower degree of crystallinity caused by the ethylene

M. Jin, Dr. R. Giesa, Dr. C. Neuber, Prof. H.-W. Schmidt
Macromolecular Chemistry I & Bavaria Polymer Institute (BPI)
University of Bayreuth
Universitätsstraße 30, 95447 Bayreuth, Germany
E-mail: christian.neuber@uni-bayreuth.de; hans-werner.schmidt@uni-bayreuth.de

The ORCID identification number(s) for the author(s) of this article can be found under <https://doi.org/10.1002/mame.201800507>.

DOI: 10.1002/mame.201800507

units, which also makes it promising for FDM processing.^[18] Only a few research studies have focused on FDM with PP since semi-crystalline polymers such as PP exhibit high volumetric shrinkage upon cooling, resulting in poor printing and large warp deformation. This warping of semi-crystalline FDM printed parts is always observed but it is less significant and more tolerable with the use of amorphous materials.^[19,20]

For the development of FDM feedstock materials, the neat polymers were compounded and processed using standard single-screw filament extrusion lines.^[21–29] The use of such lines requires considerable time and at least 1 kg material for an extrusion process optimization to achieve satisfying filament quality for further FDM printing. For instance, Carneiro et al. used a glass fiber reinforced standard injection molding grade of isotactic PP (iPP) as a filament for FDM.^[24] Hertle et al. also used iPP while studying the influences of FDM processing conditions on printed part mechanical properties.^[30] M. Spoerk et al. used a PP copolymer for filament extrusion and added different types of fillers.^[25,27–29] In these studies, they investigated the dimensional stability and volumetric shrinkage of printed parts bonded to the build surface. However, the mechanical properties of investigated materials were determined directly on filaments and no interlayer bonding studies were included. Another author evaluated mechanical properties by directly using a printed test specimen, which is, however, affected by the anisotropic properties of the printed part.^[2] In a study by Graybill et al., a free-standing square tube was used for the evaluation of interlayer bonding quality.^[31] Here the test specimens were manually cut out of a printed side wall and the required material amount was significantly reduced by printing this geometry.

Until now, there has been no effective FDM material screening method for new semi-crystalline polymers or compounds combining material processing and the evaluation of part performance, such as warping and interlayer bonding.

The scope of this work is to develop a processing method requiring small amounts of a polymer in combination with a printed thin-wall geometry for FDM material screening. To realize this, a small amount of polymer (from 10 to 50 g) is compounded and injection-molded into short filament rods instead of extruding a continuous, endless filament. To demonstrate the advantages of this method, different types of semi-crystalline polypropylenes were employed. Furthermore, a printed square tube geometry was developed to investigate the FDM performance as a function of polymer type, material composition, and printing parameters. This geometry is based on a free-standing, open, square tube with cubic dimensions, consisting of only a single-line stack. The printability and printed part performance, such as warp deformation and interlayer bonding, were evaluated. By applying this method, material, time, and cost are minimized for screening and developing new FDM materials in the early stage.

2. Experimental Section

2.1. Materials

In this work, two commercial continuous PP filaments serve as a reference: from Reprap Germany (denoted *PP filament 1*),

and from Popbit, China (denoted *PP filament 2*). The other three PP types were supplied as a fine powder or pellets: iPP Pro-fax PH350 (density at 23 °C): 0.90 g cm⁻³, melt flow rate (230 °C/2.16 kg) 3.5 g/10 min^[32] (denoted iPP) from LyondellBasell, USA; RF365MO a polypropylene/ethylene random copolymer (density at 23 °C): 0.905 g cm⁻³, melt flow rate (230 °C/2.16 kg) 20.0 g/10 min^[33] (raco PP 1), and RD208CF (density at 23 °C): 0.90 g cm⁻³, melt flow rate (230 °C/2.16 kg) 8.0 g/10 min^[34] (raco PP 2) from Borealis, Austria. In addition, ABS, a commonly used FDM continuous filament material (tradename: smartABS) from Orbi-tech, Germany, was also printed as a reference.

2.2. Lab-Scale Rod Processing

The feedstock materials for FDM were compounded and injection-molded into short rods. The compounding step enables the development of new feedstock materials involving compounds with other polymers, additives, and fillers. PP fine powder or pellets were each compounded for 5 min under nitrogen atmosphere in a co-rotating twin-screw micro-compounder (DSM Xplore, 15 mL) at a rotational speed of 40 rpm and a temperature of 240 °C. This compounding step results in a homogenous polymer melt for the injection molding step. The melt was discharged and filled directly into the barrel of a DSM injection molding machine and injected into a metal mold containing a Teflon tube (length: 140 mm, outer diameter: 4.0 mm, inner diameter: 3.0 mm). Thus, the final dimension of the injected rods is very precisely controlled by the tube dimensions. The melt temperature was set to 235 °C, the mold temperature to 23 °C, and the injection/holding pressure was 6 bar for 5 s. The Teflon tube was removed from the mold and a new tube was inserted for the next injection cycle. After removing the Teflon tube by cutting, both ends of the rods were cut with a rotary microtome (RM2255 from Leica Co.) with a step length of 25 µm to obtain flat cross sections linking individual rods without a gap. Each polymer filament rod is around 135 to 140 mm long and weighs around 0.85 g.

2.3. FDM Printer and Geometry Design

The FDM 3D printer used in this study is a desktop twin-nozzle (nozzle diameter: 400 µm) FDM printer (3NTR A4, Italia). In order to use the rods for printing, the filament supply system was modified by aligning the feeding tube vertically.

The 3D digital model of the geometry to be printed was first designed (Autodesk Inventor 2014) and additionally sliced (Slic3r) into digital layers. This geometry is designed as a free-standing square tube (5 cm × 5 cm in size) consisting of only a single-material stack with a line thickness of around 600 µm. This means that, within each layer, the nozzle moves one square path and extrudes a single material line. For the printing process, the printing bed material was either an epoxy resin hole-plate or glass (see **Table 1**); on top of the bed, two thin layers of the same material were printed. Six rods were necessary to print one square tube requiring less than 10 g of material for one run.

Table 1. Optimized printing variables for investigated iPP, raco PPs, and ABS.

Parameter	iPP rod	raco PP 1 rod	raco PP 2 rod	PP 1 filament	PP 2 filament	ABS filament
Nozzle temperature [°C]	240	250	250	250	250	260
Bed temperature [°C]	120	120	120	120	120	120
Printing speed [mm s ⁻¹]	15	15	15	15	15	15
Layer height [μm]	250	250	250	250	250	250
Fan speed [%]	100	100	100	100	25	100
Printing bed material		epoxide resin hole-plate				glass

2.4. Pre-Optimization of PP FDM Processing

To achieve dimensionally stable and defect-free FDM printed parts, each FDM procedure has to be optimized regarding processing variables, such as extruder and bed temperature, printing and cooling fan speed, for any particular feedstock material. The printed geometry for this pre-optimization was also a square tube and the criteria for optimization were less warp deformation and better part finishing using a visual qualitative evaluation. Over the course of a series of printing runs, the most important processing variables, such as nozzle temperature and cooling fan speed, were optimized (Table 1).

2.5. Warp Deformation Measurement

Warping of the side walls is defined by the distance d_{warp} between the maximum deformation of a printed square tube and the non-deformation contour of an ideally shaped square tube (Figure 1). To mimic the ideal non-deformation contour, a rigid flat plate was attached to the side wall as a reference. The distance between the deformed surface and reference plate was measured using a digital caliper (Mahr Digital Calipers 16 ES, measuring range 150 mm, resolution 0.01 mm). Each side was measured twice, resulting in eight different positions on the side walls of each square tube.

2.6. Mechanical Testing

For mechanical testing, the square tubes were cut into four side walls using a CO₂ laser cutter. In this work, five tensile specimens were punched out (Coesfeld Material Test Inc., knife for tensile specimen DIN 54504 S3A) of each side wall at angles of 90° and 0° to the layer deposition direction (X- and Y-axis) and used to determine interlayer bonding and bulk mechanical properties. Tensile tests were performed on an Instron 5565 universal tester using a 1 kN load cell and pneumatic clamps. The thickness of the specimens was measured with a digital micrometer (Mitutoyo 293–831, digimatic MDC Lite) in the range of 600 to 650 μm. The E-Moduli of all specimens were investigated at a strain rate of 0.2 mm min⁻¹ and calculated between 0.1% and 0.3% strain. Then a strain rate of 2.0 mm min⁻¹ or 40.0 mm min⁻¹ was applied for 90° and 0° specimens, respectively. In addition, the surface roughness

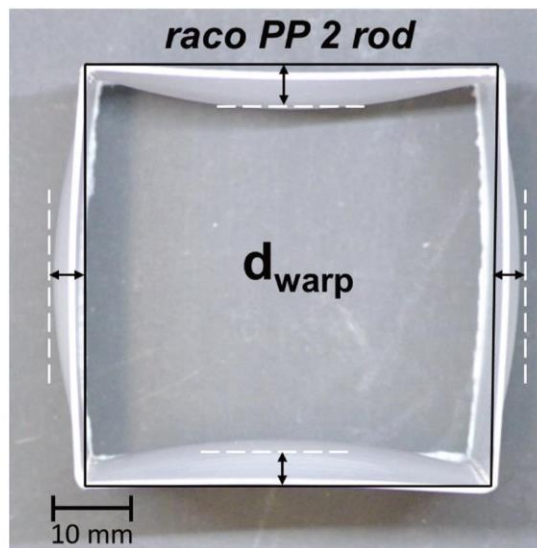


Figure 1. Definition of warp deformation as observed from the top view of a printed square tube of raco PP 2 rod. The distance between the ideal non-deformation square contour (black line) and the maximum deformation position of each side wall (white dashed line) was measured and averaged for the reported geometric deformations, noted as d_{warp} .

of each side wall was determined with a stylus profilometer (Veeco DEKTAk 150 profilometer) in combination with WYKO Vision software to analyze the surface roughness data. The surface profile height R_z is defined as the 10 points average distance between peaks (five highest points) and valleys (five lowest points) of the surface profile measured along the layer deposition direction (Z axis).^[35,36] The thickness measured with a digital micrometer (Mahr 16ES MOD. S225) is regarded as overall thickness δ_{meas} of the fused material. The thickness of the tensile specimens refers to the effective bonding thickness δ_{eff} between the individual layers as shown in Figure 2b. For 90° specimens, the difference between the measured thickness and bonding thickness can be approximated by twice the surface profile height: $2R_z = \delta_{\text{meas}} - \delta_{\text{eff}}$, and hence the mechanical properties were calculated using the specimen cross section area $A^{90^\circ} = b (\delta_{\text{meas}} - 2R_z)$, where $b = 4$ mm is the width of the test specimen. However, for 0° specimens, the cross section A^{0° is calculated by using the value of one profile height R_z to $A^{0^\circ} = b (\delta_{\text{meas}} - R_z)$.

2.7. Thermal Analysis

Thermal analysis was conducted using a Mettler Toledo DSC 2 STAR^e system under nitrogen atmosphere ramping from 25 to 250 °C at a heating/cooling rate of 10 K min⁻¹. The degree of crystallization of FDM printed samples was determined by cutting a small piece out of the center area from the side wall. Only the first heating curve was used for the calculation of the degree of crystallization according to Equation (1):

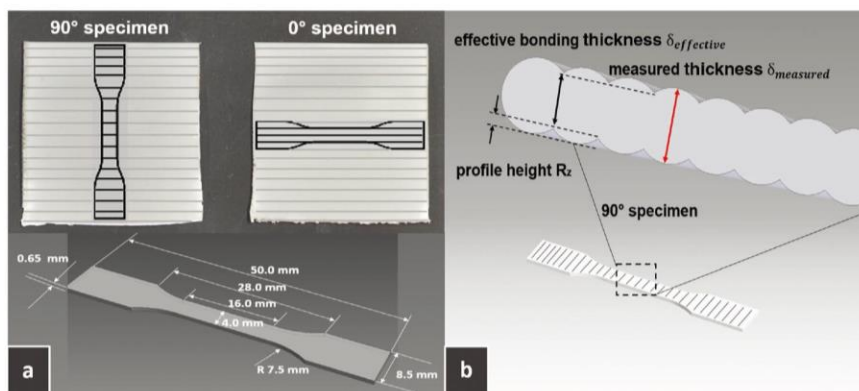


Figure 2. a) Specimens (nominal tensile specimen dimensions according to DIN 53504-S3a standard) were punched out, resulting in two different tensile specimens for evaluating the interlayer bonding quality (90° specimens, layer deposition direction (grey lines) perpendicular to tensile loading direction) and the material intrinsic properties (0° specimens, layer deposition direction (grey lines) parallel to tensile loading direction). b) Illustration of effective bonding thickness and measured thickness by utilizing a screw micrometer with a 90° specimen. Here the tensile load is applied directly to the interlayer bonding area.

$$X_c = \frac{\Delta H_m}{\Delta H_{m,0}} \quad (1)$$

where ΔH_m is the measured melting enthalpy and $\Delta H_{m,0}$ is the melting enthalpy of a 100% crystalline PP (207 J g⁻¹) as known from literature.^[5]

3. Results and Discussion

3.1. Lab-Scale Feedstock Rod Processing

Figure 3 shows the entire processing sequence from raw material to feedstock rods and their use as FDM printing material. The main advantage of the presented method is seen in the fabrication of rods with a well-defined and reproducible geometry, requiring only a small amount of raw material followed by the printing process.

First, around 8.5 g raw material is compounded in a conical mini mixer and then injection-molded into six individual rods. Since the polymer melt is injected molded into a Teflon tube, the rods exhibit a very uniform diameter. Figure 3 shows details

of four rods (*raco PP 2*). After removing the Teflon tubes, all the rods were cut to a length of about 14 cm.

3.2. 3D Printing and Characterization

To use the rods in an FDM process, the filament supply system was modified by turning the feeding tube vertically to achieve a close connection without a gap among the individual rods. This modification resulted in a constant, smooth, and continuous transport of the individual rods into the printer. Thus, the entire FDM printing process remains similar to printing a commercial continuous FDM filament. Three different PP grades were processed into rods (*iPP rod*, *raco PP1 rod*, and *raco PP2 rod*) and 3D printed. For comparison, commercial continuous filaments (*ABS filament*, *PP1 filament*, and *PP2 filament*) were also printed into square tubes via FDM.

The geometry of the square tube was chosen due to its simplicity and small amount of material consumption. With this thin-wall, single-layer geometry, the side wall warp deformation is greatly pronounced and allows the visualization and quantitative evaluation using simple geometric measurements.

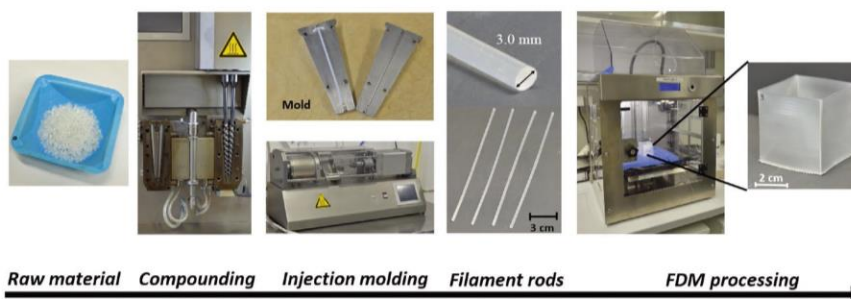


Figure 3. Sequence of the fabrication of rods for FDM material screening. The raw material is first compounded in a mini mixer and then injection-molded into Teflon tubing, rendering individual filament rods. These are then fed into a FDM 3D printer and printed into square tubes.

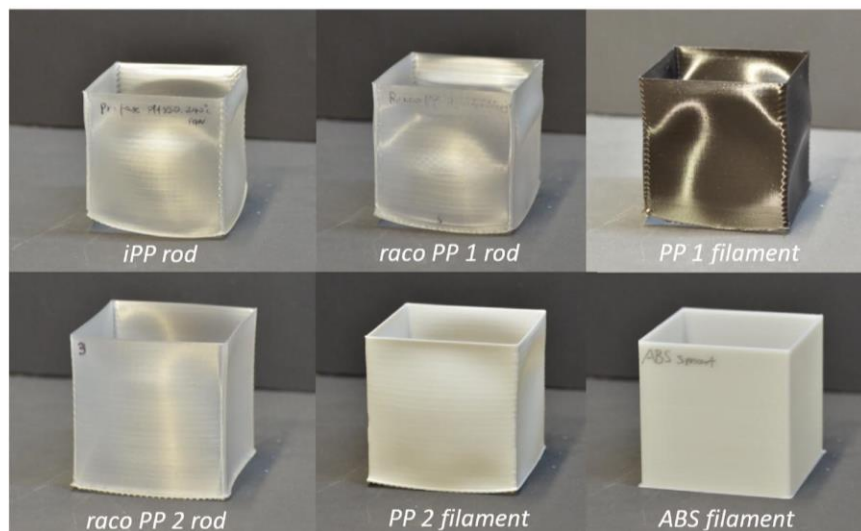


Figure 4. FDM printed square tube geometries of different polypropylene grades compared with amorphous ABS. PP exhibits significant warp deformation whereas ABS can be printed without visible warp deformation.

Additionally, tensile tests of specimens along and perpendicular to the printing direction will provide direct information about the layer bonding strength.

In **Figure 4**, images of FDM-printed square tubes are depicted. Here, the extent of warp deformation is clearly visible, with PP exhibiting pronounced warp deformation and ABS, a common reference FDM filament material, being almost warp-free. A quantitative analysis of the warping is listed in **Figure 5**.

Figure 1 depicts the side wall warp deformation from a top view (*raco PP 2 rod*). The distance between the maximum deformation point (white dashed line) and the ideal non-deformation contour (black line) corresponds to the warp deformation value. Two measurements were performed per side wall and the values averaged for the reported geometric deformations, noted as d_{warp} .

Figure 5 summarizes the measured averaged values of warp deformation (d_{warp}) for all side walls. The *iPP rod* material with

the highest degree of crystallization and stiffness exhibits the highest geometric deformation, followed by the different *raco PP* grades. The improved printed part quality of the three investigated *raco PP*s can be attributed to their significantly lower degree of crystallization. Warping is mainly governed by the shrinkage-induced residual inner stress and primarily depends on the elasticity modulus and linear shrinkage coefficient.^[5] Thus, a lower E-modulus and reduced degree of crystallization result in less part warping for semi-crystalline polymers. Consequently, *PP 2 filament* with about 20% degree of crystallization shows the least geometric deformation of all investigated PP and *raco PP* grades. In summary, small lab-scale rod manufacturing in combination with FDM printing into a single layer square tube geometry offers a fast and efficient evaluation of geometric warp deformation of new feedstock materials. The data demonstrate that d_{warp} correlates with the degree of crystallization.

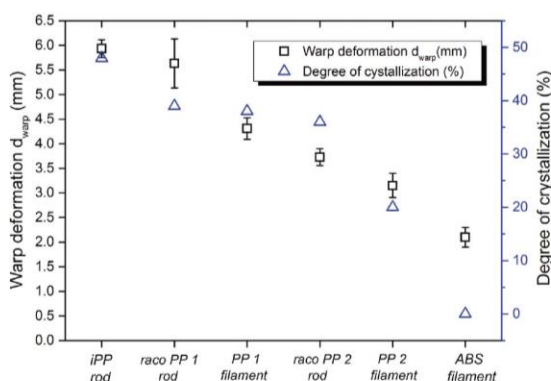


Figure 5. Warp deformation (d_{warp}) and degree of crystallization (measured by DSC) of different grades of PPs, *raco PP*s, and reference filament ABS.

3.3. Mechanical Properties

A mechanical characterization of FDM parts requires a side wall separation of the square tube into four single side wall pieces, which was accomplished with a laser cutter (see **Exp. Part**). Then a maximum of five dog bones as test specimens (**Figure 2a**) were punched out from each of the four side walls with angles of 90° and 0° to the layer deposition direction (X- and Y-axis). For 90° specimens, the tensile loading direction is perpendicular to the layer deposition direction and the load is applied to the interlayer bonding area. For the 0° specimen, the load is longitudinal to the deposited layers.

A thin wall, in combination with tensile specimens punched in different directions, avoids the complexity of contour and infill deposition techniques for producing discrete FDM test specimens and thus permits the reliable

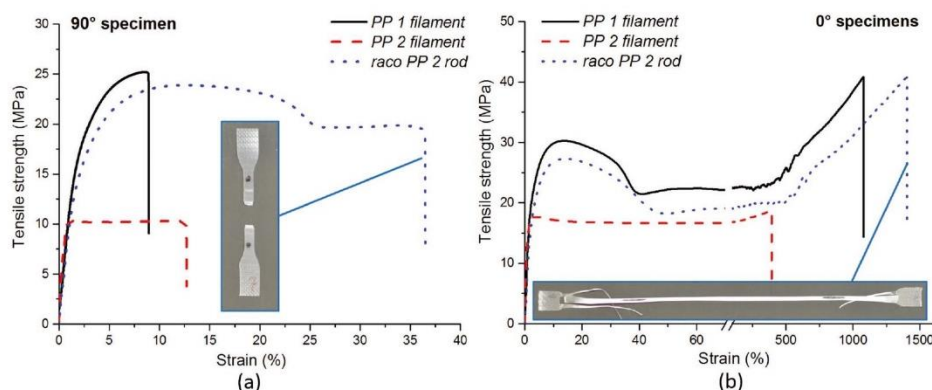


Figure 6. a) Tensile curves of 90° specimens and b) 0° specimens of three different PP grades (PP 1 filament: solid line, PP 2 filament: dashed line, raco PP 2 rod: dotted line) and images of failed dog bones (from raco PP 2 rod).

measurement of mechanical properties. However, when calculating the mechanical properties, the true specimen thicknesses for both 90° specimens and 0° specimens are required. As shown in Figure 2b and defined in Section 2.6, when calculating the mechanical properties of 90° specimens, the effective bonding thickness is the measured thickness minus twice the profile height R_z . For 0° specimens, the measured thickness minus one profile height was used for the thickness calculation.

Mechanical characterization was conducted using three selected square tubes printed from *PP 1 filament*, *PP 2 filament*, and *raco PP 2 rod* showing the lowest geometric deformations (d_{warp} , Figure 1). **Figure 6** depicts representative strength–strain curves of different PPs and **Table 2** summarizes the details of tensile testing.

Interlayer bonding is most critical for the toughness of an FDM printed part and typically the printing direction causes pronounced anisotropic behavior. In this work, the interlayer bonding quality is assessed by comparing the tensile testing results of 90° and 0° specimens. All 90° specimens in Table 2 show much lower elongation at break ϵ_{br} than 0° specimens, which is due to the poor adhesion of interlayers among the sequentially deposited layers. The image in Figure 6a of tested 90° specimens shows a clear and even

fracture among an interlayer in the center of specimen. The *raco PP 2 rod* shows the highest bonding quality with an elongation (ϵ_{br}) of around 36%. The *PP 1 filament* and *PP 2 filament* exhibit elongations at break (ϵ_{br}) of around 10% and 12%, respectively, and hence inferior bonding performance. The Young's moduli (E) of 90° specimens are around 10% to 20% lower than the 0° specimens. This is in agreement with other studies of tensile specimens with different raster orientation.^[2,37–39] In Figure 6b, two curves of typical strong and tough properties of bulk PP are observable as the 0° specimens consist of parallel-oriented fused ribbons along the tensile loading direction. The two investigated raco PP materials show similar mechanical properties of 0° specimens with a strain hardening effect due to molecular chain orientation. Blended with a soft and incompatible PE component, the *PP 2 filament* demonstrates a dramatically lower tensile strength and ultimate strain due to phase separation.^[40] Compared with the smooth fracture surface of the 90° specimen, the 0° specimen shows irregular failure of ribbons. As a conclusion, punched specimens out of a square tube side wall of 90° and 0° orientations to the printing direction offer an alternative, efficient means to investigate the interlayer bonding quality and mechanical properties of FDM filament materials.

Table 2. Tensile properties of PP 1 filament, PP 2 filament, and raco PP 2 rod as a function of the layer deposition direction in FDM printed square tubes.

Material	E [MPa] ^{a)}	σ_{yi} [MPa] ^{b)}	σ_{br} [MPa] ^{c)}	ϵ_{br} [%] ^{d)}
PP 1 filament 90°	1028 (162) ^{e)}	18.9 (0.9)	18.9 (0.9)	9.5 (3.9)
PP 1 filament 0°	1073 (203)	28.4 (2.9)	41.5 (5.5)	405 (73)
PP 2 filament 90°	1050 (165)	10.5 (0.1)	10.5 (0.1)	12.0 (4.0)
PP 2 filament 0°	1267 (110)	16.1 (0.3)	16.7 (0.6)	1170 (80)
raco PP 2 rod 90°	828 (21)	23.9 (0.2)	23.9 (0.2)	35.9 (5.1)
raco PP 2 rod 0°	900 (130)	27.3 (0.4)	34.3 (3.9)	1400 (20)

^{a)}Young's modulus; ^{b)}strength at yield; ^{c)}strength at break; ^{d)}elongation at break; ^{e)}standard deviation in parentheses.

4. Conclusions

A new lab-scale feedstock rod processing method for FDM material screening was presented. This method allows feedstock rods to be processed from a limited amount (from 10 to 50 g) of a newly developed material by using a mini compounder and an injection molding machine. With the help of a Teflon tube as a mold, the manufactured rods demonstrated uniform diameters and were successfully printed with an FDM printer. Three different grades of PP were processed into PP FDM rods and then compared with two commercial

PP FDM continuous filaments with respect to printed part characteristics, such as geometric deformation, degree of crystallization, and mechanical properties, later resulting in the anisotropic bonding strength. A printed free-standing square tube consisting of only a single-material-line stack was used for the visualization and evaluation of material-shrinkage-induced warp deformation. iPP with a relatively high degree of crystallization and stiffness demonstrated the most severe geometric deformation. Here, a selected polypropylene-ethylene random copolymer with a lower degree of crystallization and stiffness exhibited reduced geometric deformation, while a commercial polypropylene/polyethylene blend material with the lowest degree of crystallization featured the least geometric deformation of printed parts. In addition, the interlayer bonding strength of selected PP materials was also determined utilizing small-scale tensile specimens punched out of printed square tube side walls. As a conclusion, the presented method enables FDM rods to be manufactured efficiently from only a small amount of raw material. In addition, the punched-out test specimens provide a reliable analysis of the printed part performance for screening and development of new FDM materials.

Conflict of Interest

The authors declare no conflict of interest.

Keywords

3D printing, fused deposition modeling, interlayer bonding, polypropylene feedstock filament rods, warp deformation

Received: August 21, 2018

Revised: September 27, 2018

Published online: October 19, 2018

- [1] S. Upcraft, R. Fletcher, *Assem. Autom.* **2003**, 23, 318.
- [2] S. Ahn, M. Montero, D. Odell, S. Roundy, P. K. Wright, *Rapid Prototyping J.* **2002**, 8, 248.
- [3] A. H. Nickel, D. M. Barnett, F. B. Prinz, *Mater. Sci. Eng., A* **2001**, 317, 59.
- [4] J. Gonzalez-Gutierrez, S. Cano, S. Schuschnigg, C. Kukla, J. Sapkota, C. Holzer, *Materials* **2018**, 11.
- [5] T.-M. Wang, J.-T. Xi, Y. Jin, *Int. J. Adv. Manuf. Technol.* **2007**, 33, 1087.
- [6] Q. Sun, G. M. Rizvi, C. T. Bellehumeur, P. Gu, *Rapid Prototyping J.* **2008**, 14, 72.
- [7] Stratasys Co., FDM Thermoplastics: Find your FDM thermo-plastic, <http://www.stratasys.com/de/materialien/fdm> (accessed: September 2018)
- [8] R. J. Zaldivar, D. B. Witkin, T. McLouth, D. N. Patel, K. Schmitt, J. P. Nokes, *Addit. Manuf.* **2017**, 13, 71.
- [9] Makerbot Co., Makerbot Homepage, <https://www.makerbot.com> (accessed: August 2018).
- [10] V. Kishore, C. Ajinjeru, A. Nycz, B. Post, J. Lindahl, V. Kunc, C. Duty, *Addit. Manuf.* **2017**, 14, 7.
- [11] A. Bagsik, V. Schöppner, E. Klemp, *14th international scientific conference on polymeric materials* **2010**, Halle (Saale).
- [12] R. Melnikova, A. Ehrmann, K. Finsterbusch, *IOP Conf. Ser.: Mater. Sci. Eng.* **2014**.
- [13] S. H. Masood, K. Mau, W. Q. Song, *Mater. Sci. Forum* **2010**, 654-656, 2556.
- [14] R. Singh, S. Singh, *J. Inst. Eng. (India): Series C* **2014**, 95, 103.
- [15] D. B. Malpass, E. I. Band, *Introduction to Industrial Polypropylene: Properties, Catalysts, Processes*, John Wiley & Sons, Salem, Massachusetts **2012**.
- [16] J. Karger-Kocsis (editor), *Polypropylene Structure, Blends and Composites: Volume 3 Composites*, Chapman and Hall Inc., London **1995**.
- [17] M. Gahleitner, P. Jääskeläinen, E. Ratajski, C. Paulik, J. Reussner, J. Wolfschwenger, W. Neißl, *J. Appl. Polym. Sci.* **2005**, 95, 1073.
- [18] W. Tang, J. Tang, H. Yuan, R. Jin, *J. Appl. Polym. Sci.* **2011**, 122, 461.
- [19] P. K. Gurrula, S. P. Regalla, *Virtual Phys. Prototyping* **2014**, 9, 127.
- [20] J. M. Fischer, *Handbook of Molded Part Shrinkage and Warp*, Plastics Design Library/William Andrew Pub, Norwich, New York **2003**.
- [21] J. Corney, S. H. Masood, W. Q. Song, *Assem. Autom.* **2005**, 25, 309.
- [22] S. Masood, W. Song, *Mater. Des.* **2004**, 25, 587.
- [23] R. Singh, S. Singh, F. Fraternali, *Composites, Part B* **2016**, 98, 244.
- [24] O. S. Carneiro, A. F. Silva, R. Gomes, *Mater. Des.* **2015**, 83, 768.
- [25] M. Spoerk, J. Sapkota, G. Weingrill, T. Fischinger, F. Arbeiter, C. Holzer, *Macromol. Mater. Eng.* **2017**, 302, 1700143.
- [26] S. Dul, L. Fambri, A. Pegoretti, *Composites, Part A* **2016**, 85, 181.
- [27] M. Spoerk, F. Arbeiter, I. Raguž, G. Weingrill, T. Fischinger, G. Traxler, S. Schuschnigg, L. Cardon, C. Holzer, *Macromol. Mater. Eng.* **2018**, 303, 1800179.
- [28] M. Spoerk, C. Savandaiah, F. Arbeiter, J. Sapkota, C. Holzer, *Polym. Compos.* **2017**, 83, 768.
- [29] M. Spoerk, C. Savandaiah, F. Arbeiter, G. Traxler, L. Cardon, C. Holzer, J. Sapkota, *Composites, Part A* **2018**, 113, 95.
- [30] S. Hertle, M. Drexler, D. Drummer, *Macromol. Mater. Eng.* **2016**, 307, 1482.
- [31] B. Graybill, *Development of a Predictive Model for the Design of Parts Fabricated by Fused Deposition Modeling*: Master Thesis at University of Missouri-Columbia **2010**.
- [32] Lyondellbasell, "Pro-fax PH350: Technical Data Sheet," <https://www.lyondellbasell.com/en/polymers/p/Pro-fax-PH350/a38a1948-55a3-4078-be2a-3048b25fc6af> (accessed: September 2017).
- [33] Borealis Co., RF365 MO: Product Data Sheet, <http://www.borealisgroup.com/en/polyolefins/products/Others/RF365MO/>, (accessed: September 2018).
- [34] Borealis Co., RD208CF: Product Data Sheet, <http://www.borealisgroup.com/en/polyolefins/products/Others/RD208CF/>, (accessed: September 2018).
- [35] Veeco Co., Surface Measurement Parameters for Wyko Optical Profilers, Veeco Instruments Inc, http://zeus.plmsc.psu.edu/~manias/MatSc597/docs/di_roughness.pdf (accessed: September 2018).
- [36] E. S. Gadelmawla, M. M. Koura, T. Maksoud, I. M. Elewa, H. H. Soliman, *J. Mater. Process. Technol.* **2002**, 123, 133.
- [37] J. F. Rodríguez, J. P. Thomas, J. E. Renaud, *Rapid Prototyping J.* **2001**, 7, 148.
- [38] A. S. El-Gizawy, S. Corl, B. Graybill, *InProceedings of the ICMET, International Conference on Mechanical Engineerings and Technology Congress & Exposition* **2011**.
- [39] C. Ziemian, M. Sharma, S. Ziemian, *InTech* **2012**, <https://doi.org/10.5772/34233>.
- [40] J. W. Teh, *J. Appl. Polym. Sci.* **1983**, 28, 605.

4.4 Tailoring polypropylene for extrusion-based additive manufacturing

Additive Manufacturing 33 (2020) 101101



Contents lists available at ScienceDirect

Additive Manufacturing

journal homepage: www.elsevier.com/locate/addma

Full Length Article

Tailoring polypropylene for extrusion-based additive manufacturing

Minde Jin, Christian Neuber*, Hans-Werner Schmidt*



Macromolecular Chemistry I and Bavarian Polymer Institute (BPI), University of Bayreuth, Universitätsstraße 30, 95447, Bayreuth, Germany

ARTICLE INFO

Keywords:

Fused filament fabrication (FFF)
 Polypropylene
 Warp deformation
 Interlayer bonding
 Anisotropic property of 3D printed parts

ABSTRACT

This paper reports on the optimization of polypropylene (PP) feedstock material towards extrusion-based additive manufacturing. To achieve this, two commercially available grades of polypropylene/ethylene random copolymers (raco PP) were modified, aiming to reduce warp deformation caused by shrinkage and at the same time reduce the anisotropic property by improving the interlayer bonding quality of 3D printed parts processed by fused filament fabrication (FFF). A β -nucleating agent, several amorphous polypropylenes (aPP) and one linear low-density polyethylene (LLDPE) were selected as additive or blending component with the goal to reduce shrinkage. The polypropylene feedstock material optimization was conducted by a combination of a lab-scale filament rod processing method and utilizing printed square tubes to optimize printing performance. The achieved results demonstrate that the crystallization behavior and E-modulus of polypropylene play significant roles for warp deformation in extrusion-based 3D printed parts. The β -nucleating agent alters the crystallization behavior, even a slightly negative influence on the warp deformation was observed. The investigated polymer blend of raco PP and LLDPE shows no significant contribution to reduce warpage and impairs also the interlayer bonding. The best results were achieved by blending raco PP with selected amorphous PPs. With two aPP grades warp deformation could be drastically reduced. In addition, the interlayer bonding quality is remarkably enhanced in these blends in spite of slight decreases in stiffness and strength. In conclusion, the optimized PP feedstock material features less warp deformation, high stiffness, and most importantly, outstanding interlayer bonding qualities.

1. Introduction

Thermoplastics are polymer materials which can be melt processed several times or re-casted by utilizing their melting and re-solidification properties [1,2]. The thermoplastic market occupies over 10 % of the global market in the chemical industry and over 90 % of all polymer materials. In addition, the thermoplastic market belongs to the most rapidly growing part of the world economy. Nowadays, one of the new driving forces is the need for tailored thermoplastic materials due to the emergence of revolutionary technologies such as 3D printing technologies [3].

Rapid prototyping (RP) using 3D printing, also reported as additive manufacturing (AM), makes it possible to produce parts layer by layer using a digital model totally without the need of tooling [4]. During the last three decades, numerous 3D printing technologies, each with their own specific advantages, were developed to shorten the production development cycle and produce customized parts with defined functionality and individuality [5]. For most 3D printing technologies, the concept is summarized as AM via sequential material deposition with the basic principle: layer by layer [6]. Among 3D printing technologies,

extrusion-based additive manufacturing, also known as fused deposition modeling (FDM) or fused filament fabrication (FFF), is one of most widely-used processes. Here, a simplified thermoplastic extrusion process in combination with computer-numerical-controlled (CNC) technology provides cost-effective layered processing of 3D printed parts. For extrusion-based additive manufacturing, special thermoplastic materials are needed, which are usually supplied as a continuous feedstock filament which is driven by a feeding system into the FFF liquefier [7]. The softened and melted material from the liquefier is deposited in the X–Y plane through a nozzle with a typical diameter of 400 μm [5]. A digital model file defines the movements of the nozzle. When the current printing layer is finished, the next layer starts on top of the previous layer after lifting the nozzle or lowering the worktable by just one layer step height in the Z axis. The successively deposited material strands are fused together during printing by thermal energy and mechanical pressure of the moving hot nozzle [7]. Nozzle temperature, worktable temperature, as well as nozzle path and speed are critical processing variables which influence the final printed part performance [8].

In the polymer class of thermoplastics, the commodity plastic group

* Corresponding authors.

E-mail addresses: christian.neuber@uni-bayreuth.de (C. Neuber), hans-werner.schmidt@uni-bayreuth.de (H.-W. Schmidt).<https://doi.org/10.1016/j.addma.2020.101101>

Received 20 August 2019; Received in revised form 24 January 2020; Accepted 30 January 2020

Available online 31 January 2020

2214-8604/ © 2020 Published by Elsevier B.V.

is used in largest quantities for everyday things due to their cost-effectiveness in combination with mid-range mechanical properties [3]. Most notably, polyethylene (PE), polypropylene (PP), polyvinylchloride (PVC), polystyrene (PS), and their copolymers are used as commodity plastics and constitute already more than 50 % of total thermoplastic materials consumption [1]. For extrusion-based additive manufacturing materials, polylactic acid (PLA) and acrylonitrile-butadiene-styrene (ABS) are the most widely used feedstock materials [9,10]. However, typical commodity plastics have not been favored for extrusion-based AM up to now. Since the applied material hardens after passing the hot nozzle upon cooling due to re-solidification, 3D printed materials should feature less shrinkage to offer high part dimensional accuracy and less fabrication failure. Here, typical semi-crystalline commodity thermoplastics show relatively high volumetric shrinkage and warp deformation of extrusion-based 3D printed parts due to the material-related degree of crystallization. Wang et al. have studied the warp deformation of FFF printed parts and their research indicates that the shrinkage-induced warpage depends on the nature and properties of the utilized materials, especially with regard to shrinkage coefficient and stiffness [7]. In addition, the layer-by-layer and direct material deposition of the FFF process forms laminations of fused layers, which causes the anisotropic property of the final 3D printed parts [5,11]. Hence, a typical final FFF printed part consists of a series of extruded and fused material strands and enclosed air voids. The resulting meso-structure interface bonding quality is dominated by the thermal history of each extruded strand, which in turn depends on the processing conditions and nature of the applied material [12,13]. Thus, the interface of fused strands is always the critical area of extrusion-based 3D printed parts caused by limited polymer chain intermixing and reduced formation of entanglements or crystals at the interface within the short time period of the melted state. Here, semi-crystalline materials with a low degree of crystallization could gain reinforcement due to their thermally reversible crosslinks caused by crystals at the interface. Therefore, in some extrusion-based 3D processes, nylon 12 is selected because it exhibits less warpage thanks to its relatively low crystallinity compared with Nylon 6 and outstanding mechanical properties compared with typical commodity plastics [14,15].

Among the commodity thermoplastics, polypropylene (PP) is the most common semi-crystalline thermoplastic applied in consumer and technical products due to its exceptional mechanical properties, processing ability, and low cost. In addition, through copolymerization as well as by compounding with additives and fillers, PP can be successfully modified and tailored for various applications [16,17]. Furthermore, amorphous PP (aPP) or amorphous polyolefins can be blended in a wide range with isotactic PP as a softening agent or to tailor the properties of a blend [18,19]. With a similar principle, PP copolymers or blends with polyethylene (PE) are also widely used to improve the performance of PP [20,21]. Additives such as clarification and nucleation agents are very popular in the industry to improve the optical and mechanical properties of PP. Among the different known modifications of polypropylene in the crystalline form, the monoclinic α and the hexagonal β modifications draw the most attention in both scientific research and industrial applications [22–24]. The α form is the most common modification under regular crystallization conditions, while the β crystal form is observed in the presence of β -nucleating agents [22] or after applying a special cooling and processing condition [25]. Compared to the α -phase, the β -phase is tougher but less dense and stiff [26]. For FFF materials, lower stiffness and density of formed crystals could reduce the inner stress caused by material shrinkage upon cooling [7] and thus may lead to enhance the 3D printing performance [7,22,23,25,27,28]. Some studies have reported preliminary results of incidentally observed β -PP crystals obtained in extrusion-based 3D printed parts by adding fillers or due to special thermal conditions during the printing process [29–31]. However, a systematic study of the influence of β -form crystals on shrinkage and bonding quality has yet to be reported. Among modified PPs, grades of polypropylene-ethylene

random copolymers (raco PP) offer a lower degree of crystallization due to the ethylene co-units, making these PP grades very promising for extrusion-based 3D printing [32–34].

In recent years, several research studies have focused on extrusion-based 3D printing utilizing PP. Carneiro et al. were the first to investigate a glass-fiber-filled polypropylene by modifying an injection molding grade of isotactic PP (iPP), and parts printed from it showed high shrinkage and warp deformation [35]. Wang et al. studied the crystallization kinetics of iPP by adding spray-dried cellulose nanofibrils (SDCNF) targeting retarding the crystallization and lowering the crystallinity. However, even after adding different amounts of SDCNF, the achieved reduction of crystallization rate and crystallinity indicates that the decrease of material shrinkage is expected to be relative low for iPP with high crystallinity [36]. We developed an effective screening method for optimizing polypropylene feedstock materials utilizing injection molded short rods and 3D printed square tube specimens [34]. Among the investigated iPP, raco PP, and PP/PE blends, the geometric deformation was reduced with decreasing crystallinity, indicating that raco PP, with its lower degree of crystallization, causes less warp deformation. Spoerk et al. selected a raco PP grade with a lower degree of crystallization as the base PP material for many of their studies [21,29,37–40]. In addition, Spoerk et al. optimized the shrinkage of raco PP by adding expanded spherical perlite fillers and also one amorphous polyolefin to reduce the brittle filament issue. However, although they managed to decrease part shrinkage, negative effects due to the high filler content, such as reduced maximum tensile strength and elongation of modified raco PP filaments, were also observed [21,29,38]. Interestingly, by adding aPP, the degree of crystallization of raco PP could be somewhat adjusted, which seems to be a promising way to decrease the geometric deformation [7,18,21]. However, for all reported studies, investigations on the influence of additives or on the content of polymer compounds within investigated blends with respect to the interlayer bonding quality are still missing for PP.

Inspired by the published results, the scope of this work is a detailed investigation into polypropylene/ethylene random copolymers which aims to improve extrusion-based 3D printed part performance. Here, the investigated raco PP filament modifications focused on reducing warp deformation and improving interlayer bonding quality. To achieve this, a β -nucleating agent or selected amorphous PP materials (aPP) were blended together with raco PP grades in different proportions in order to tune the crystallization behavior and interlayer bonding quality. The influence of these additives was systematically investigated utilizing injection molded short rods fed into a standard 3D printer. Single-wall square tubes were chosen as an optimized geometric form and 3D printed, allowing an efficient investigation into the degree of warp deformation and quality of interlayer bonding [34].

2. Experimental work

2.1. Materials

In this work, two commercial grade polypropylene/ethylene random copolymers serve as neat base PP materials for optimizations: raco PP RD208CF from Borealis, Austria denoted *raco PP 1* [41] and raco PP RP220 M from LyondellBasell, Netherlands denoted *raco PP 2* [42]. Six different amorphous polypropylene-based polyolefins were selected for blending and optimization: amorphous PP from Sigma-Aldrich, USA denoted *aPP 1* [43]; Rextac RT 2115 from Rectax, USA denoted *aPP 2* [44]; Vestoplast EP V2013 from Evonik, Germany denoted *aPP 3* [45]; Vestoplast 608 from Evonik, Germany denoted *aPP 4* [45]; Vestoplast 891 from Evonik, Germany denoted *aPP 5* [45]; Aer-afin 17 from Eastman, USA (denoted *aPP 6* [46]). One linear low density polyethylene (LLDPE) LL6101 from Exxonmobile denoted as *LLDPE* (Vicat softening point: 94 °C [47]) was also selected for blending. An overview of the technical data and of more detailed results of the polypropylene/ethylene random copolymers, amorphous

Table 1a
Basic technical data of investigated propylene/ethylene copolymers (raco PP).

Polyolefin	Supplier	Grade	Color	MFI (g/min) ^a	Flexural modulus (MPa)
raco PP 1	Borealis	RD208CF [41]	natural	8	650
raco PP 2	LyondellBassel	RP220 M [42]	natural	8	700

^a melt flow rate (230 °C/2.16 kg).

polypropylene and linear low density polypropylene is given in Table 1a, 1b, 1c and Supplementary material (S3). Thermal characterization by DSC of raco PP 1 and raco PP 2 is shown in the Supplementary material (S1).

The investigated β -nucleating agent was N,N'-dicyclohexyl-terephthalamide [54,55], CAS-Nr: 15088-29-6, synthesized at the chair of Macromolecular Chemistry I, University of Bayreuth, Germany.

2.2. Lab-scale feedstock rod preparation

Investigated materials (see Table 2) were compounded and injection molded into filament rods instead of utilizing conventional continuous feedstock filaments [34].

Corresponding PP fine powder was dry-blended with the β -nucleating agent in a glass bottle for 24 h utilizing rotating mixing equipment. For amorphous PPs, which were supplied as pellets or resin balls, the powder blending was not possible. The mixed raw materials were compounded afterwards under nitrogen atmosphere in a co-rotating twin-screw micro-compounder (DSM Xplore, 15 ml) at 240 °C and 40 rpm for 5 min. The melt was injected into a Teflon tube in order to precisely control the final dimension of the molded rods. After removing the Teflon tubes by peeling, filament rods with lengths between 135 mm and 140 mm and weights of around 0.85 g were obtained. For more details see reference [34].

2.3. FFF printer, specimen design and processing conditions

The FFF 3D printer used is a desktop twin-nozzle (nozzle diameter 450 μ m) FFF printer (3NTR A4, Italia) whose filament supply tube was modified for feeding with filament rods. The 3D digital model was designed (Fusion 360, Autodesk) and additionally sliced by software (Slic3r). The printed specimen is a single-line-stacked square tube [34] and the built surface is 5.0 cm \times 5.0 cm with a side wall thickness of around 600–650 μ m. As 3D printing build surface "P-surface 141" from PPprint GmbH from Germany was used [51]. The processing conditions for 3D printing of each commercial filament or manufactured rod were optimized individually using "design of experiment method" previously developed [34]. We found that all commercial filaments showed optimized 3D printing performance at the nearly same conditions. Therefore, we used for comparison of the commercial filaments a fixed set of parameters, which is included in Table 3.

2.4. Warp deformation and mechanical properties characterization

The degree of warp deformation of the side walls of printed square

Table 1b
Basic technical data of used amorphous polypropylenes (aPP) and linear low density polyethylene (LLDPE).

Amorphous Polyolefin	Supplier	Grade	Color	Softening point (°C) ^a	Melt viscosity (cps) ^b
aPP 1	Sigma-Aldrich	9003-07-0 [43]	natural	150	–
aPP 2	Rectax	RT 2115 [44]	natural	152	1500
LLDPE	Exxonmobile	LL6101 [47]	natural	–	–

^a ring and ball softening point.

^b melt viscosity at 190 °C.

tubes was measured quantitatively and evaluated as reported elsewhere [34]. The measured geometric deformation of side walls is defined by the distance between the maximal deformation point of printed cubic tubes and the non-deformation contour of an ideal shaped cubic tube. To define the edges of ideal non-deformation contour, a rigid flat reference plate was attached on one side to the side wall. The distance between the deformation surface and reference plate was measured using a digital caliper. Each side was measured two times, therefore totally eight different positions on the side walls of each cubic tube were measured.

For mechanical testing, each square tube was cut into the four single side walls using a CO₂ laser cutter. In this work, tensile specimens with angles of 90° and 0° to the layer deposition direction were punched out (Coesfeld Materialtest Inc., electro-hydraulic punching cutter, mold knife for tensile specimen DIN 53 504 S3A) and used to evaluate interlayer bonding and bulk mechanical properties, respectively. Out of each side wall, five tensile specimens were punched out and used for the mechanical characterization. Tensile tests were performed according ISO 527 on an Instron® 5565 universal tester with pneumatic clamps and a 1 kN load cell. The thickness of the specimens was measured with a digital micrometer (Mitutoyo® 293–831, digimatic MDC Lite).

The E-modulus was investigated at a strain rate of 0.2 mm/min and calculated between 0.1 % and 0.3 % strain. After E-modulus determination, strain rates of 2.0 mm/min and 40.0 mm/min were applied for 90° and 0° specimens, respectively. The elsewhere reported [34] effective thickness correction was applied for the investigated single-line-stacked specimens (see also Supplementary material S2). The surface roughness was determined with a stylus profilometer (Veeco DEKTAK 150) in combination with WYKO Version software. To characterize the interlayer bonding properties the values of maximum strain are used, as these values reveal a clearer view on the anisotropic behavior compared with Young's modulus and strength values. Therefore, the term "strain bonding quality" is used in this work as the critical criterion for the layer fusion of 3D printed parts. In addition, a jumping frog test was performed to demonstrate the properties of a 3D printed thin wall geometries and the interlayer bonding quality. For more details, please see Supplementary material (S1, S2, and S4).

2.5. X-ray diffraction analysis (WAXS)

To investigate the β -form of PP printed specimens, wide-angle X-ray scattering (WAXS, Bruker D8 X-ray diffractometer) was utilized at a voltage of 40 kV and a current of 40 mA. By using nickel-filtered CuK α radiation (1.54 Å), the diffraction pattern was recorded with a step size of 0.05° between 2 θ from 8° to 30°. The amount of beta modification was determined utilizing the Turner-Jones method (eq. (1)) [48].

$$k = \frac{H_{\beta 1}}{H_{\beta 1} + (H_{\alpha 1} + H_{\alpha 2} + H_{\alpha 3})} \quad (1)$$

A characteristic scattering peak around 2 θ = 15.8° is widely used to calculate the β -content of polymorphous crystals in PP via k -value. $H_{\alpha 1}$, $H_{\alpha 2}$, and $H_{\alpha 3}$ are the corresponding peak heights of the three characteristic α -form peaks at 2 θ = 13.85°, 16.6°, and 18.2°, respectively. For the k -value, the value 0 corresponds to fully α -form crystals, while

Table 1c
Basic technical data of investigated commercial PP, PLA and ABS filaments.

Commercial filaments	Supplier	Filament	Color	Printing Tem. (°C) ^a	E-modulus (MPa)
PP 1	Reprap	PP filament [48]	black	200–245	1050 ^b
PP 2	Popbit	PP filament [49]	white	240–260	1200 ^b
PP 3	Ultimaker	Ultimaker PP [50]	natural	205–220	450 ^a
PP 4	Ppprint	P-filament 721 [51]	natural	200–220	650 ^a
ABS	Orbi-Tech	Smart ABS [52]	natural	240–250	1750 ^b
PLA	Orbi-Tech	PLA filament [53]	white	195–240	3500 ^b

^a values according data sheet from supplier.

^b values from tensile specimens obtained by the testing method in [34].

Table 2
Composition of the polymer blends comprising a β-nucleating agent or amorphous PP.

PP	Additive/aPPs	Concentration	Related chapter
raco PP 1	β-nucleating agent	100, 500, 1000 ppm	3.1
raco PP 1	aPP 1	1.0, 5.0, 10.0 wt%	3.2
raco PP 2	aPP 1	10.0, 15.0, 20.0 wt%	3.3
raco PP 2	aPP 2	10.0 wt%	3.4
raco PP 2	LLDPE	10.0 wt%	3.4
raco PP 2	aPP 3-6	10.0 wt%	Supplementary mat.

Table 3
Optimized processing conditions for 3D printing of different PP samples and filaments.

Parameter	Rods: raco PP 1/ modified raco PP 1	Rods: raco PP 2/ modified raco PP 2	Commercial PP filaments
Nozzle temperature (°C)	250	210	220/250
Print bed temperature (°C)	120	120	120
Printing speed (mm/s)	15	15	15
Layer height (μm)	250	250	250
Fan speed (%)	100	100	100

value 1 corresponds to fully β-form crystals.

2.6. Thermal analysis and degree of crystallization

Thermal properties and melt enthalpies of printed samples were investigated using differential scanning calorimetry (DSC) (Mettler Toledo DSC 2 STAR^e system). Samples were cut out of the middle area from corresponding square tube side walls. The DSC measurements

were performed under nitrogen atmosphere within the temperature range of 25 °C–230 °C at a heating/cooling rate of 10 K/min. The first heating curve was used for the melt enthalpy peak area integration (see also Supplementary material S1). Because of the broad crystallization range, the integration of each enthalpy peak area was determined from 60 °C to 160 °C with the STAR^e software. The average of five independent measurements were used to calculate corresponding degree of crystallizations. To determine the degree of crystallization of the β nucleated samples we used the k value as fraction ratio of the β to α phase and for the polymer blend systems the different crystalline fractions were taken into account using following equation:

$$X_c = \frac{\Delta H_m}{\Delta H_{m,0}*(1-x) + \Delta H'_{m,0}*x} \quad (2)$$

where ΔH_m is the measured melting enthalpy of printed samples. For the iPP α phase we used ΔH_{m,0} of 207 Jg⁻¹, which corresponds to the melting enthalpy of a 100 % crystalline α-iPP [56]. For the β phase we used ΔH'_{m,0} of 192 Jg⁻¹ corresponds to 100 % β-form iPP [17]. For the blend of raco PP with 10 wt% LLDPE we used for LLDPE ΔH'_{m,0} of 293 Jg⁻¹ of 100 % crystalline PE [57]. Here, x is either the k value or refers to the blend composition.

2.7. Crossed polarized light microscopy

Crossed polarized light microscopy was used to investigate the crystalline structure of PP with the focus on the interlayer bonding area. All experiments were performed using a crossed polarized light microscope from Nikon (DIAPHOT 300). Crossed polarized light micrographs were recorded by a Nikon ACT-1 software using a digital camera (Nikon, DMX1200). All pictures were taken at same conditions for all samples at different magnification of 10x and 40x at exposure time of 100 ms and 700 ms, respectively. Samples were cut out of the middle area of the printed square tubes. Here, thin slices with a thickness of about 10 μm were cut with a rotary microtome (RM2255 from Leica

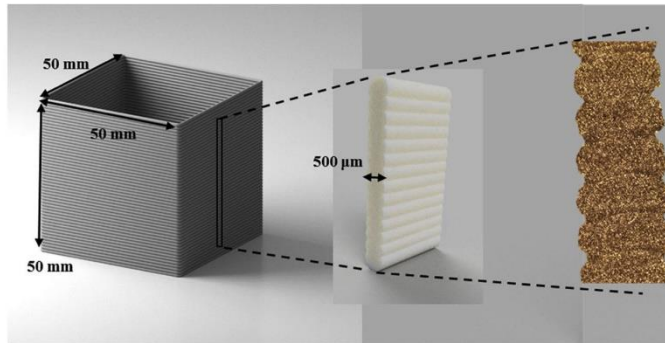


Fig. 1. Illustration of the sample preparation for crossed polarized light microscopic investigations. Samples were cut from the middle area of the printed square tubes. Thin slices with a thickness of about 10 μm were cut with a rotary microtome and placed between glass slides for photography.

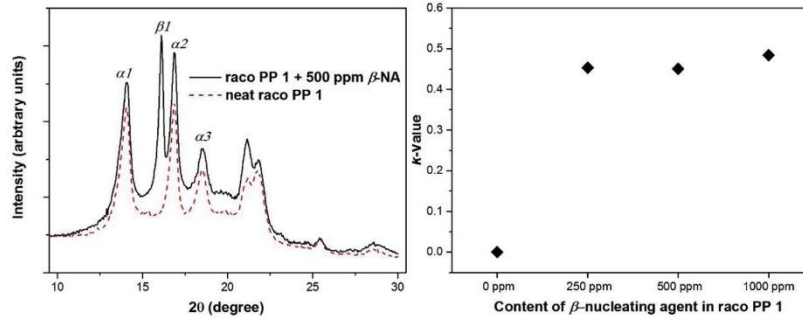


Fig. 2. WAXS patterns of 3D printed specimens utilizing (left) neat *raco PP 1* and *raco PP 1* with 500 ppm β -nucleating agent and (right) calculated k values of investigated *raco PP 1* specimens with different contents of β -nucleating agent.

Co.). The sample preparation is illustrated in Fig. 1.

3. Results and discussion

3.1. *Raco PP* modified with a β -nucleating agent

In order to reveal the influence of β -nucleating agents on the extrusion-based additive manufacturing of polypropylene, the *raco PP 1* was modified with different amounts of a β -nucleating agent (β -NA). *N,N'*-dicyclohexyl-terephthalamide was selected as β -NA [55,58]. WAXS patterns shown in Fig. 2 (left) are recorded from a printed square tube of *raco PP 1* with 500 ppm β -nucleating agent and from neat *raco PP 1* as reference (red dashed line). A significant $\beta 1$ peak indicates the presence of the β crystal structure. In contrast, the neat *raco PP 1* pattern exhibits no $\beta 1$ peak and hence is a *raco PP* with a fully α -modification with a k -value of 0 [24]. All investigated and calculated k -values as a function of concentration are summarized in Fig. 2 (right). Independent of the amount of β -nucleating agent added, all k -values are nearly constant at around 0.45. This observation is in agreement with the literature and the fact that the growth of β -form crystals progresses only in the temperature range of 100 °C–140 °C [54,55,59]. Below 100 °C or above 140 °C, the β - α growth transition occurs and thus the growth rate of the α -phase is favored. Due to the layer-by-layer construction principle of FFF, the extruded material is reheated several times by subsequently deposited layers on top [8]. Thus for simple thin-wall tube geometry, the material is reheated relatively efficiently, which could promote β - α growth transition and result in very similar k -values independent of the content of β -nucleating agent.

Recorded crossed polarized light microscopic images show clear differences (see Fig. 3). In contrast to the neat *raco PP 1* the β -nucleated sample shows darker stripes at the interlayer areas between two printed strands with a height of about 50 μ m. Further the spherulites within the entire β -nucleated sample are smaller compared to the not nucleated PP.

Fig. 4 (left) shows the measured geometric deformation of printed square tube samples. Details about the measurement and the evaluation are presented in Supplementary material S2. An unexpected rise after adding the β -nucleating agent is observed. A possible explanation of this increased warp deformation might be the β - α crystal growth transition and the resulting complex β - α twin structure which forms different crystal boundaries [27]. Thus, the inner stress cannot be eliminated or homogeneously distributed and thus causes higher geometric warp deformation. In addition, Fig. 4 (right) suggests that the used β -nucleating agent has no obvious influence on the stiffness of printed samples, as the E-moduli remain quite constant. Additionally, the samples containing the β -nucleating agent show similar degree of crystallization, which indicates that NA does not change the degree of crystallization.

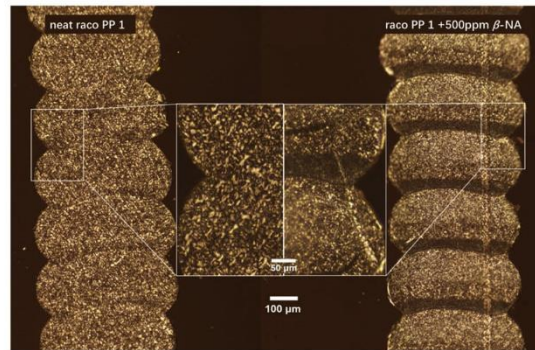


Fig. 3. Crossed polarized light microscopic images (10x and 40x) from cross section of square tube of neat *raco PP 1* (left) and *raco PP 1* with 500 ppm β -nucleating agent (right).

Furthermore, the strain bonding quality at the interface of two fused strands was efficiently investigated by tensile tests on 90° dog bone specimens (see also Chapter 2.4). The tensile test curves in Fig. 5 (left) demonstrate that a high concentration of the β -nucleating agent has a negative influence on the interlayer strain bonding quality. The β -nucleating agent modifies the crystal form at a certain content and thus seems to influence the polymer chain diffusion and crystallization behavior at the interfaces of fused strands. Adding 500 or 1000 ppm of β -nucleating agent obviously impairs the strain bonding quality, while adding 250 ppm slightly improves the observed tensile strain. This phenomenon also probably originates from the β - α crystallite growth transition and the occurrence of twin crystal structures, which possess many boundaries. All 0° specimens demonstrate very similar mechanical properties, which means the β -nucleating agent did not relevantly influence strength and E-modulus of the bulk material (Fig. 5 (left)). The mechanical properties of the 0° specimens correspond to those of the bulk material, which is fabricated by a conventional injection molding process. Because the strands in these specimens are oriented parallel to the tensile loading direction, the obtained stress-strain curves show typical behaviors of thermoplastics with a hardening effect and a tensile strain of about 1500 %. In contrast, 90° specimens show less strength and clearly less strain behaviors (Fig. 5 (right)). The fracture surface of a photographed broken dog bone of a 90° specimen, processed from *raco PP 1* with 500 ppm β -nucleating agent, is smooth and indicates poor interlayer bonding.

From Table 4, anisotropic properties of the investigated specimens are clearly observable by comparing the tensile strain values of 0° and 90° specimens. The tensile strain values (denoted as elongation at break) of 90° specimens are only about 2 % of those of 0° specimens due

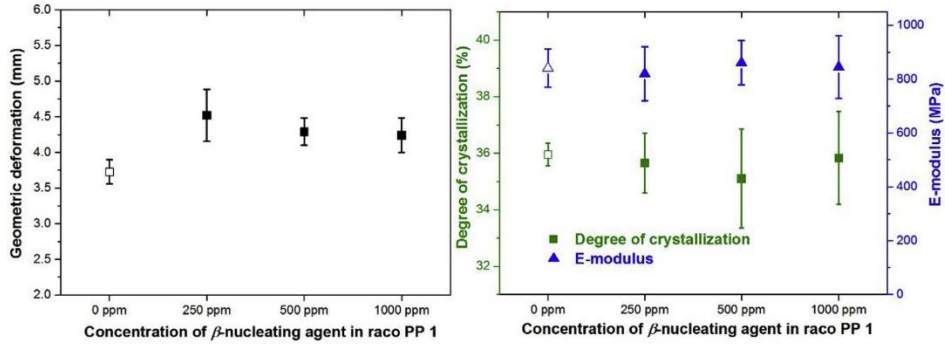


Fig. 4. The influence of β -nucleating agent concentration on (left) geometric deformation (black hollow square: neat raco PP 1 samples, black solid squares: β -nucleating agent modified raco PP 1 samples) and (right) degree of crystallization and E-moduli (90° orientation) of printed square tube specimens (degree of crystallization: green hollow square: neat raco PP 1 samples, green solid square: β -nucleating agent modified raco PP 1 samples; E-moduli: blue hollow triangle: neat raco PP 1 samples, blue solid triangles: β -nucleating agent modified raco PP 1 samples). (For interpretation of the references to colour in this figure legend, the reader is referred to the web version of this article).

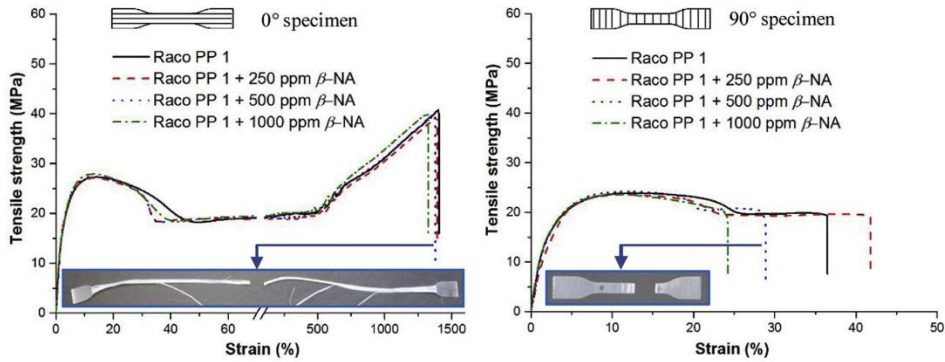


Fig. 5. Stress-strain curves of 0° specimens (left) and (right) 90° specimens (racó PP 1: black solid line, racó PP 1 with 250 ppm β -nucleating agent: red dashed line, racó PP 1 with 500 ppm β -nucleating agent: blue dotted line, racó PP 1 with 1000 ppm β -nucleating agent: green dash-dotted line). Images of broken 0° and 90° dog bones (from racó PP 1 with 500 ppm β -nucleating agent) are shown at the bottom of the graphs. All shown stress-strain curves are a representative example of an actual measurement out of at least 10 specimens. (For interpretation of the references to colour in this figure legend, the reader is referred to the web version of this article).

Table 4
Mechanical properties of 0° and 90° oriented dog bones of β -nucleating agent modified racó PP 1 punched out of FFF printed square tubes.

Material	Orientation ^a	E [MPa] ^b	σ_{yt} [MPa] ^c	σ_{br} [MPa] ^d	ϵ_{br} [%] ^e
racó PP 1 neat	0°	841 (71) ^f	27.3 (0.4)	40.7 (1.3)	1400 (20)
	90°	828 (21)	23.9 (0.2)	20.0 (0.2)	35.9 (5.1)
racó PP 1 with 250 ppm β -NA ^g	0°	820 (100)	27.2 (0.4)	38.5 (2.9)	1422 (39)
	90°	819 (50)	23.6 (0.3)	19.4 (0.5)	39.0 (9.1)
racó PP 1 with 500 ppm β -NA	0°	861 (82)	27.6 (0.4)	39.3 (1.7)	1397 (72)
	90°	866 (33)	24.0 (0.2)	19.7 (0.6)	31.0 (4.0)
racó PP 1 with 1000 ppm β -NA	0°	845(116)	27.9 (0.4)	41.5 (1.2)	1312 (46)
	90°	840 (55)	23.5 (0.3)	19.7 (0.5)	24.4 (5.4)

^a Orientation of tensile loading direction to layer deposition direction.
^b E-modulus.
^c strength at yield.
^d strength at break.
^e elongation at break.
^f standard deviation in parentheses.
^g β -NA = β -nucleating agent N,N'-dicyclohexyl-terephthalamide.

to the reduced interlayer strain bonding quality. Maximum tensile strengths of 90° specimens are obtained at about 60 % of 0° specimens and yield strengths at about 90 %. The E-moduli from both 0° and 90° specimens are very similar due to the initial tensile loading range (measured at a strain between 0.1-0.3 %), which is far away from stressing the interlayer bonding of 90° specimens.

3.2. Racó PP 1 blended with aPP 1

To tune the crystallinity, stiffness and interlayer bonding quality of FFF printed parts, racó PP 1 was blended with the amorphous polypropylene aPP 1 and manufactured into feedstock polymer rods. Fig. 6 shows that the geometric deformation, degree of crystallization, and E-modulus of obtained square tubes decrease with increasing amount of blended amorphous PP. The geometric deformation is reduced from 3.7 to 3.2 mm by adding 10 wt% of aPP 1. The degree of crystallization is reduced mainly due to dilution. A reduction of the degree of crystallization from 36 % to 35 % is observed already by addition of 1 wt% aPP 1. Adding 10 wt% aPP 1 lowers the degree of crystallization further to 33 %. The E-modulus is also reduced because of adding the soft aPP 1. With the addition of 10 wt% aPP 1, a drop in the E-modulus from 830 to 660 MPa is measured for samples with 90° orientation.

Fig. 7 compares crossed polarized light microscopic images of neat

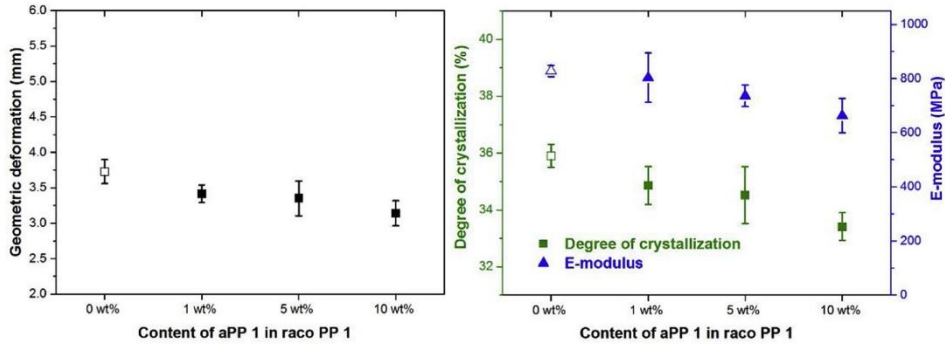


Fig. 6. Influence of aPP 1 content in raco PP 1 on (left) geometric deformation (black hollow square: neat raco PP 1 samples, black solid squares: raco PP 1 blended with aPP 1) and (right) degree of crystallization and E-moduli (90° orientation) of printed square tube specimens (green hollow square: neat raco PP 1 samples, green solid squares: raco PP 1 blended with aPP 1, blue hollow triangles: neat raco PP 1 sample, blue solid triangles: raco PP 1 blended with aPP 1). (For interpretation of the references to colour in this figure legend, the reader is referred to the web version of this article).

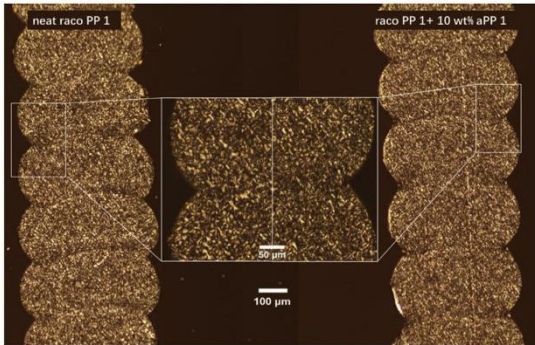


Fig. 7. Crossed polarized light microscopic images (10x and 40x) from cross section of square tube of neat raco PP 1 (left) and raco PP 1 with 10 wt% aPP 1 (right).

raco PP 1 and 10 wt% aPP 1 samples. No significant differences are visible although the interlayer strain bonding quality results in a higher strain bonding strength. The interface boundary lines appear a little clearer for the neat PP 1 sample and slightly more blurry for the blend with 10 wt% aPP 1. The overall morphology is in both cases uniform.

Table 5

Mechanical properties of 0° and 90° oriented dog bones of neat raco PP 1 and raco PP 1 blended with aPP 1 and punched out of FFF printed square tubes.

Material	Orientation ^a	E [MPa] ^b	σ_{y1} [MPa] ^c	σ_{br} [MPa] ^d	ϵ_{br} [%] ^e
raco PP 1 neat	0°	841 (71) ^f	27.3 (0.4)	40.7 (1.3)	1400 (20)
	90°	828 (21)	23.9 (0.2)	20.0 (0.2)	35.9 (5.1)
raco PP 1 with 1 wt% aPP1	0°	847 (30)	25.8 (0.4)	41.3 (1.5)	1475(83)
	90°	803 (91)	23.2(0.2)	19.9 (0.3)	39.3 (12)
raco PP 1 with 5 wt% aPP1	0°	764 (87)	25.6 (0.3)	39.1(1.0)	1400 (51)
	90°	736 (40)	21.6 (0.5)	18.1 (0.8)	211 (23)
raco PP 1 with 10 wt% aPP1	0°	680 (16)	22.1 (0.4)	36.7 (1.6)	1535 (28)
	90°	663 (64)	19.4 (0.3)	16.2 (0.5)	283 (95)

- ^a Orientation of tensile loading direction to layer deposition direction.
- ^b E-modulus.
- ^c strength at yield.
- ^d strength at break.
- ^e elongation at break.
- ^f standard deviation in parentheses.

The mechanical properties of blended samples are shown in Fig. 8 and summarized in Table 5. In Fig. 8, stress-strain curves of 0° specimens are plotted in the left. These specimens show lower stiffness and strength with increasing content of aPP 1. The soft amorphous polyolefin aPP 1 seems to act as a plasticizer, thus the blended samples are softer and more elastic and the high strains are still slightly enhanced.

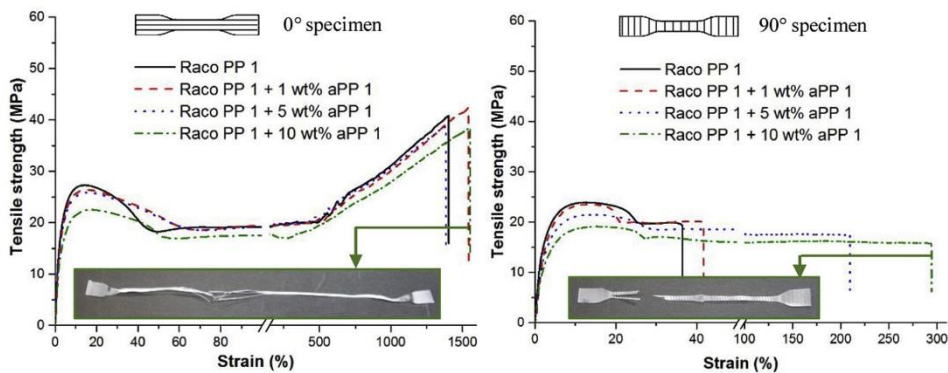


Fig. 8. Stress-strain curves of (left) 0° specimens and (right) 90° specimens (raco PP 1: black solid line, raco PP 1 with 1 wt% aPP 1: red dashed line, raco PP 1 with 5 wt% aPP 1: blue dotted line, raco PP 1 with 10 wt% aPP 1: green dash-dotted line). Images of broken 0° and 90° dog bones (from raco PP 1 with 10 wt% aPP 1) are shown at the bottom of the graphs. All shown stress-strain curves are a representative example of an actual measurement out of at least 10 specimens. (For interpretation of the references to colour in this figure legend, the reader is referred to the web version of this article).

Despite lower stiffness and strength at higher amounts of *aPP 1*, the interlayer bonding qualities are stepwise improved for 90° specimens (Fig. 8 (right)). The volume filling effect of *aPP 1* among crystal spherulite boundaries seems to strengthen the physical crosslinks produced by crystallites at the interface [18]. 90° specimens blended with 10 wt% *aPP 1* achieve almost 300 % elongation at break, which is about eight times higher than the strain of neat *raco PP 1*.

In Table 5, the results of tensile tests are summarized in detail. By blending with *aPP 1*, the interlayer strain bonding quality is clearly improved; exemplarily, the strain of the 90° specimen is improved by about 500 % for the specimen with 10 wt% of *aPP 1*. Compared with neat *raco PP 1*, the specimen blended with 10 wt% *aPP 1* shows a drop in E-modulus and yield strength of about 20 % for both 90° and 0° specimens.

3.3. *Raco PP 2* blended with *aPP1*

A second *raco PP* with a higher E-modulus, *raco PP 2* from LayonellBasell, was also used. Furthermore, higher concentrations of blended *aPP 1* were investigated in the range of 10 wt% to 20 wt%. Compared with *raco PP 1*, the *raco PP 2* features similar flow properties but with a more favorable low degree of crystallization and the already mentioned higher E-modulus. Consequently, *raco PP 2* should provide an enhanced potential to further lower the degree of crystallization while maintaining a higher E-modulus. From Fig. 9 (left), the obtained geometric deformation of investigated blends of *raco PP 2* is unfavorably higher than for blends of *raco PP 1* and *aPP 1* (see Fig. 6). However, it is lowered by adding higher contents of *aPP 1*. An explanation for this unexpectedly high geometric deformation may be the higher E-modulus and higher stiffness of commercial grade *raco PP 2*. In addition, incorporated additives, such as nucleating agents, used in *raco PP 2* could also influence the geometric deformation. Degree of crystallization and E-moduli are clearly lowered by adding higher contents of *aPP 1*. Although at 15 wt%, the degree of crystallization and E-modulus are not significantly lower than at 10 wt% of *aPP 1*, the addition of 20 wt% of *aPP 1* further reduces the E-modulus but less the degree of crystallization. From crossed polarized light microscopic images, there are no significant differences in comparison of neat *raco PP 2* to blended samples with *aPP 1* (not shown here).

In Fig. 10, the mechanical properties of *raco PP 2* blended with *aPP 1* are shown. The 0° specimens show very similar tensile strains but a clearly observable decrease in yield strength and E-modulus at higher *aPP 1* concentrations. For 90° specimens, all blended samples show tensile strains of over 600 % and the highest value is observed for the specimen with 10 wt% of *aPP 1*. This observation demonstrates that no further improvement of the interlayer bonding is achieved by adding

more than 10 wt%, while E-modulus and yield strength drop further at higher *aPP 1* concentrations.

In Table 6, the mechanical properties of 0° and 90° specimens of neat *raco PP 2* and *raco PP 2* blended with *aPP 1* are given in detail. Comparing the 10 wt% with the 20 wt% 90° specimens, the E-modulus is clearly reduced by about 30 % and the tensile strain by about 20 %. Consequently, more than 10 wt% of *aPP 1* brings no further improvement in critical performance parameters such as interlayer strain bonding quality, E-modulus, and strength of FFF printed parts, and demonstrates the optimized *aPP 1* content of 10 wt% with respect to the balance between geometric deformation and mechanical properties.

3.4. *Raco PP 2* blended with different *aPPs* and one *LLDPE*

To investigate the influence of different types of amorphous polyolefins, the identified optimized 10 wt% content was used for the preparation of additional blends of *raco PP 2* with further selected *aPPs* (*aPP 2* to *aPP 6*), as well as one *LLDPE*. Fig. 11 shows the measured geometric deformations (Fig. 11 (left)) and degree of crystallization and E-moduli (Fig. 11 (right)) of neat *raco PP 2* and *raco PP 2* blends with 10 wt% of *aPP 1*, *aPP 2*, or *LLDPE* (more *aPP* results see Supplementary material S4). While blended specimens of *aPP 1* and *aPP 2* demonstrate significantly reduced geometric deformation compared to the neat *raco PP 2*, an increase in shrinkage is observed for specimens blended with *LLDPE*. This finding is supported by the measured degree of crystallization shown in Fig. 11 (right), with the *LLDPE* blend showing the highest degree of crystallization of the investigated blends. The degree of crystallization is clearly decreased by blending *raco PP 2* with *aPP1* or *aPP 2*. With lower crystallinity, the two *aPP* blended samples demonstrate lower E-moduli; the *LLDPE* blended sample also shows an E-modulus decrease but less significant.

Crossed polarized light microscopic images (Fig. 12) compare the neat *raco PP 2* and the blend with 10 wt% *LLDPE*. Significantly brighter boundary areas at the interface area of fused strands are visible in the blend. In addition, spherulites of *raco PP 2* with 10 wt% *LLDPE* appear smaller compared to the neat *raco PP 2* crystals. As the strain bonding quality of the blend is significantly reduced by the blended *LLDPE* a morphology change in the interface area is indicated.

In Fig. 13 (left), investigated 0° specimens show very similar tensile strains. The sample blended with *LLDPE* with the lowest tensile strain with about 1250 % due to the PP/PE phase separation but a higher E-modulus and strength at yield compared with *aPP* blended samples. Neat *raco PP 2* demonstrates the highest E-modulus, strength at yield, and strength at break. In Fig. 13 (right), more effective screening and evaluation of corresponding interlayer bonding properties of 3D printed parts can be realized since 90° specimens are investigated. Crystal

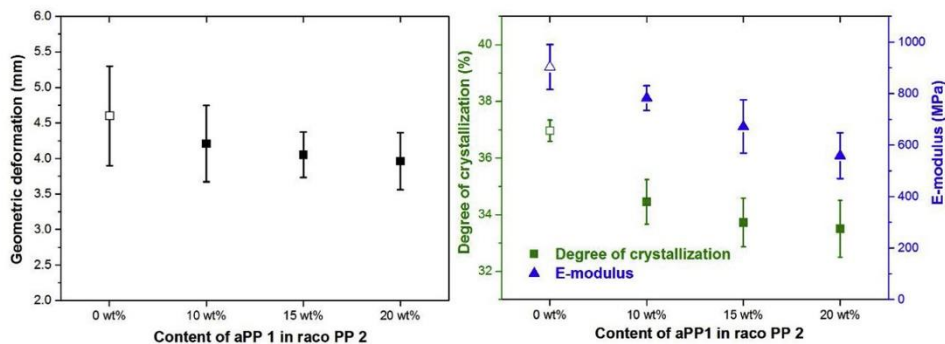


Fig. 9. Influence of *aPP 1* content in *raco PP 2* on (left) geometric deformation (black hollow square: neat *raco PP 2* samples, black solid square: *raco PP 2* blended with *aPP 1*) and (right) degree of crystallization and E-moduli (90° orientation) of printed square tube specimens (green hollow square: neat *raco PP 2* samples, green solid square: *raco PP 2* blended with *aPP 1*, blue hollow triangle: neat *raco PP 2* samples, blue solid triangle: *raco PP 2* blended with *aPP 1*). (For interpretation of the references to colour in this figure legend, the reader is referred to the web version of this article).

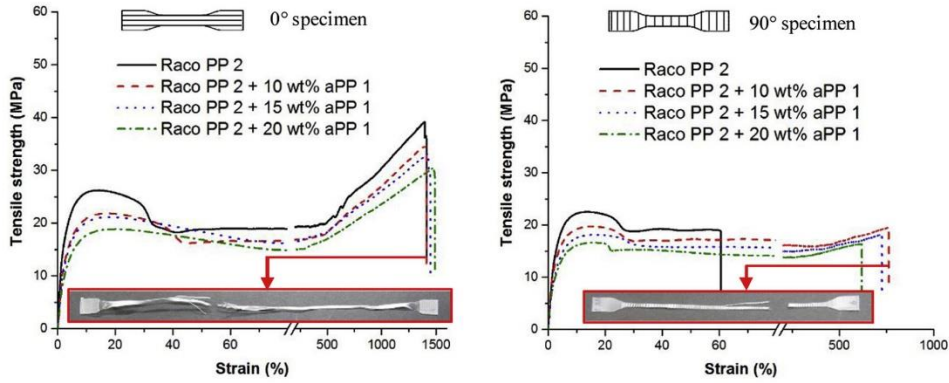


Fig. 10. Stress-strain curves of (left) 0° specimens and (right) 90° specimens of neat *raco PP 2* and *raco PP 2* blended with *aPP 1* (neat *raco PP 2*: black solid line, *raco PP 2* with 10 wt% *aPP 1*: red dashed line, *raco PP 2* with 15 wt% *aPP 1*: blue dotted line, *raco PP 2* with 20 wt% *aPP 1*: green dash-dotted line). Images of broken 0° and 90° dog bones (from *raco PP 1* with 10 wt% of *aPP 1*) are shown at the bottom of the graphs. All shown stress-strain curves are a representative example of an actual measurement out of at least 10 specimens. (For interpretation of the references to colour in this figure legend, the reader is referred to the web version of this article).

Table 6

Mechanical properties of 0° and 90° oriented dog bones of neat *raco PP 2* and *raco PP 2* blended with *aPP 1* punched out of FFF printed square tubes.

Material	Orientation ^a	E [MPa] ^b	σ_{yt} [MPa] ^c	σ_{br} [MPa] ^d	ϵ_{br} [%] ^e
<i>raco PP 2 neat</i>	0°	971 (19) ^f	25.4 (0.6)	39.7 (0.8)	1429 (31)
	90°	903 (87)	22.1 (0.7)	18.5 (0.5)	57.0 (20)
<i>raco PP 2 with 10 wt% aPP1</i>	0°	769 (12)	21.2 (0.4)	35.0 (1.1)	1467 (44)
	90°	783 (48)	19.4 (0.4)	19.4 (0.4)	664 (135)
<i>raco PP 2 with 15 wt% aPP1</i>	0°	704 (24)	20.3 (0.5)	32.1 (0.9)	1412 (70)
	90°	672 (103)	18.1 (0.3)	18.1 (0.3)	739 (29)
<i>raco PP 2 with 20 wt% aPP1</i>	0°	616 (52)	19.3 (0.3)	31.0 (1.1)	1428 (42)
	90°	559 (89)	16.9 (0.2)	16.9 (0.2)	525 (69)

- ^a Orientation of tensile loading direction to layer deposition direction.
- ^b E-modulus.
- ^c strength at yield.
- ^d strength at break.
- ^e elongation at break.
- ^f standard deviation in parentheses.

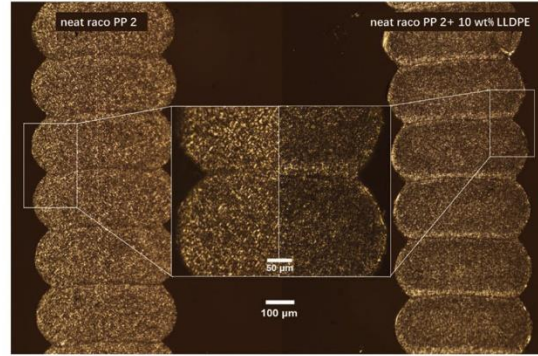


Fig. 12. Crossed polarized light microscopic images (10x and 40x) from square tube of neat *raco PP 2* (left) and *raco PP 2* with 10 wt% LLDPE (right).

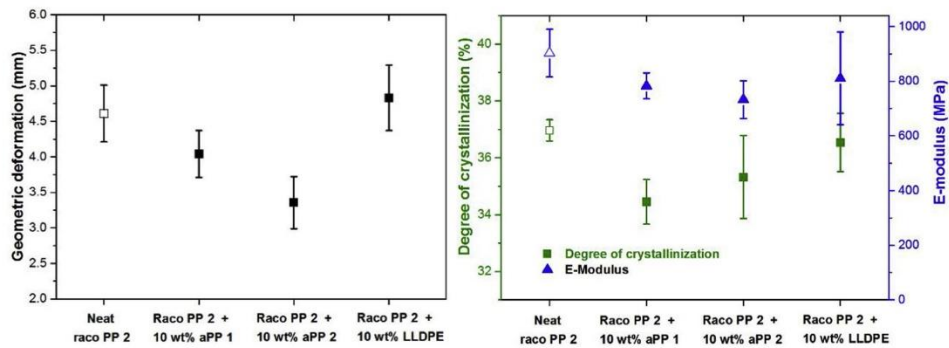


Fig. 11. Influence of *aPP 1*, *aPP 2*, or LLDPE blended with *raco PP 2* (left) on geometric deformation (black hollow square: neat *raco PP 2* sample, black solid square: *raco PP 2* blended with *aPP 1*, *aPP 2*, or LLDPE) and (right) degree of crystallization and E-moduli (90° orientation) of printed square tube samples (green hollow square: neat *raco PP 2* sample, green solid triangle: *raco PP 2* blended with *aPP 1*, *aPP 2*, or LLDPE, blue hollow triangle: neat *raco PP 2* samples, blue solid triangles: *raco PP 2* blended with *aPP 1*, *aPP 2*, or LLDPE). (For interpretation of the references to colour in this figure legend, the reader is referred to the web version of this article).

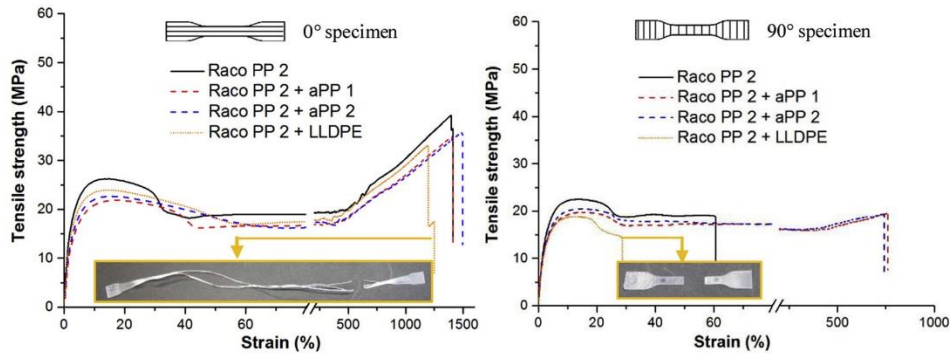


Fig. 13. Stress-strain curves of (left) 0° specimens and (right) 90° specimens (neat *raco PP 2*: black solid line, *raco PP 2* with 10 wt% *aPP 1*: red dashed line, *raco PP 2* with 10 wt% *aPP 2*: blue dashed line, *raco PP 2* with 10 wt% *LLDPE*: orange dashed line). Images of broken 0° and 90° dog bones (from *raco PP 2* with 10 wt% *LLDPE*) are shown at the bottom of the graphs. All shown stress-strain curves are a representative example of an actual measurement out of at least 10 specimens. (For interpretation of the references to colour in this figure legend, the reader is referred to the web version of this article).

spherulite blends with aPPs allow boundaries to be filled [18] and thus their 90° specimens feature higher interlayer bonding qualities, but the tensile strain values are more scattered compared to those of the 0° specimens. Especially the 90° specimen blended with 10 wt% of *LLDPE* shows significant mechanical property loss compared to its 0° specimen and even more compared to the blends of *raco PP 2* and two aPPs. This observation may result again from a phase separation and thus a different crystallization behavior of formed *LLDPE* and *raco PP 2* domains (see also Fig. 12). The melted state responsible for the formation of interlayer bonding of an FFF processed part occurs for only a very short time period. In this case, the coexistence of separated PP and PE crystallites within the interface could impair the interlayer strain bonding quality due to hetero crystallite boundaries. Furthermore, both 90° specimens of blends of *raco PP 2* and *aPP 1* and *2* (Fig. 13 (right)) show clear improvement in interlayer strain bonding quality compared with neat *raco PP 2*.

From Figs. 11 and 13, and Table 7 the lowest geometric deformation is given by the 10 wt% *aPP 2* blended specimen, offering still high mechanical properties and outstanding interlayer strain bonding quality. The E-modulus is around 740 MPa and tensile yield strength at the highest level among all investigated specimens.

Table 7

Mechanical properties of 0° and 90° oriented dog bones of neat *raco PP 2* and *raco PP 2* blended with *aPP 1*, *aPP 2*, or *LLDPE* punched out of FFF printed square tubes.

Material	Orientation ^a	E [MPa] ^b	σ_{yt} [MPa] ^c	σ_{br} [MPa] ^d	ϵ_{br} [%] ^e
<i>raco PP 2</i> neat	0°	971 (19) ^f	25.4 (0.6)	39.7 (0.8)	1429 (31)
	90°	903 (87)	22.1 (0.7)	18.5 (0.5)	57.0 (20)
<i>raco PP 2</i> with 10 wt% <i>aPP 1</i>	0°	769 (12)	21.2 (0.4)	35.0 (1.1)	1467 (44)
	90°	783 (48)	19.4 (0.4)	19.4 (0.4)	664 (135)
<i>raco PP 2</i> with 10 wt% <i>aPP 2</i>	0°	744 (46)	22.7 (0.5)	35.9 (0.5)	1484 (13)
	90°	733 (69)	20.4 (0.2)	20.4 (0.2)	690 (152)
<i>raco PP 2</i> with 10 wt% <i>LLDPE</i>	0°	859 (90)	23.8 (0.7)	36.4 (1.2)	1353 (93)
	90°	811 (170)	19.2 (0.4)	15.2 (0.2)	26.0 (7.9)

^a Orientation of tensile loading direction to layer deposition direction.
^b E-modulus.
^c strength at yield.
^d strength at break.
^e elongation at break.
^f standard deviation in parentheses.

3.5. Performance of 3D printed parts of selected PP-based feedstock materials

In order to contrast the performance of 3D printed parts of the investigated two *raco PP* grades and their optimized blends with aPPs, we selected neat *raco PP 1* and *2*, the blends of *raco PP 1* and 10 wt% of *aPP 1*, and *raco PP 2* and 10 wt% of *aPP 2*. For reference purposes we selected four commercially available PP filaments (see Chapter 2.1) denoted here as *PP 1-4*. From Fig. 14 (left), the measured geometric deformation demonstrates that the values could be clearly reduced by blending the investigated *raco PP* grades with 10 wt% of an aPP (visualized by arrows in Fig. 14), and optimized values are at a very similar level to those of the commercially available filaments *PP 2* and *3*. While the commercial *PP 1* shows higher geometric deformation, the commercial *PP 4* demonstrates the best value for this property among all the PP specimens. From Fig. 14 (right), the degree of crystallization is slightly higher for blending *raco PP 1* with *aPP 1* compared with *raco PP 2* blended with *aPP 2*, while the E-modulus decrease trend is reversed. The E-moduli of modified PPs are around 700 MPa, which is similar to that of the commercial *PP 4*. The commercial *PP 1* has the highest E-modulus and degree of crystallization, which lead to the highest geometric deformation value. The commercial *PP 2* and *PP 4* show very interesting properties. *PP 2* shows the lowest degree of crystallization but a significantly higher E-modulus, resulting in a relatively low geometric deformation value, which indicates that the influence of the degree of crystallization is very important with regard to part geometric deformation. In comparison, *PP 4* offers a higher degree of crystallization and lower E-modulus and features the lowest geometric deformation. In conclusion, these observations confirm that the combination of degree of crystallization and stiffness cause the final geometric deformation of 3D printed parts

Fig. 15 and Table 8 demonstrate the mechanical properties of neat *raco PP* grades and optimized *raco PP* blends compared with the commercial PP filaments. From Fig. 15(a), for 0° specimens, the tensile curves for neat *raco PPs* are very similar and the curves of the blended *raco PPs* show a similar progression, too. The general trend is that E-moduli and strengths decline from neat to blended *raco PPs*, while high strains of above 1400 % are obtained for all specimens. In contrast, the strains of 90° specimens show clear differences and are dramatically improved for the blended *raco PPs* compared with the neat specimens, which means the interlayer strain bonding quality is significantly enhanced by adding 10 wt% aPP. This trend is especially observed when blending *raco PP 2* with *aPP 2*, as here the 90° specimen's measured tensile strain is approximately 50 % of that of the corresponding 0° specimen. For neat *raco PP 2*, this anisotropic behavior only allows a

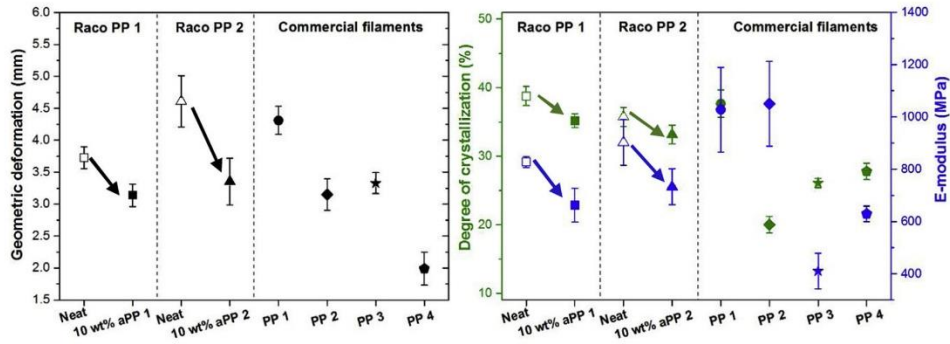


Fig. 14. (left) Geometric deformation and (right) degree of crystallization and E-moduli (90° orientation) of printed square tube specimens of *raco PP 1* and 2, the blends of *raco PP 1* and 10 wt% of *aPP 1*, *raco PP 2* and 10 wt% of *aPP 2*, and selected commercial PP filaments (hollow cube: *raco PP 1*, solid cube: *raco PP 1* with 10 wt% *aPP 1*, hollow triangle: *raco PP 2*, solid triangle: *raco PP 2* with 10 wt% *aPP 2*, filled circle: commercial *PP 1*, filled diamond: commercial *PP 2*, filled star: commercial *PP 3*, filled pentagon: commercial *PP 4*, arrows: tendency from neat raco PP to modified raco PP by blending with 10 wt% of *aPP 1* or *aPP 2*).

value of less than 5 %. As expected, a drop of tensile strength and E-modulus is observed for blended raco PPs due to the smoothness of amorphous polyolefin chains, which could act as a plasticizer. In Fig. 15(c) and (d), mechanical properties of all commercial PP filaments are compiled. The commercial *PP 1* demonstrates the highest tensile modulus and strength for the 0° specimen, but also the lowest strain interlayer bonding for the 90° specimen. Commercial *PP 2* and 3 show

similar tensile strengths but commercial *PP 2* exhibits significantly lower tensile strain. The commercial *PP 4* offers the strongest interlayer bonding among all commercial PPs and excellent mechanical properties as well. The observed differences in mechanical properties may be explained by the different chemical nature of the investigated PP grades, as there is a huge discrepancy between commercially available PP filaments. In conclusion, the key criteria for optimizing a PP filament for

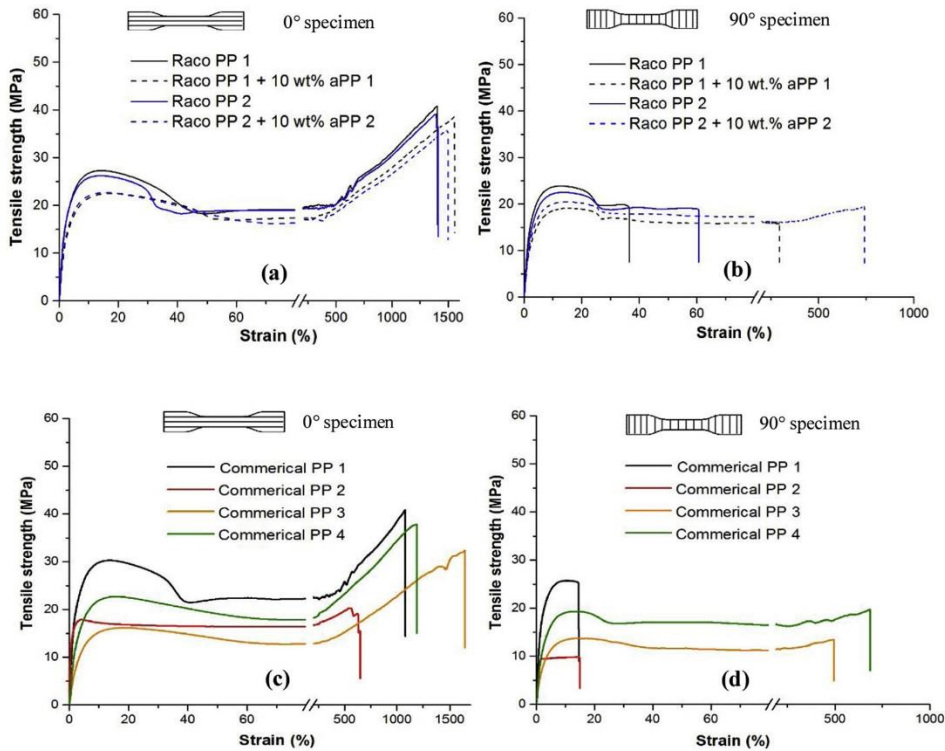


Fig. 15. Stress-strain curves of a) 0° specimens and b) 90° specimens of *raco PP 1*, *raco PP 1* with 10 wt% *aPP 1*, *raco PP 2*, and *raco PP 2* with 10 wt% *aPP 2* (*raco PP 1*: black solid line, *raco PP 1* with 10 wt% *aPP 1*: black dashed line, *raco PP 2*: blue solid line, *raco PP 2* with 10 wt% *aPP 2*: blue dashed line). Stress-strain curves of c) 0° specimens and d) 90° specimens of commercial PP filaments (commercial *PP 1* to 4: black, red, orange, and green solid lines). All shown stress-strain curves are a representative example of an actual measurement out of at least 10 specimens. (For interpretation of the references to colour in this figure legend, the reader is referred to the web version of this article).

Table 8

Mechanical properties of 0° and 90° oriented dog bones of neat raco PP 1 and 2, raco PP1 blended with aPP 1, raco PP 2 blended with aPP 2, and commercial PP 1–4 reference materials punched out of FFF printed square tubes.

Material	Orientation ^a	E [MPa] ^b	σ_{yt} [MPa] ^c	σ_{br} [MPa] ^d	ϵ_{br} [%] ^e
raco PP 1 neat	0°	841 (71) ^g	27.3 (0.4)	40.7 (1.3)	1400 (20)
	90°	828 (21)	23.9 (0.2)	20.0 (0.2)	35.9 (5.1)
raco PP 1 with 10 wt% aPP 1	0°	680 (16)	22.1 (0.4)	36.7 (1.6)	1535 (28)
	90°	663 (64)	19.4 (0.3)	19.9 (0.3)	283 (95)
raco PP 2 neat	0°	971 (19)	25.4 (0.6)	39.7 (0.8)	1429 (31)
	90°	903 (87)	22.1 (0.7)	18.5 (0.5)	57.0 (20)
raco PP 2 with 10 wt% aPP 2	0°	744 (46)	22.7 (0.5)	35.9 (0.5)	1484 (13)
	90°	733 (69)	20.4 (0.2)	20.4 (0.2)	690 (152)
commercial PP 1	0°	1073 (103)	28.4 (2.9)	41.5 (5.5)	1170 (80)
	90°	1028 (162)	24.9 (1.1)	24.9 (1.1)	9.5 (3.9)
commercial PP 2	0°	1267 (110)	16.1 (0.4)	16.7 (0.6)	405 (73)
	90°	1050 (162)	10.5 (0.4)	10.5 (0.4)	12.0 (4.0)
commercial PP 3	0°	420 (77)	15.8 (0.5)	33.4 (1.5)	1705 (132)
	90°	411 (68)	14.8 (0.4)	15.8 (0.4)	505 (81)
commercial PP 4	0°	635 (44)	22.5 (0.8)	44.7 (2.0)	1621 (83)
	90°	630 (29)	19.7 (0.5)	19.7 (0.5)	750 (75)

Standard deviation in parentheses.

^a Orientation of tensile loading direction to layer deposition direction.

^b E-modulus.

^c strength at yield.

^d strength at break.

^e elongation at break.

extrusion-based 3D printing are degree of crystallization, high mechanical properties, excellent interlayer bonding, as well as identifying the optimal balance of these three. One optimized raco PP was selected for a “jumping frog test” (Supplementary material S4) which is a simple and illustrative test to demonstrate the properties of a 3D printed thin wall geometries and the interlayer bonding quality.

4. Conclusions

The material shrinkage and limited interlayer bonding are issues in extrusion-based 3D printing of several commercially available PP filaments. In this context, the influence on the 3D printing performance of raco PP grades by adding a β -nucleating agent was investigated. The addition of the selected β -nucleating agent showed a slightly negative influence and could neither reduce the geometric deformation nor increase the interlayer strain bonding quality. By blending raco PP grades with one linear low-density polyethylene (LLDPE) also no improvement in the quality of the printed parts was observed. However, by blending raco PP grades with several amorphous polypropylene (aPP) grades less warp deformation and still adequate mechanical properties were achieved. In conclusion, the reported extensive and in-depth optimization of a tailored PP feedstock material led to the development of a successful material combinations which offers less warp deformation, high stiffness, and most importantly, outstanding interlayer strain bonding quality. The enhanced performance of 3D printed parts printed out of such an optimized raco PP/aPP blend feed stock material is visualized by a 3D printed frog model. Compared with commercially available PLA and ABS filaments only the raco PP/aPP blend allows repeatable jumps and withstands a static weight loading of 5 kg.

Author statement

Minde Jin: Experimental work, writing- original draft preparation
Christian Neuber: Supervision, writing and editing
Hans-Werner Schmidt: Supervision, writing and editing

Declaration of Competing Interest

None.

Acknowledgments

Special thanks to Jens Haalck from **TER Chemicals** and Dr. David Zopes from **KEYSER & MACKAY** for the kind supply of samples of the amorphous polyolefins.

Appendix A. Supplementary data

Supplementary material related to this article can be found, in the online version, at doi:<https://doi.org/10.1016/j.addma.2020.101101>.

References

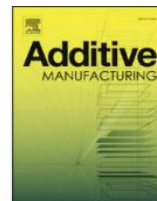
- [1] C.C. Ibeh, Thermoplastic Materials: Properties, Manufacturing Methods, and Applications, Taylor and Francis, Hoboken, 2014.
- [2] A.V. Shenoy, D.R. Saini, Thermoplastic melt rheology and processing, Dekker, New York, NY (1996).
- [3] O. Olabisi, K.P. Adewale (Eds.), Handbook of Thermoplastics, CRC Press Taylor & Francis Group, Boca Raton, London, New York, 2016.
- [4] S. Upcraft, R. Fletcher, The rapid prototyping technologies, *Assem. Autom.* 23 (2003) 318–330, <https://doi.org/10.1108/01445150310698634>.
- [5] S.-H. Ahn, M. Montero, D. Odell, S. Roundy, P.K. Wright, Anisotropic material properties of fused deposition modeling ABS, *Rapid Prototyp. J.* 8 (2002) 248–257, <https://doi.org/10.1108/13552540210441166>.
- [6] I. Gibson, D. Rosen, B. Stucker, Additive Manufacturing Technologies: 3D Printing, Rapid Prototyping and Direct Digital Manufacturing, Springer, New York, Heidelberg, Dordrecht, London, 2015.
- [7] T.-M. Wang, J.-T. Xi, Y. Jin, A model research for prototype warp deformation in the FDM process, *Int. J. Adv. Manuf. Technol.* 33 (2007) 1087–1096, <https://doi.org/10.1007/s00170-006-0556-9>.
- [8] Q. Sun, G.M. Rizvi, C.T. Bellehumeur, P. Gu, Effect of processing conditions on the bonding quality of FDM polymer filaments, *Rapid Prototyp. J.* 14 (2008) 72–80, <https://doi.org/10.1108/13552540810862028>.
- [9] Co. Stratasys, FDM Thermoplastics: Find Your FDM Thermoplastic, (2018) (Accessed 19 February 2019), <http://www.stratasys.com/de/materialien/fdm>.
- [10] Co. Makerbot, Makerbot Homepage, (2017) (Accessed 19 February 2019), <https://www.makerbot.com/>.
- [11] V. Kishore, C. Ajinjeru, A. Nycz, B. Post, J. Lindahl, V. Kunc, C. Duty, Infrared preheating to improve interlayer strength of big area additive manufacturing (BAAM) components, *Addit. Manuf.* 14 (2017) 7–12, <https://doi.org/10.1016/j.addma.2016.11.008>.
- [12] C. Bellehumeur, L. Li, Q. Sun, P. Gu, Modeling of bond formation between polymer filaments in the fused deposition modeling process, *J. Manuf. Process.* 6 (2004) 170–178, [https://doi.org/10.1016/S1526-6125\(04\)70071-7](https://doi.org/10.1016/S1526-6125(04)70071-7).
- [13] C.G. Schirmeister, T. Hees, E.H. Licht, R. Mühlaupt, 3D printing of high density polyethylene by fused filament fabrication, *Addit. Manuf.* 28 (2019) 152–159, <https://doi.org/10.1016/j.addma.2019.05.003>.
- [14] R. Singh, S. Singh, Development of nylon based FDM filament for rapid tooling application, *J. Inst. Eng. India Ser. C* 95 (2014) 103–108, <https://doi.org/10.1007/>

- s40032-014-0108-2.
- [15] F. Knoop, V. Schoepner, Mechanical and thermal properties of FDM parts manufactured with polyamide 12, *Proceeding of SFF Symposium* (2015) 935–948.
- [16] D.B. Malpass, E.I. Band, *Introduction to Industrial Polypropylene: Properties, Catalysts, Processes*, Wiley, Salem, Mass, Hoboken, N.J., 2012.
- [17] J. Karger-Kocsis, *Polypropylene Structure, Blends and Composites: Volume 3 Composites*, Springer Science & Business Media, 1995.
- [18] R.A. Phillips, *Macromorphology of polypropylene homopolymer tacticity mixtures*, *J. Polym. Sci. Part B: Polym. Phys.* **38** (2000) 1947–1964, [https://doi.org/10.1002/1099-0488\(20000801\)38:15<1947:AID-POLB10>3.0.CO;2-M](https://doi.org/10.1002/1099-0488(20000801)38:15<1947:AID-POLB10>3.0.CO;2-M).
- [19] J. Karger-Kocsis, Amorphous or atactic polypropylene, in: J. Karger-Kocsis (Ed.), *Polypropylene*, Springer Netherlands, Dordrecht, 1999, pp. 7–12.
- [20] J.Z. Jinneng Xie, CN104086891 A, (2014).
- [21] M. Spoerk, J. Sapkota, G. Weingrill, T. Fischinger, F. Arbeiter, C. Holzer, Shrinkage and warpage optimization of expanded-perlite-filled polypropylene composites in extrusion-based additive manufacturing, *Macromol. Mater. Eng.* **12** (2017) 1700143, <https://doi.org/10.1002/mame.201700143>.
- [22] D. Libster, A. Aserin, N. Garti, Advanced nucleating agents for polypropylene, *Polym. Adv. Technol.* **18** (2007) 685–695, <https://doi.org/10.1002/pat.970>.
- [23] J. Karger-Kocsis, J. Varga, Effects of β -? transformation on the static and dynamic tensile behavior of isotactic polypropylene, *J. Appl. Polym. Sci.* **62** (1996) 291–300, [https://doi.org/10.1002/\(SICI\)1097-4628\(19961010\)62:2<291:AID-APP4>3.0.CO;2-S](https://doi.org/10.1002/(SICI)1097-4628(19961010)62:2<291:AID-APP4>3.0.CO;2-S).
- [24] A.T. Jones, J.M. Aizlewood, D.R. Beckett, Crystalline forms of isotactic polypropylene, *Makromol. Chem.* **75** (1964) 134–158, <https://doi.org/10.1002/macp.1964.020750113>.
- [25] József Varga, β -Modification of isotactic polypropylene: preparation, structure, processing, properties, and application, *J. Macromol. Sci. Part B* (2002).
- [26] J. Kotek, M. Raab, J. Baldrian, W. Grellmann, The effect of specific: beta-nucleation on morphology and mechanical behavior of isotactic polypropylene, *J. Appl. Polym. Sci.* **85** (2002) 1174–1184, <https://doi.org/10.1002/app.10701>.
- [27] J. Výchopňová, V. Habrová, M. Obadal, R. Čermák, R. Čabla, Crystallization of polypropylene with a minute amount of β -nucleator, *J. Therm. Anal. Calorim.* **86** (2006) 687–691, <https://doi.org/10.1007/s10973-006-7894-6>.
- [28] H.B. Chen, J. Karger-Kocsis, J.S. Wu, J. Varga, Fracture toughness of α - and β -phase polypropylene homopolymers and random- and block-copolymers, *Polymer* **43** (2002) 6505–6514, [https://doi.org/10.1016/S0032-3861\(02\)00590-6](https://doi.org/10.1016/S0032-3861(02)00590-6).
- [29] M. Spoerk, F. Arbeiter, I. Raguž, G. Weingrill, T. Fischinger, G. Traxler, S. Schuschnigg, L. Cardon, C. Holzer, Polypropylene filled with glass spheres in extrusion-based additive manufacturing: effect of filler size and printing chamber temperature, *Macromol. Mater. Eng.* **303** (2018) 1800179, <https://doi.org/10.1002/mame.201800179>.
- [30] L. Wang, D.J. Gardner, Effect of fused layer modeling (FLM) processing parameters on impact strength of cellular polypropylene, *Polymer* **113** (2017) 74–80, <https://doi.org/10.1016/j.polymer.2017.02.055>.
- [31] L. Wang, J.E. Sanders, D.J. Gardner, Y. Han, Effect of fused deposition modeling process parameters on the mechanical properties of a filled polypropylene, *Prog. Addit. Manuf.* **3** (2018) 205–214, <https://doi.org/10.1007/s40964-018-0053-3>.
- [32] M. Gahlleitner, P. Jääskeläinen, E. Ratajski, C. Paulik, J. Reussner, J. Wolschweinger, W. Neißl, Propylene-ethylene random copolymers: comonomer effects on crystallinity and application properties, *J. Appl. Polym. Sci.* **95** (2005) 1073–1081, <https://doi.org/10.1002/app.21308>.
- [33] W. Tang, J. Tang, H. Yuan, R. Jin, Crystallization behavior and mechanical properties of polypropylene random copolymer/poly(ethylene-octene) blends, *J. Appl. Polym. Sci.* **122** (2011) 461–468, <https://doi.org/10.1002/app.34162>.
- [34] M. Jin, R. Giesa, C. Neuber, H.-W. Schmidt, Filament materials screening for FDM 3D printing by means of injection-molded short rods, *Macromol. Mater. Eng.* **303** (2018) 1800507, <https://doi.org/10.1002/mame.201800507>.
- [35] O.S. Carneiro, A.F. Silva, R. Gomes, Fused deposition modeling with polypropylene, *Mater. Des.* **83** (2015) 768–776, <https://doi.org/10.1016/j.matdes.2015.06.053>.
- [36] L. Wang, W. Gramlich, D. Gardner, Y. Han, M. Tajvidi, Spray-dried cellulose nanofibril-reinforced polypropylene composites for extrusion-based additive manufacturing: nonisothermal crystallization kinetics and thermal expansion, *J. Compos. Sci.* **2** (2018) 7, <https://doi.org/10.3390/jcs2010007>.
- [37] B. Kaynak, M. Spoerk, A. Shirole, W. Ziegler, J. Sapkota, Polypropylene/cellulose composites for material extrusion additive manufacturing, *Macromol. Mater. Eng.* **303** (2018) 1800037, <https://doi.org/10.1002/mame.201800037>.
- [38] M. Spoerk, C. Savandiah, F. Arbeiter, J. Sapkota, C. Holzer, Optimization of mechanical properties of glass-spheres-filled polypropylene composites for extrusion-based additive manufacturing, *Polym. Compos.* **83** (2017) 768, <https://doi.org/10.1002/pc.24701>.
- [39] M. Spoerk, C. Savandiah, F. Arbeiter, G. Traxler, L. Cardon, C. Holzer, J. Sapkota, Anisotropic properties of oriented short carbon fibre filled polypropylene parts fabricated by extrusion-based additive manufacturing, *Compos. Part A Appl. Sci. Manuf.* **113** (2018) 95–104, <https://doi.org/10.1016/j.compositesa.2018.06.018>.
- [40] M. Spoerk, J. Gonzalez-Gutierrez, C. Lichal, H. Cajner, G. Berger, S. Schuschnigg, L. Cardon, C. Holzer, Optimisation of the adhesion of polypropylene-based materials during extrusion-based additive manufacturing, *Polymers* **10** (2018) 490, <https://doi.org/10.3390/polym10050490>.
- [41] Borealis Co, RD208CF: Product Data Sheet, (2013) (Accessed 15 May 2019), <http://www.borealisgroup.com/en/polyolefins/products/Others/RD208CF/>.
- [42] Lyondellbasell, Moplen RP220M: Technical Data Sheet, (2014) (Accessed 20 February 2019), <http://img9.cntrades.com/201603/23/15-12-22-75-1009588.pdf>.
- [43] Sigma Aldrich, Polypropylene- Amorphous. <https://www.sigmaaldrich.com/catalog/product/aldrich/428175?lang=de®ion=DE> (Accessed 28 Oct. 2019).
- [44] Rectax, Rectax APAO datasheet: APAO. <http://www.rectax.com/pdf/rectax-automotive-transportationadhesives-v1-final.pdf> (Accessed 28 Oct. 2019).
- [45] A.G. Evonik, Vestoplast: Datasheet, (2017) (Accessed 21 March 2019), <https://adhesive-resins.evonik.com/product/adhesive-resins/downloads/vestoplast%20brochure%202016.pdf>.
- [46] Eastman, Eastman Aerafin™ 17 Polymer: Technical Data Sheet, (2018) (Accessed 16 May 2019), https://productcatalog.eastman.com/tds/ProdDatasheet.aspx?product=71103020&pn=Aerafin+-+17+Polymer#_ga=2.85972122.2076261317.1550740489-1185642349.1550740489.
- [47] Exxonmobil, LLDPE LL6101: Production Datasheet, (2017) (Accessed 20 February 2019), <https://exxonmobilchemical.ides.com/datasheet.aspx?l=58933&FMT=PDF&CULTURE=en-US&PS=PE&E=244026>.
- [48] German RepRap, PP Polypropylen Filament. <https://www.germanreprap.com/produkt.aspx?WPPParams=50C9D4C6C5D2E6BDA5A98392A9> (Accessed 2 June 2019).
- [49] PopBit 3D Tec Co., PP-PE Filament. <http://www.3d-popbit.com/pp-pe-filament/3d-pe-filament/pp-pe-filament-for-3d-printer.html> (Accessed 28 Oct. 2019).
- [50] Ultimaker, UltiMaker PP, (2019) (Accessed 2 June 2019), <https://ultimaker.com/materials/pp>.
- [51] PPrint GmbH, PPrint, (2018) (Accessed 19 February 2019), <https://www.ppprint.de/>.
- [52] Orbi-Tech, Orbi-Tech Smart ABS Nature 3 mm Filament, (2019) (Accessed 19 February 2019), <https://orbi-tech.de/shop/3D-Filamente/smartABS/3-mm-smartABS/smartABS-Filament-3-mm-750-g-Natur:461.html>.
- [53] Orbi-Tech, Orbi-Tech PLA White 3 mm Filament, (2019) (Accessed 18 February 2019), <https://orbi-tech.de/shop/3D-Filamente/PLA/3-mm-PLA/PLA-Filament-3-mm-750-g-Weiss:257.html>.
- [54] B. Lotz, α and β phases of isotactic polypropylene: a case of growth kinetics 'phase reentrancy' in polymer crystallization, *Polymer* **39** (1998) 4561–4567, [https://doi.org/10.1016/S0032-3861\(97\)10147-1](https://doi.org/10.1016/S0032-3861(97)10147-1).
- [55] C. Mathieu, A. Thierry, J.C. Wittmann, B. Lotz, Specificity and versatility of nucleating agents toward isotactic polypropylene crystal phases, *J. Polym. Sci. Part B: Polym. Phys.* **40** (2002) 2504–2515, <https://doi.org/10.1002/polb.10309>.
- [56] G.-y. Shi, B. Huang, J.-y. Zhang, Enthalpy of fusion and equilibrium melting point of the beta-form of polypropylene, *Makromol. Chem. Rapid Commun.* **5** (1984) 573–578, <https://doi.org/10.1002/marc.1984.030050915>.
- [57] F.M. Mirabella, A. Bafna, Determination of the crystallinity of polyethylene/?-olefin copolymers by thermal analysis: Relationship of the heat of fusion of 100% polyethylene crystal and the density, *J. Polym. Sci. Part B: Polym. Phys.* **40** (2002) 1637–1643, <https://doi.org/10.1002/polb.10228>.
- [58] W. Stocker, M. Schumacher, S. Graff, A. Thierry, J.-C. Wittmann, B. Lotz, Epitaxial crystallization and AFM investigation of a frustrated polymer structure: isotactic poly(propylene), β phase, *Macromolecules* **31** (1998) 807–814, <https://doi.org/10.1021/ma971345d>.
- [59] J. Varga, Modification change during spherulitic growth of polypropylene, *Angew. Makromol. Chemie* **104** (1982) 79–87, <https://doi.org/10.1002/apmc.1982.051040107>.

Contents lists available at [ScienceDirect](#)

Additive Manufacturing

journal homepage: www.elsevier.com/locate/addma



Supplementary material:

Tailoring polypropylene for extrusion-based additive manufacturing

Minde Jin, Christian Neuber*, Hans-Werner Schmidt*

Macromolecular Chemistry I and Bavarian Polymer Institute (BPI), University of Bayreuth, Universitätsstraße 30, 95447 Bayreuth, Germany

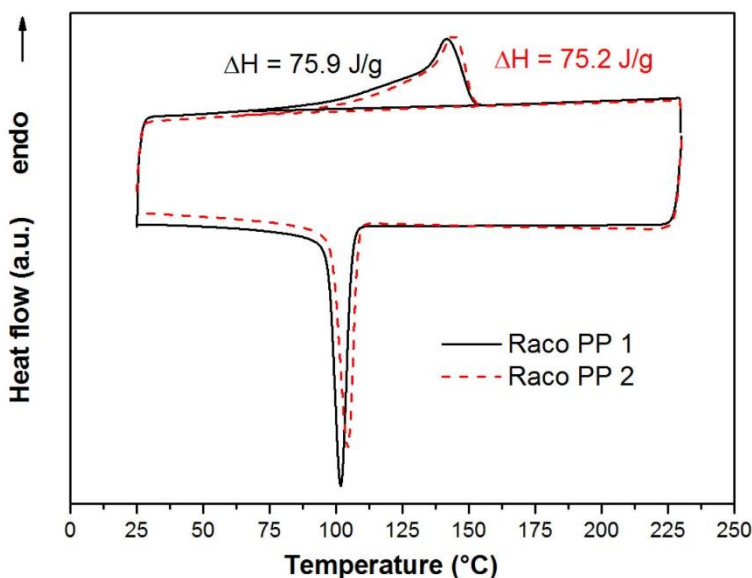
* E-mail: christian.neuber@uni-bayreuth.de; hans-werner.schmidt@uni-bayreuth.de

Table of contents

1. DSC curves of investigated raco PP 1 and raco PP 2	2
2. Mechanical testing and thickness correction	2
3. Raco PP 2 blend with different aPPs and one LLDPE	3
4. Jumping frog test	6

1. DSC curves of investigated *raco PP 1* and *raco PP 2*

Thermal properties and degree of crystallization of samples were investigated using differential scanning calorimetry (DSC). Samples were cut out of the middle area from corresponding square tube side walls. The first heating curve was used for the melt enthalpy peak area integration (see *SI*) for the calculation of degree of crystallization (see also Chapter 2.6 “Thermal analysis and evaluation of degree of crystallization”). The integration of each enthalpy peak area was evaluated in range from 60 °C to 160 °C with the STARe software.



SI. First heating and cooling curves of DSC measurements from *raco PP 1* (black solid line) and *raco PP 2* (red dashed line) and corresponding melt enthalpies ΔH . DSC measurements were performed under nitrogen atmosphere within the temperature range of 25°C to 230 °C at a heating/cooling rate of 10 K/min.

2. Mechanical testing and thickness correction

In this work, tensile specimens with the angle of 90° and 0° to the layer deposition direction were punched out and used for the determination of interlayer strain bonding quality and bulk mechanical properties, respectively. But for the calculation of the mechanical properties, the true specimen thicknesses for both 90° specimens and 0° specimens are required. Here we identified the effective bonding thickness as the measured thickness minus twice the profile height R_z originated by the layer by layer preparation. For 0° specimens, the measured thickness minus one profile height was used for the effective thickness calculation (see also [1]).

The surface profile height R_z is defined as the ten points average distance between peaks (5 highest points) and valleys (5 lowest points) of the surface profile measured along the layer deposition

direction (Z axis) [2,3]. The thickness measured with a digital micrometer is regarded as overall thickness δ_{measured} of the fused material. The thickness of tensile tested specimens for correction refers to the effective bonding thickness $\delta_{\text{effective}}$ between the individual layers.

For 90° tensile specimen, *E*-Modulus *E* and strength σ correction according the following equations:

$$E_{\text{corrected}} = E_{\text{measured}} * \frac{\delta_{\text{measured}}}{\delta_{\text{measured}} - 2R_z} \quad (1)$$

$$\sigma_{\text{corrected}} = \sigma_{\text{measured}} * \frac{\delta_{\text{measured}}}{\delta_{\text{measured}} - 2R_z} \quad (2)$$

For 0° tensile specimen, *E*-Modulus *E* and strength σ correction according the following equations:

$$E_{\text{corrected}} = E_{\text{measured}} * \frac{\delta_{\text{measured}}}{\delta_{\text{measured}} - R_z} \quad (3)$$

$$\sigma_{\text{corrected}} = \sigma_{\text{measured}} * \frac{\delta_{\text{measured}}}{\delta_{\text{measured}} - R_z} \quad (4)$$

3. Raco PP 2 blend with different aPPs and one LLDPE

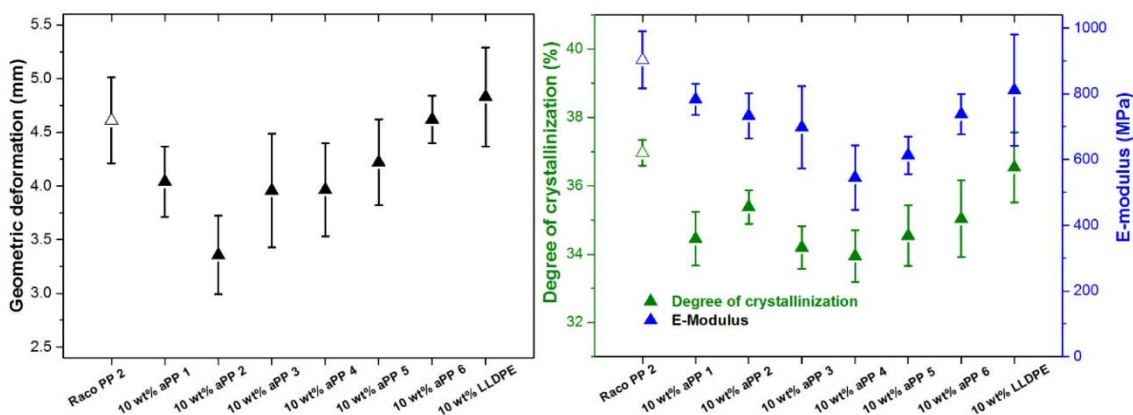
Beside the two commercial grade polypropylene/ethylene random copolymers which serve as neat base PP materials for optimizations six different amorphous polypropylene-based polyolefins were selected for optimization and blended with the two raco PPs. An overview of the technical data of all investigated amorphous polyolefins is given in *Table 1*.

Table 1.
Technical data of investigated amorphous polyolefins

Amorphous Polyolefin	Supplier	Grade	Color	Softening point ^{a)} (°C)	Melt viscosity ^{b)} (cps)
<i>aPP 1</i>	Sigma-Aldrich	9003-07-0 [4]	natural	150	-
<i>aPP 2</i>	Rectax	RT 2115 [5]	natural	152	1500
<i>aPP 3</i>	Evonik	EP V2103 [6]	natural	103	2500 ± 500
<i>aPP 4</i>	Evonik	Vestoplast 608 [6]	natural	157	9000 ± 3000
<i>aPP 5</i>	Evonik	Vestoplast 891 [6]	natural	152	115,000 ± 35,000
<i>aPP 6</i>	Eastman	Aerafin 17 [7]	natural	130	1700

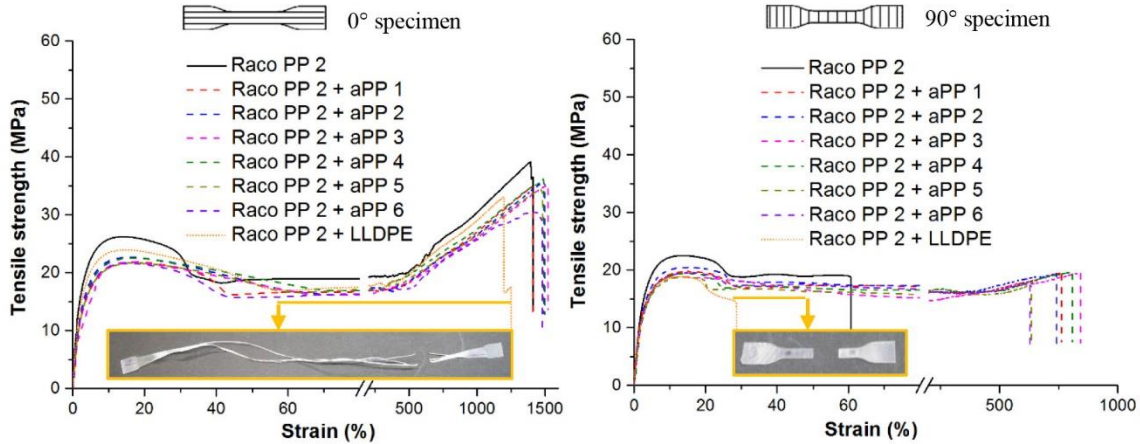
^{a)} ring and ball softening point, ^{b)} melt viscosity at 190 °

To investigate the influence of different types of amorphous polyolefins, the identified optimized 10 wt% content was used for the preparation of additional blends of *raco PP 2* with selected aPPs (*aPP 1* to *aPP 6*), as well as one LLDPE. **S2** shows the measured geometric deformations (*left*) and degree of crystallization and E-moduli (*right*) of neat *raco PP 2* and *raco PP 2* blends with 10 wt% of *aPP 1* – *aPP 6* or LLDPE. While blended specimens of *aPP 1* to *aPP 5* demonstrate reduced geometric deformation compared to the neat *raco PP 2*, an increase in shrinkage is observed for specimens blended with *aPP 6* or LLDPE. This finding is supported by the measured degree of crystallization shown in **S2** (right), with the LLDPE blend showing the highest degree of crystallization of the investigated blends. Degree of crystallization are clearly decreased by blending *raco PP 2* with aPPs; among them, *aPP 4* is the most effective, reducing degree of crystallization by about 15 % compared with neat *raco PP 2*.



S2: Influence of *aPP 1* – *aPP 6* or LLDPE blended with *raco PP 2* on (left) geometric deformation (black hollow triangle: neat *raco PP 2* sample, black solid triangles: *raco PP 2* blended with *aPP 1* – *aPP 6* or LLDPE) and (right) degree of crystallization and E-moduli (90° orientation) of printed square tube samples (black hollow triangle: neat *raco PP 2* sample, green solid triangle: *raco PP 2* blended with *aPP 1* – *aPP 6* or LLDPE, blue hollow triangle: neat *raco PP 2* samples, blue solid triangles: *raco PP 2* blended with *aPP 1* – *aPP 6* or LLDPE).

In addition, stress strain curves were measured of neat *raco PP 2* and *raco PP 2* blends with 10 wt% of *aPP 1* – *aPP 6* or LLDPE (see **S3** and **Table 2**).



S3. Tensile curves of (left) 0° specimens and (right) 90° specimens (neat *raco PP 2*: black solid line, *raco PP 1* with 10 wt% *aPP 1*: red dashed line, *raco PP 2* with 10 wt% *aPP 2*: blue dashed line, *raco PP 2* with 10 wt% *aPP 3*: pink dashed line, *raco PP 2* with 10 wt% *aPP 4*: green dashed line, *raco PP 2* with 10 wt% *aPP 5*: gold dashed line, *raco PP 2* with 10 wt% *aPP 6*: purple dashed line, *raco PP 2* with 10 wt% *LLDPE*: orange solid line). Images of broken 0° and 90° dog bones (from *raco PP 2* with 10 wt% *LLDPE*) are shown at the bottom of the graphs. All curves show a measured tensile curve, representing the mechanical properties of one test series consists at least 10 specimens.

In **S3** (left), all investigated 0° specimens show very similar tensile strains. Neat *raco PP 2* demonstrates the highest E-modulus, strength at yield, and strength at break. In **S3** (right), more effective screening and evaluation of corresponding interlayer bonding properties of 3D printed parts can be realized since 90° specimens are investigated. Crystal spherulite blends with aPPs allow boundaries to be filled [8] and thus their 90° specimens feature higher interlayer bonding qualities, but the tensile strain values are more scattered compared to those of the 0° specimens. Especially the 90° specimen blended with 10 wt% of *LLDPE* shows significant mechanical property loss compared to its 0° specimen and even more compared to the blends of *raco PP 2* and all aPPs. Furthermore, all 90° specimens of blends of *raco PP 2* and *aPP 1 – 6* (**S3** (right)) show clear improvement in interlayer strain bonding quality compared with neat *raco PP 2*.

Table 2.

Mechanical properties of 0° and 90° oriented dog bones of neat *raco PP 2* and *raco PP 2* blended with *aPP 1 - 6* or *LLDPE* punched out of FFF printed square tubes.

Material	Orientation ^{a)}	<i>E</i> [MPa] ^{b)}	σ_{yi} [MPa] ^{c)}	σ_{br} [MPa] ^{d)}	ϵ_{br} [%] ^{e)}
<i>raco PP 2 neat</i>	0°	971 (19) ^{f)}	25.4 (0.6)	39.7 (0.8)	1429 (31)
	90°	903 (87)	22.1 (0.7)	18.5 (0.5)	57.0 (20)
<i>raco PP 2 with 10 wt% aPP 1</i>	0°	769 (12)	21.2 (0.4)	35.0 (1.1)	1467 (44)
	90°	783 (48)	19.4 (0.4)	19.4 (0.4)	664 (135)
<i>raco PP 2 with 10 wt% aPP 2</i>	0°	744 (46)	22.7 (0.5)	35.9 (0.5)	1484 (13)
	90°	733 (69)	20.4 (0.2)	20.4 (0.2)	690 (152)
<i>raco PP 2 with 10 wt% aPP 3</i>	0°	749 (90)	22.1 (0.6)	35.2 (1.7)	1600 (191)
	90°	698 (125)	18.9 (0.5)	18.9 (0.5)	666 (188)
<i>raco PP 2 with 10 wt% aPP 4</i>	0°	557 (105)	22.0 (0.4)	35.1 (1.6)	1459 (101)
	90°	545 (98)	19.6 (0.4)	19.6 (0.4)	561 (191)
<i>raco PP 2 with 10 wt% aPP 5</i>	0°	652 (90)	22.4 (0.4)	36.7 (0.6)	1540 (48)
	90°	613 (57)	18.8 (0.4)	18.8 (0.4)	641 (44)
<i>raco PP 2 with 10 wt% aPP 6</i>	0°	762 (116)	22.6 (0.7)	35.2 (0.4)	1457 (31)
	90°	738 (61)	19.5 (0.9)	19.5 (0.9)	657 (72)
<i>raco PP 2 with 10 wt% LLDPE</i>	0°	859 (90)	23.8 (0.7)	36.4 (1.2)	1353 (93)
	90°	811 (170)	19.2 (0.4)	15.2 (0.2)	26.0 (7.9)

^{a)} Orientation of tensile loading direction to layer deposition direction, ^{b)} E-modulus, ^{c)} strength at yield, ^{d)} strength at break, ^{e)} elongation at break, ^{f)} standard deviation in parentheses

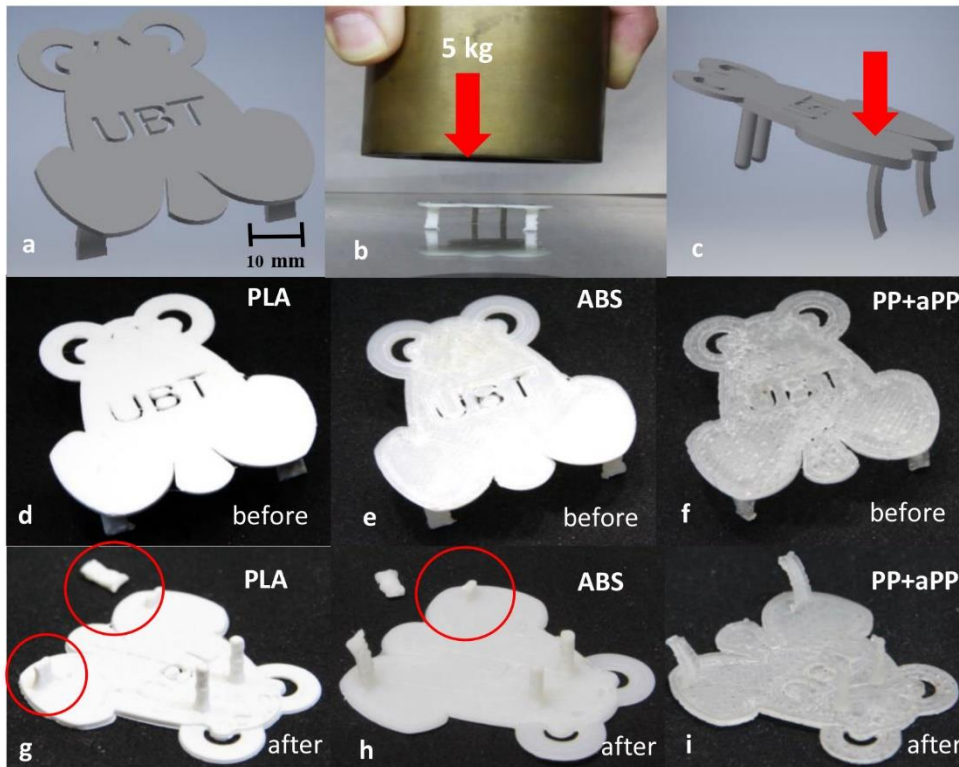
4. Jumping frog test

In order to demonstrate the excellent interlayer strain bonding quality of *raco PP* blended with *aPP* 3D printed parts, small, more precise “jumping frogs” were FFF 3D printed, utilizing optimized *raco PP 1* with 10 wt% *aPP 1* as well as commercial ABS and PLA filaments for reference purposes (*S4* (a-c)). The modified PP and ABS were printed at 250 °C extrusion temperature/120 °C bed temperature, and PLA was printed at 210 °C extrusion temperature/60 °C bed temperature. For all printed frogs printing speed was 15 mm/s, layer height 250 μm, and fan speed 100%.

A jumping frog 3D model was selected as the frog legs are the most critical parts and clearly demonstrate the interlayer bonding qualities of the utilized feedstock materials when they need to bend, as in with a jump. The frog is designed as simply and lightweight as possible for successful jumping. However, the utilized material should feature certain strength and stiffness during the

force loading on top and the legs should be bendable for temporary energy storage. Upon quickly releasing the applied force loading, the legs should recover into their original positions and push the frog to jump. In detail, two investigations were conducted: i) static weight loading and ii) frog jumping.

When a static weight of 5 kg was loaded on top of the frogs (**S4** (b)), one hind leg or both hind legs of the PLA and ABS frogs always cracked (**S4** (d and e)). Only the frog 3D printed with blended *raco PP 1* and *aPP 1* exhibited reversible bending of the hind legs (**S4** (i)). A very similar behavior was observed for the frog jumping. Again, hind legs of the PLA and ABS frogs typically failed and cracked, while the frog prepared from the blended *raco PP 1* and *aPP 1* could be used for several successful jumps.



S4. **a)** CAD model of jumping frog, **b)** static weight loading test, **c)** jumping frog test: By pressing on top above the hind leg and after quickly releasing the applied force loading, the frog jumps forward, **d)-f)** top view of frogs 3D printed out of PLA, ABS, and blended *raco PP 1* and *aPP 1* before static weight loading and jumping, **d)-f)** bottom view of frogs 3D printed out of PLA, ABS, and blended *raco PP 1* and *aPP 1* after static weight loading.

References

- [1] M. Jin, R. Giesa, C. Neuber, H. - W. Schmidt, Filament Materials Screening for FDM 3D Printing by Means of Injection - Molded Short Rods, *Macromol. Mater. Eng.* 303 (2018) 1800507. <https://doi.org/10.1002/mame.201800507>.
- [2] Veeco Co., Surface Measurement Parameters for Wyko® Optical Profilers, 2002. http://zeus.plmsc.psu.edu/~manias/MatSc597/docs/di_roughness.pdf (accessed 19 February 2019).
- [3] E.S. Gadelmawla, M.M. Koura, T.M.A. Maksoud, I.M. Elewa, H.H. Soliman, Roughness parameters, *Journal of Materials Processing Technology* 123 (2002) 133–145. [https://doi.org/10.1016/S0924-0136\(02\)00060-2](https://doi.org/10.1016/S0924-0136(02)00060-2).
- [4] Sigma Adrich, Polypropylene- Amorphous. <https://www.sigmaaldrich.com/catalog/product/aldrich/428175?lang=de®ion=DE> (accessed 28.Oct.2019).
- [5] Rectax, Rectax APAO datasheet: APAO. <http://www.rextac.com/pdf/rextac-automotive-transportationadhesives-v1-final.pdf> (accessed 2 June 2019).
- [6] Evonik AG, Vestoplast: Datasheet, 2017. <https://adhesive-resins.evonik.com/product/adhesive-resins/downloads/vestoplast%20brochure%202016.pdf> (accessed 21 March 2019).
- [7] Eastman, Eastman Aerafin™ 17 Polymer: Technical Data Sheet, 2018. https://productcatalog.eastman.com/tds/ProdDatasheet.aspx?product=71103020&pn=Aerafin+-+17+Polymer#_ga=2.85972122.2076261317.1550740489-1185642349.1550740489 (accessed 16 May 2019).
- [8] R.A. Phillips, Macromorphology of polypropylene homopolymer tacticity mixtures, *J. Polym. Sci. B Polym. Phys.* 38 (2000) 1947–1964. [https://doi.org/10.1002/1099-0488\(20000801\)38:15<1947:AID-POLB10>3.0.CO;2-M](https://doi.org/10.1002/1099-0488(20000801)38:15<1947:AID-POLB10>3.0.CO;2-M).

4.5 (AB)_n segmented copolyetherimides for 4D printing

(AB)_n segmented copolyetherimides for 4D printing

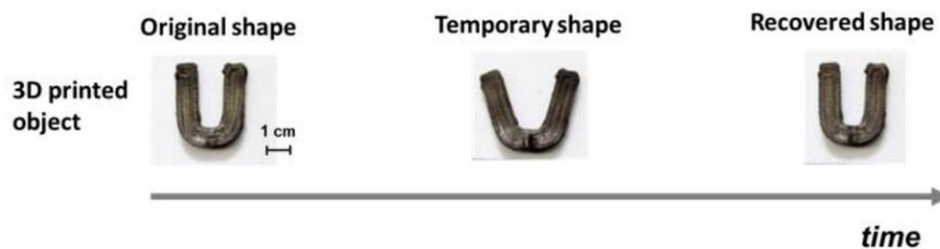
Minde Jin, Markus Stihl, Reiner Giesa, Christian Neuber, Hans-Werner Schmidt**

*Macromolecular Chemistry and Bavarian Polymer Institute (BPI), University of Bayreuth,
Universitätsstraße 30, 95447 Bayreuth, Germany*

* E-mail: christian.neuber@uni-bayreuth.de, hans-werner.schmidt@uni-bayreuth.de

ToC ABSTRACT FIGURE

(AB)_n segmented copolyetherimides consisting of perylene and poly(ethylene glycol) segments are tailored for extrusion-based additive manufacturing and 4D printing.



Keywords:

Extrusion-based additive manufacturing, 3D printing, 4D printing, shape memory, (AB)_n segmented copolymers

Abstract:

The fourth dimension in 4D printing comprises the ability of materials to recover their shape by utilizing 3D printing in combination with shape memory polymers. The focus of this work is on 3D printing of physically crosslinked thermoplastic polymers, which allow a reversible transformation of a temporary to its original shape by an external stimulus temperature, thus realize 4D printing. In this context, $(AB)_n$ segmented copolyetherimides consisting of perylene and poly(ethylene glycol) (PEG) segments were synthesized and characterized regarding their thermal and rheological properties in view of 3D printing. The perylene imide segments act as reversible physical crosslinks which disassemble at temperatures between 100 and 200 °C. The PEG segments exhibit a low melting temperature around 40 to 60 °C and are semi-crystalline at room temperature and enable 4D printing. The results show that this type of $(AB)_n$ segmented copolyetherimides combine reliable 3D printing performance, indicated by low warp deformation and excellent interlayer bonding. With a blend of two copolymers, we were able to realize 4D printing.

1. Introduction

Among 3D printing technologies, extrusion-based additive manufacturing (AM), often referred to as fused filament fabrication (FFF), fused layer manufacturing (FLM), or fused deposition modeling (FDM), is a widely used technique.^[1-3] Here AM combines a simplified thermoplastic extrusion process with computer-numerical-controlled (CNC) technology enabling cost-effective layered processing of 3D printed parts. A feeding system conveys polymer filaments into a liquefier, and the molten material is deposited through a nozzle in a layer by layer fashion.^[4] Processing parameters, such as printing platform temperature, nozzle temperature, as well as nozzle path and printing speed, directly influence the performance of the final printed part.^[5] Due to the unique layered fabrication process, the successively deposited extrusion lines are fused together by thermal energy and mechanical pressure of the moving hot nozzle during printing.^[6] Compared with injection molding, FFF printed parts exhibit more anisotropy due to reduced interlayer bonding quality.^[5] Printing semi-crystalline polymers with a low degree of crystallinity (e.g. polyamide 12 or polyurethane) gain reinforcement as a result of interchain crystallization at the interface. However, semi-crystalline polymers with a higher degree of crystallinity, such as polyethylene (PE) or polypropylene (PP), exhibit detrimental material shrinkage of the printed part.^[7-15]

Smart materials are also in the focus of 3D printing as they offer distinct advantages.^[16] The combination of smart materials and 3D printing is reported in several review articles using the term '4D printing'.^[16-20] 4D printing allows a printed part to change its shape or function with time in response to stimuli such as pressure, temperature, pH, swelling/shrinking, or light.^[21] 4D printing opens up new pathways for creating diverse shape-shifting concepts and functionalities, e.g., soft robotics, drug delivery, tissue engineering, or biomedical devices.^[21,22] 3D printing of shape memory polymers (SMP) enables 4D printing. SMPs can be chemically tailored to allow sophisticated applications.^[21,23] For shape memory, a stimulus (temperature,

moisture, etc.) is necessary to lead to a transformation from a temporary shape to the programmed original shape.^[24–27] Commonly the shape memory effect is thermally induced. Such materials are called thermosensitive SMPs. For the shape memory effect, three requirements are essential: (i) crosslinks acting as fixation of the original shape, (ii) a second type of physical crosslinks acting as defeasible fixation of the temporary shape allowing reversible switching, and (iii) a certain degree of elasticity as shape recovery driving force.^[28,29]

The first type of crosslinks can be either chemically (covalent bonds) or physically (intermolecular interactions).^[24] Physical crosslinks require a polymer morphology that consists of at least two separated domains, e.g., a crystalline and an amorphous phase. Another polymer morphology with physical crosslinks is present in $(AB)_n$ segmented copolymers and thermoplastic elastomers.^[30] Here separated domains of the copolymer chain form hard segments that act as crosslinks and break or, more precisely, disassemble at an elevated temperature ($T_{\text{trans.}(high)}$). For shape switching, a second type of reversible physical crosslinking is required at a lower temperature ($T_{\text{trans.}(low)}$). This transition is necessary for the fixation of the temporary shape. The transition at $T_{\text{trans.}(low)}$ can be either recrystallization or the glass transition of domains formed by the more flexible (soft) segments. Thus, by heating above $T_{\text{trans.}(low)}$, a certain elasticity is reached, and in combination with the stored inner energy, transformation from temporary shape to original shape occurs. Therefore, these domains are often called switching domains.^[29] In recent years, a rapidly increased number of publications have been reported on 3D and 4D printing materials and extrusion-based AM, utilizing thermoplastic elastomers such as polyurethanes.^[17,21] However, such soft filament materials are a major challenge for the feeding systems of 3D printers. The low stiffness combined with high melt viscosity can cause filament buckling which impedes the printing process.^[31]

In this paper, $(AB)_n$ segmented copolyetherimides consisting of perylene and poly(ethylene glycol) (PEG) segments were synthesized to realize 3D and 4D printing for the first time with

this class of copolymers. The same type of $(AB)_n$ copolyetherimide was synthesized as anode material in all-organic polymer batteries.^[32] Similar polymers were also investigated, for example, in organic photovoltaics.^[33-36] In this work, aimed at 3D and 4D printing, perylene imide segments should act as reversible physical crosslinks disassembling at elevated temperatures ($T_{\text{trans.}(high)}$) while the PEG segments which are semi-crystalline at room temperature and melt around 50 °C ($T_{\text{trans.}(low)}$) should enable shape switching. Also, the crystallinity of PEG segments should improve the filament quality concerning feeding issues in extrusion-based 3D printing.

2. Experimental Part

2.1. Materials

Polyethylene glycol diamines with molecular weights of about 2000 and 8000 g/mol were synthesized from corresponding PEG diols via PEG-ditosylate intermediates in analogy to a known procedure.^[37,38] Jeffamine[®] ED-900 (o,o'-bis(2-aminopropyl)polypropylene glycol-*block*-polyethylene glycol-*block*-polypropylene glycol, CAS-No: 65605-36-9) was purchased from Sigma Aldrich.^[39] The molecular weights of PEG diamines were determined by titration against 0.1 M HCl solution as $M_n = 1998 \text{ g mol}^{-1}$ and $M_n = 7998 \text{ g mol}^{-1}$ for PEG diamines and as $M_n = 971 \text{ g mol}^{-1}$ for the Jeffamine[®] ED900. Perylene-3,4,9,10-tetracarboxylic dianhydride (CAS-No: 81-30-1) was purchased from Sigma Aldrich and used as received.

2.2. Synthesis of (AB)_n segmented copolymers

The synthesis of the copolyetherimides **1a** and **1b** was carried out in a one-pot-melt polycondensation by reacting perylene-3,4,9,10-tetracarboxylic dianhydride with the corresponding polyethylene glycol diamine in a molar ratio of 1:1.25 (perylene: diamine). The reaction was performed at 180 °C (melt) for 24 h in a stainless-steel reactor with mechanical stirring under argon atmosphere. The completion of the reaction was confirmed with FT-IR spectroscopy. The obtained products were used without further purification. Copolyetherimide **2** with a Jeffamine[®] ED900 instead of the PEG segment was synthesized in the same manner.

2.3. Thermal analysis

Differential scanning calorimetry (DSC) was conducted using a Mettler Toledo[®] DSC 2 STAR^e system under a nitrogen atmosphere from 25 to 250 °C at a heating/cooling rate of 10 K/min. Values of the melting/crystallization temperatures of the PEG segments and the

disassembly/assembly temperature of perylene segments were read from the peak maximum of the second heating and cooling run, respectively.

2.4. Rheological characterization

Oscillatory shear rheology experiments were performed on a rheometer (Kinexus lab+, Malvern Panalytical) using a 25 mm plate-plate geometry at a cooling rate of 2 K/min and a frequency of 0.5 Hz in a temperature range from 200 to 5 °C. For the cooling run at the beginning, a constant shear strain of 0.1% was applied then switched to constant shear stress at 1000 Pa.

2.5. Lab-scale filament rod processing

The detailed preparation of lab-scale filament rods is described in a previous publication.^[12] Using a 12 ml Xplore Microinjection molder, chunks of the copolymers were molten in the barrel for approx. 4 min at 200 °C for **1a** and 190 °C for **1b**. The blend **3** consisting of **1b** and **2** was prepared using a Carver 2518 hot press to mix both copolymers by compression molding of a blend **3** film, folding the film, and repeating the compression molding and folding procedure for at least 10 times. The melt was then directly injected into a metal mold containing a Teflon[®] tube with an inner diameter of 3.0 mm. Several individual filament rods obtained this way were welded together into a filament of around 90 cm length by fixating the rods in a short Teflon[®] tube and a heat gun as heat source (see *Supporting Information S2*).

2.6. 3D printing

A fused filament fabrication (FFF) desktop 3D printer (3NTR[®] A4, Italy) was used in this study. The nozzle diameter was 450 μm . The 3D digital models of the geometries were first designed with Autodesk[®] Fusion 360 and additionally sliced with the software Slic3r (Version 1.3.0). For the optimization of the printing variables, a free-standing square tube of 1 x 1 cm in the base area and 1 to 5 cm in height was printed.^[12] For evaluation of printed part performance, a free-standing square tube of 5 x 5 cm base area and 5 cm in height consisting of a single line stack was 3D printed. The resulting thickness of the obtained side wall was around 750 μm . As 3D printing build surface, Scotch Blue Tape 2090 from 3M[®] was used. To achieve dimensional stable and defect-free printed parts, each printing was optimized regarding processing parameters, such as extruder and printing platform temperature, and cooling fan speed (see Table S1).

2.7. Mechanical properties

Mechanical testing was carried out with an Instron[®] 5565 universal tester using a 1 kN load cell and pneumatic clamps. The tensile strain was measured by a non-contacting video extensometer (AVE1). A minimum of five specimens was measured, and the average value is reported. *Short filament rods*: filament rods were cut into a length of about 4 cm and tested. The *E-Moduli* were determined at a strain rate of 0.2 mm/min and 0.1% and 0.3% strain. At higher strain, a rate of 10.0 mm/min was applied until fracture of the sample. *Compression-molded films*: the copolymers were melted and compression molded at 220 °C in a Carver 2518 hot press into films with a thickness of about 1.0 mm. The layer thickness was measured with a digital micrometer (Mitutoyo[®] 293-831, digimatic MDC Lite). Specimens for mechanical testing were punched from hot-pressed films into a dogbone geometry (Coesfeld Materialtest Inc., shape according to DIN 54504 S3A). *E-Moduli* were determined at a strain rate of 0.2 mm/min and

between 0.1% and 0.3% strain. At higher strain, a rate of 10.0 mm/min was applied until the fracture of the sample. *3D printed parts*: Five test specimens with the angle of 90° and five of 0° to the layer deposition direction (X- and Y axis) were punched out from each sidewall of the 3D printed square tube. The *E*-Moduli were determined at a strain rate of 0.2 mm/min and 0.1% and 0.3% strain. At higher strain, now a rate of 2.0 mm/min was applied for 90° specimens and 10.0 mm/min for the 0° specimens.

2.8. Shape memory testing

Shape memory experiments were conducted on 3D printed parts in form of a U-shape and a self-biting snake. A 3D digital model was designed (Autodesk® Fusion 360) and additionally sliced (Slic3r Version 1.3.0) into digital layers and printed under the optimized conditions Table S1. The original printed shape was first heated in an oven (Heraeus) at 60 °C for about 5 min to completely melt the PEG segments. At this elastic state, the shape was transferred into the temporary shape and then cooled down in a refrigerator to about 5 °C for the fixation of the temporary shape. The obtained temporary shape was long-term stable under ambient conditions. For recovery, the temporary shape was converted into the recovered shape by short-time heating at 60 °C above $T_{\text{trans.}(low)}$.

3. Results and discussion

3.1. Synthesis and thermal characterization of $(AB)_n$ segmented copolyetherimides

To provide materials for extrusion-based 3D printing with the additional feature of a shape memory effect, the polymer requires two separated transitions at different temperatures, $T_{\text{trans.}(low)}$ and $T_{\text{trans.}(high)}$. In this respect, the $(AB)_n$ segmented copolyetherimides **1a** and **1b** (**Figure 1**) consist of polyethylene glycol segments which crystallize above room temperature and of perylene bisimides segments which form physical crosslinks via π - π interactions at higher temperatures. The copolyetherimides **1a** and **1b** were synthesized in the one-pot-melt polycondensation reaction of perylene-3,4,9,10-tetracarboxylic dianhydride with polyethylene glycol diamines of different length.

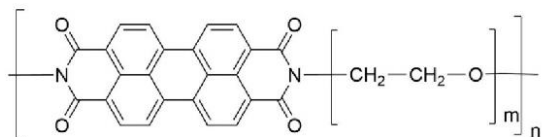
**1a, 1b**

Figure 1: Chemical structure of synthesized $(AB)_n$ segmented copolyetherimides **1a** and **1b** with rigid perylene bisimide segments and flexible polyethylene glycol (PEG) segments (**1a**: $m = 45$ (2000 g/mol), **1b**: $m = 182$ (8000 g/mol)).

To determine the transition temperatures of copolyetherimides they were investigated by thermal and rheological methods. In **Figure 2**, 2nd heating and cooling curves of **1a** and **1b** by DSC measurements are depicted. Both curves show one endothermic transition between 40 and 60 °C indicating the melting of the crystallized PEG segments. Polymer **1a** with the shorter PEG segment (2000 g/mol) exhibits a melting peak at 43 °C with a melting enthalpy of 68 J/g. In **1b** with longer PEG segments (8000 g/mol), the crystallization is more pronounced. Here, a melting range at 57 °C with almost a doubled melt enthalpy of about 120 J/g is measured. Both polymers show recrystallization of the PEG segments with supercooling of 11K for **1a** and at

36K for **1b**. However, from the DSC measurements of **1a** and **1b** the formation of physical crosslinks by the perylene bisimide units cannot be identified at temperatures up to 220 °C. In addition, TGA measurements were carried out for **1a** and **1b** under nitrogen (*Supporting Information*, S1). In both samples weight loss occurs above 370 °C, hence significantly higher than typically temperatures of around 200 °C used for extrusion-based AM.

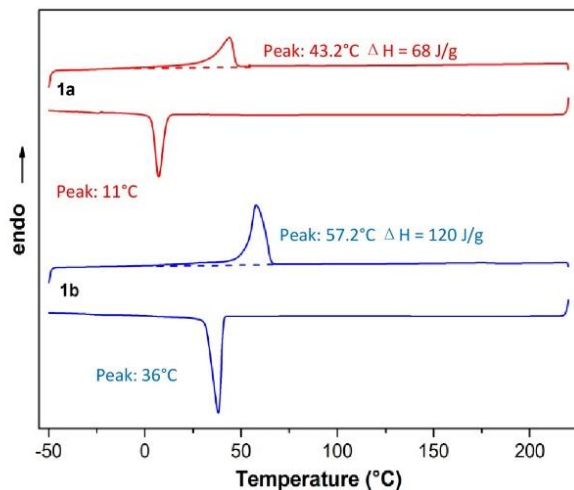


Figure 2: DSC second heating and cooling curves (rate: 10K/min) of the $(AB)_n$ segmented copolyetherimides **1a** and **1b** with corresponding melting temperatures and enthalpies and recrystallization temperatures of the polyethylene glycol segments.

Additionally, oscillator shear rheological measurements as a function of the temperature were performed (**Figure 3**) to investigate the formation of physical crosslinks by the perylene bisimide units. In Figure 3(A) and (B), the storage G' (solid symbols) and the loss modulus G'' (open symbols) as a function of the temperature of **1a** and **1b** are shown. While the storage modulus G' relates to the elastic component of the system, the loss modulus G'' to the viscous component.

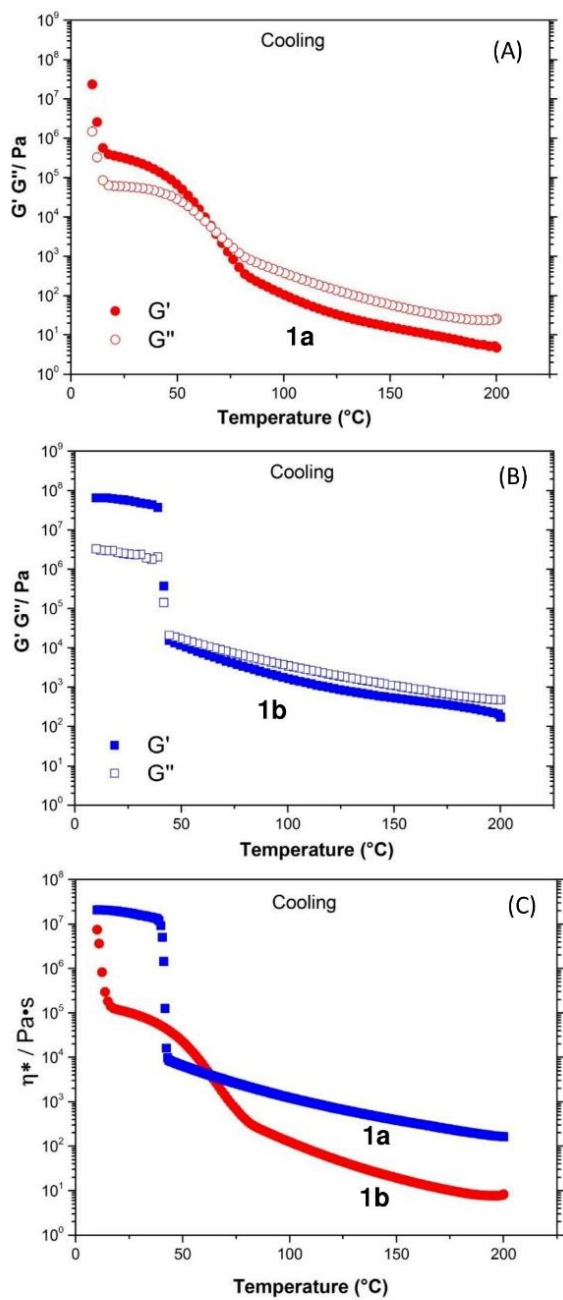


Figure 3: Oscillatory shear rheology measurements of the $(AB)_n$ segmented copolyetherimides. Storage modulus G' and loss modulus G'' of **1a** (A) and **1b** (B), and melt viscosity (C) of **1a** and **1b** as a function of the temperature (Plate-plate 25 mm, 0.5 Hz, cooling with 2K/min).

Consequently, if the loss modulus G'' is larger than the storage modulus G' the polymer exhibits the character of a viscous fluid. The crossing of both moduli is referred to the crossover temperature at which the viscous behavior changes to elastic behavior.^[30] For **1a**, this crossover temperature is at 65 °C, corresponding to the self-assembly of the perylene segments forming physical crosslinks. Figure 3(C) depicts the corresponding curves of **1b**, which contains much longer PEG segments. Here no crossover temperature is identified up the crystallization of the PEG segments. This can be explained by the more diluted perylene segment content of **1b** (PEG 8000) with a similar number of repeating units compared with **1a** (PEG 2000). For samples **1a** and **1b**, the storage and loss moduli rapidly increases at 10 and 45 °C, which is attributed to the progressive crystallization of the PEG segments which is in excellent agreement with the DSC measurements (see Figure 2). In Figure 3(C) the complex melt viscosity plots of **1a** and **1b** upon cooling are shown. Here both copolyetherimides **1a** and **1b** exhibit a low melt viscosity above 150 °C which should facilitate extrusion-based 3D printing. In contrary to **1b**, **1a** exhibits a pronounced transition at around 50-70 °C which is assigned to the disassembly of the perylene bisimide segments ($T_{\text{trans,(high)}}$). For both **1a** and **1b**, a steep increase in viscosity is observed around 10 and 40 °C, respectively, corresponding well with the recrystallization temperatures of the PEG segments as measured by DSC ($T_{\text{trans,(low)}}$). In conclusion, rheology investigations indicate that extrusion-based 3D printing should be possible in the temperature range between 150 and 200 °C since a low viscous melt is present for both copolyetherimides.

3.2. 3D printing of $(AB)_n$ segmented copolyetherimides

3.2.1. Introduction

Figure 4 illustrates the different stages of the extrusion-based AM process. Included are also the different states of the macromolecular arrangement of investigated copolyetherimides during is process. First, the filament has to be fed into the liquefier with driving wheels. Here the filament requires a sufficient stiffness to avoid buckling and slipping between the driving wheels. This is one of the most important factors for a controlled feeding process. In this work, the essential mechanical stability/stiffness of the filaments is provided by the aggregated perylene bisimides and the crystallized PEG segments (I).

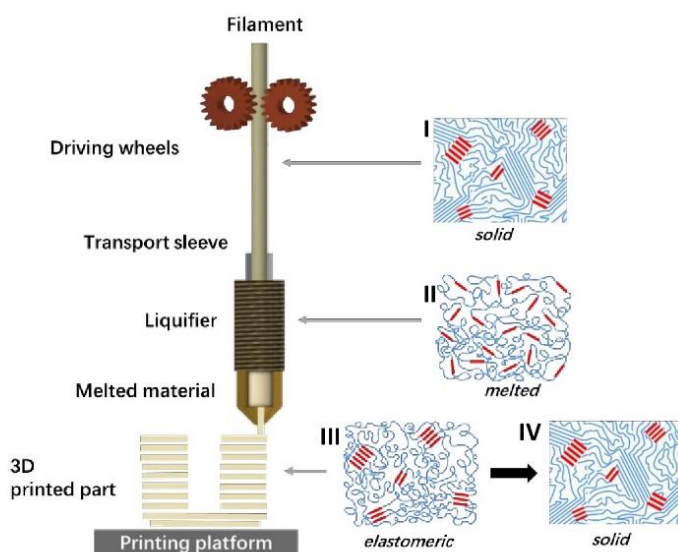


Figure 4: Schematic representation of extrusion-based additive manufacturing process and the different stages of the macromolecular arrangement (I-IV, see main text) of investigated copolyetherimides within filament feeding system (solid), liquefier (melt), and after 3D printing of the printed part (elastomeric and solid).

Then, the liquefier temperature has to be above the melting temperature of the PEG segments and the transition from the assembled to disassemble state of perylene bisimides segments (II), so that an extrudable melt is obtained. After extrusion through the nozzle, the polymer melt is deposited layer by layer to build up a 3D printed part. Upon cooling, the perylene bisimide

segments reassembled and form the first bonding between the layers and stabilize at this point the printed part (III). The layer bonding is further improved by the crystallization of PEG segments (IV). As outlined above in the previous chapters, the synthesized copolymers **1a** and **1b** possess the required thermal transitions and thermoplastic behavior for 3D printing process. As mentioned above, for an efficient transport through the driving wheels and the feeding zone, the polymers require a certain filament strength and stiffness. Therefore, tensile tests of injection-molded filament rods were carried out and compared to compression molded films.

3.2.2. Mechanical characterization by tensile tests

Stress-strain curves of injection-molded filament rods of **1a** and **1b** are shown in **Figure 5** and the obtained data are listed in **Table 1**. The stress-strain curves shown are one representative example of the actually tested ten different specimens.

Table 1: *E*-modulus (E), stress at break (σ_{br}), and elongation at break (ε_{br}) of injection-molded filament rods of $(AB)_n$ segmented copolyetherimides **1a** and **1b**.

Copolymer	E [MPa]	σ_{br} [MPa]	ε_{br} [%]
1a	454 (98) ^{a)}	3.8 (0.1)	1.5 (0.2)
1b	688 (108)	16.0 (0.3)	700 (50)

^{a)} Standard deviation in parentheses of at least ten samples. Experimental details can be found in the Experimental Part.

The behavior of copolyetherimides **1a** is described by an extremely brittle character with an elongation at break of only 1.5% and a strength at break of 3.8 MPa in combination with an E -modulus of 450 MPa. Thus, at room temperature, **1a** lost any elastomer properties. In contrary, copolyetherimide **1b** shows a mechanical behavior of a typical semi-crystalline polymer with a yield point, strain hardening, and ultimate strength. In **1b**, packing and crystallization of the

longer PEG segments are improved and the E-Modulus is higher at about 690 MPa. The E-Moduli of **1a** and **1b** provide sufficient stiffness required for feeding in extrusion-based 3D printers.

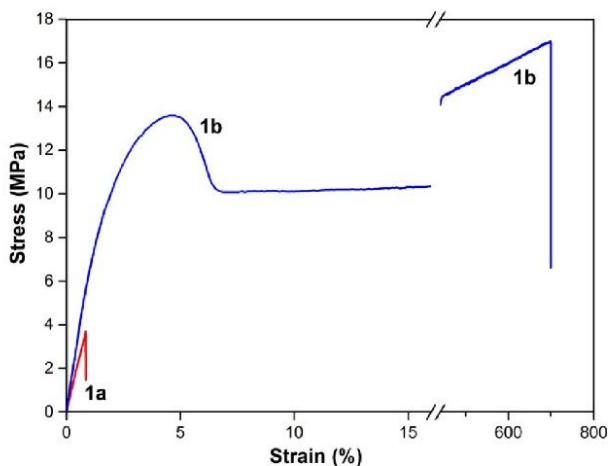


Figure 5: Stress-strain curves of injection-molded filament rods of $(AB)_n$ segmented copolyetherimides **1a** (red) and **1b** (blue). Due to the relatively short PEG 2000 segments of **1a**, it exhibits an much more brittle behavior compared to **1b** possessing PEG 8000 segments.

3.3.3. 3D printing

The final dimensions of injecting-molded filament rods are controlled by the Teflon[®] tube inner diameter and the length of the mold. To prepare much longer pieces of one filament rod, several rods were welded together by pushing two heated ends inside of a short piece of the Teflon[®] tube. More details about this process are included in the *Supporting Information, S2*. To achieve dimensional stable and defect-free 3D printed parts, processing parameters, such as liquefier and printing platform temperature, as well as cooling fan speed, have to be optimized for each polymer. Therefore, copolyetherimides **1a** and **1b** were printed first into small square tubes, these tubes were analyzed, parameters changed, and thus printing variables optimized (see *Supporting Information, S4*). Utilizing these optimized printing parameters, **1a** and **1b** could be

successfully 3D printed to U- or spiral shapes. The extruded material flow was very constant during the printing process and the first printed layer adhered well on the blue tape 3D printing platform. The good quality of the printed square tubes assured reproducible mechanical testing results. **Figure 6(A)** demonstrates the low surface roughness and geometric deformation of a square tube using **1b**.

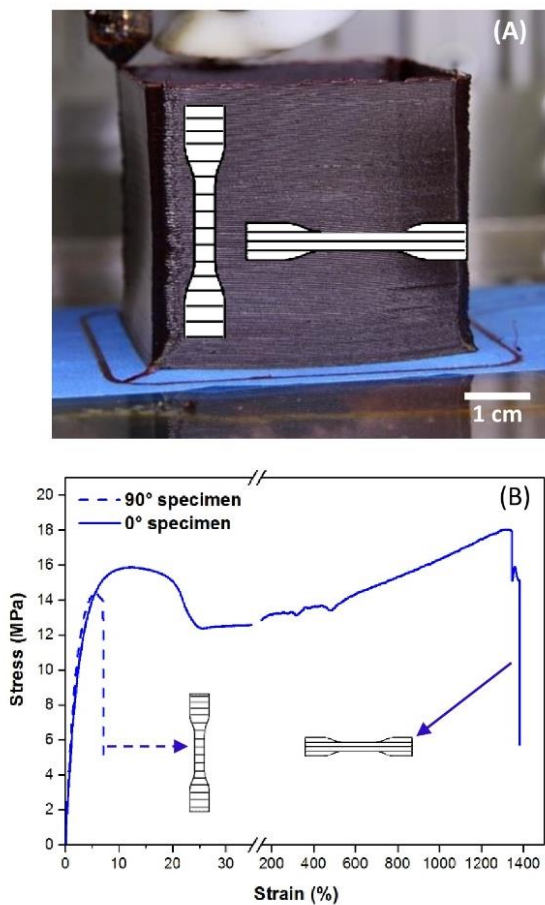


Figure 6: (A) Image of a square tube obtained by extrusion-based 3D printing at 170 °C utilizing copolymer **1b**. Dogbones shown are not at scale. (B) Stress-strain curves of 90° and 0° test specimens punched out of sidewalls of a printed square tube with different orientation to the layer deposition direction. Samples, punched in printing direction (0°), exhibit a tensile behavior with necking and strain hardening, whereas samples punched in 90° direction are much weaker and reflect the interlayer bonding strength.

Due to the square tube shape, tensile specimens of different orientations to the layer deposition direction can be punched out of the sidewalls and characterized by tensile tests. For example, stress-strain curves of **1b** are plotted in **Figure 6(B)**. Here, the 0° specimen, which should be more similar to the properties of an extruded and injection-molded material, features a very high elongation at break of about 1400% and is therefore comparable with the tensile data measured of injection-molded filament rods (see Table 1). But more interesting is the elongation at break of the 90° -specimens reflecting the interlayer bonding strength of printed parts. The value of 7.2% and the yield strength of 14 MPa can be considered a typical value for semi-crystalline polymers utilized for 3D printing.

Table 2: Comparison of the mechanical properties of 3D printed parts to compression-molded films of copolyetherimide **1b**.

<i>Sample</i>	<i>E</i> [MPa] ^{a)}	σ_{br} [MPa] ^{b)}	ϵ_{br} [%] ^{c)}
3D printed part 90° ^{d)}	644 (54) ^{e)}	14.4 (0.2)	7.2 (0.2)
3D printed part 0° ^{d)}	659 (66)	18.2 (0.2)	1400 (60)
Compression molded film ^{f)}	613 (51)	12.5 (0.3)	35 (0.5)
Injection molded rod ^{g)}	688 (108)	16.0 (0.3)	700 (50)

^{a)} E-modulus; ^{b)} strength at break; ^{c)} elongation at break; ^{d)} orientation of tensile loading direction to layer deposition direction of punched dogbones from 3D printed square tube; ^{e)} standard deviation in parentheses of at least ten samples.; ^{f)} dogbones were punched out from a compression-molded film; ^{g)} see Table 1. Experimental details can be found in the Experimental Part.

In **Table 2**, tensile properties of copolymer **1b** investigated on injection-molded filament rods, dogbones punched out of compression-molded films, and dogbones punched out of 3D printed square tube sidewalls are listed. The E-moduli of tensile specimens obtained by different methods range between 610 and 688 MPa and thus are comparable.

3.4 4D printing

The 4D printing concept is illustrated in **Figure 7** by realizing a shape memory utilizing the phase transitions of the presented $(AB)_n$ segmented copolyetherimides. First, an original U-shape is 3D printed consisting at room temperature of crystallized PEG and aggregated perylene bisimide segments. When the original shape is heated above $T_{\text{trans.}(low)}$, the polymer softens (1. Softening) owed to the melting of the PEG segments. In this state, the U-shape can be transformed by an external force into the temporary shape (2. External force), for example, a V-shape. As at $T_{\text{trans.}(low)}$ the melted PEG segments are chemically attached to the aggregated perylene bisimide segments, an elastomeric behavior is present. Thus, after cooling below $T_{\text{trans.}(low)}$, the temporary shape is fixed (3. Fixation) and offers long-term shape stability under ambient conditions. Heated again above $T_{\text{trans.}(low)}$ softens the polymer (4. Softening) and allows the recovery driven by elastomeric restoring forces (5. Shape recovery). The recovered shape then can again be fixed by cooling below $T_{\text{trans.}(low)}$ (6. Fixation).

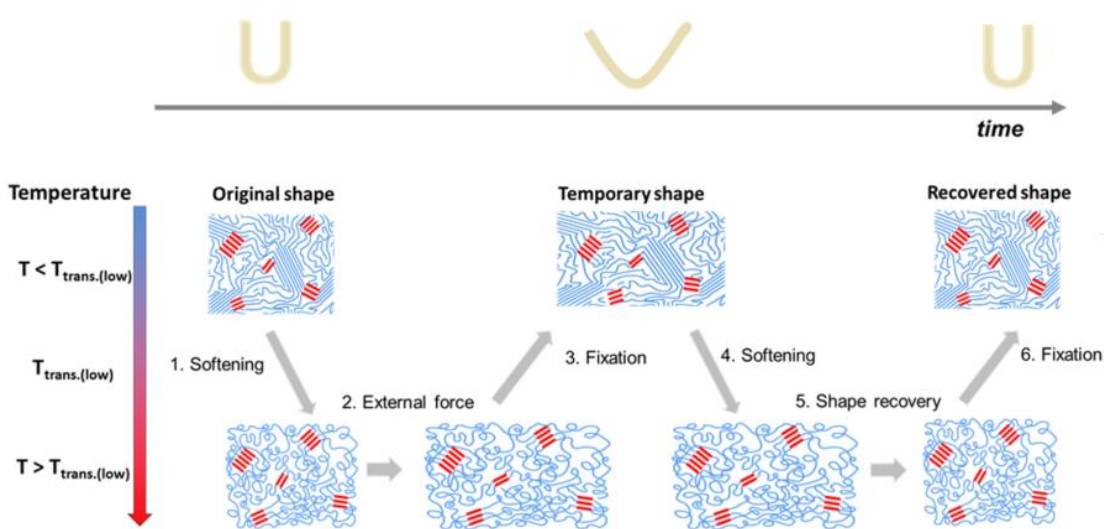


Figure 7: Schematic illustration of phase transitions of utilized copolyetherimides when realizing the shape memory effect of a 3D printed part.

3.4.1. Blend of copolyetherimides

For the realization of a shape memory effect utilizing a thermoplastic polymer, two thermal transition temperatures are needed. The lower thermal transition, $T_{\text{trans.}(low)}$, should be clearly above room temperature, so a fixation of a temporary shape is possible. The second thermal transition, $T_{\text{trans.}(high)}$, should be at a distinct higher temperature, so the physical crosslinks are sufficiently stable at $T_{\text{trans.}(low)}$. But DSC curves of copolyimides **1a** and **1b** (see Figure 2) exhibit only one thermal transition at around 40 and 60 °C, respectively, which are attributed to the melting of the PEG crystals. No indication for an aggregation of rigid perylene bisimide segments can be identified. However, rheological investigations (see Figure 3) show a crossover for **1a** at 65 °C upon cooling ($T_{\text{trans.}(high)}$). In consequence, this crossover may indicate the formation of physical crosslinks by assembled perylene bisimides. For investigating the potential resulting shape stability, short filament rods of **1a** and **1b** were mounted free-standing in a polystyrene foam block (Figure 8(A)).

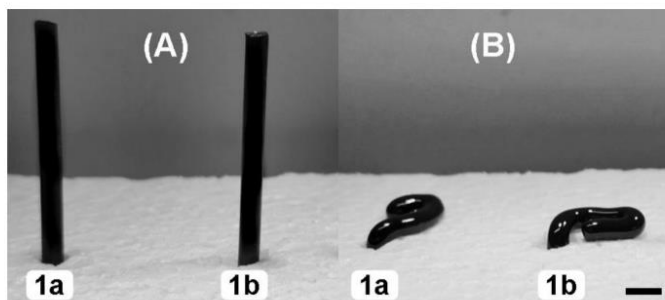


Figure 8: Qualitative experiment to demonstrate the lacking thermal shape stability of filament rods of copolyetherimides **1a** and **1b** at room temperature (A) and after heating to 60 °C for 5 min (B). (The scale bar represents 1 cm).

Then they were placed into an oven at 60 °C (between $T_{\text{trans.}(low)}$ and $T_{\text{trans.}(high)}$) for 5 min. Figure 8(B) shows collapsed filament rods demonstrating that any possibly formed perylene aggregates are too weak to fix the shape of a standing filament rod above $T_{\text{trans.}(low)}$. Therefore, an additional copolyetherimide with a higher perylene bisimide content using Jeffamine® ED-

900 was synthesized. This monomer is based on a much shorter PEG center block of around 550 g/mol, flanked by propylene oxide spacers, does not crystallize, and exhibits a glass temperature around $-50\text{ }^{\circ}\text{C}$.

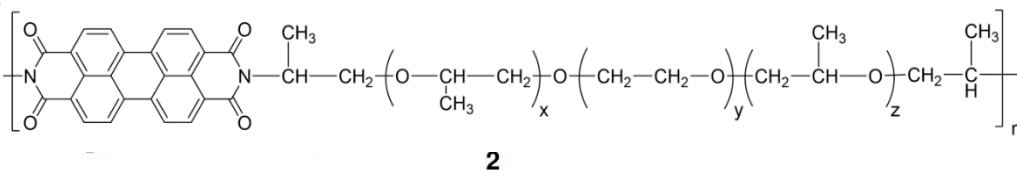


Figure 9: Chemical structure of synthesized $(AB)_n$ segmented copolyetherimide **2** with perylene bisimide and Jeffamine[®] ED-900 segments. According to the datasheet of Jeffamine[®] ED-900, y amounts to 12.5, whereas $x+z$ to around 6.^[39]

The much shorter Jeffamine block and the propylene oxide spacers might improve the aggregation of perylene bisimide segments. Here, the same bulk synthesis route was used yielding copolyetherimide **2** (Support Information, S5). Thermal characterization of copolyetherimide **2** using DSC showed as expected no melting peak for the Jeffamine[®] segments, but a small peak around $200\text{ }^{\circ}\text{C}$ (Figure S6). Oscillating shear rheology revealed a very strong increase in shear modulus of approx. six magnitudes within less than 10K around $180\text{ }^{\circ}\text{C}$ during cooling as shown in **Figure 10**. This reversible transition can be assigned unambiguously to the assembly of the perylene bisimide moieties in the polymer since no other transition can occur at this temperature.

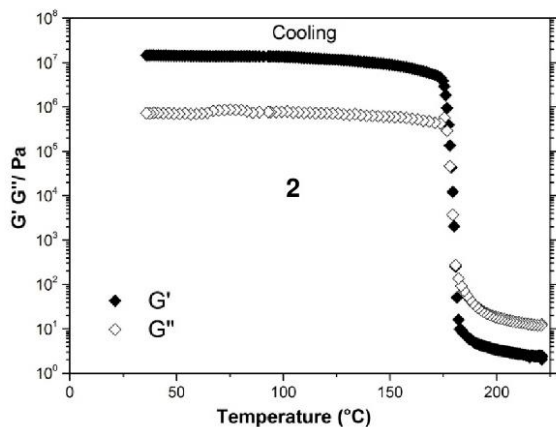


Figure 10: Oscillatory shear experiments of copolyetherimide **2** based on Jeffamine[®] ED900 showing a steep increase of shear modulus between 185 and 175 °C caused by the aggregation of the perylene bisimide hard segments. T_{cross} is observed at 180°C. (Cooling at 2K/min, 25 mm plate-plate, 0.5 Hz).

Thus, this ultra-fast hardening behavior is based solely on π - π interactions of the perylene imides moieties.

In summary, copolyetherimides **1a** and **1b** show a PEG crystallization but no perylene bisimide hard segment disaggregation, whereas **2** based on Jeffamine[®] exhibits no PEG crystallization but strong perylene bisimide hard segment melting transition. Hence, a blend of the two copolyetherimides should combine both properties. **Figure 11** shows the mechanical characterization of filament rods produced from **1b**, **2**, and blend **3**. The stress-strain curve of **1b** shows a typical thermoplastic behavior with high elongation at break of about 700%. While **2** shows a clearly lower E-modulus and an elongation at break of 8%. However, the E-modulus of **3** is in-between, and its elongation at break is reduced to 6%. Tensile tests of compression-molded and punched out dogbones of **1b**, **2**, and **3** show similar stress-strain curves compared to filament rods (more details see *Supporting Information, S5 and Figure S8*).

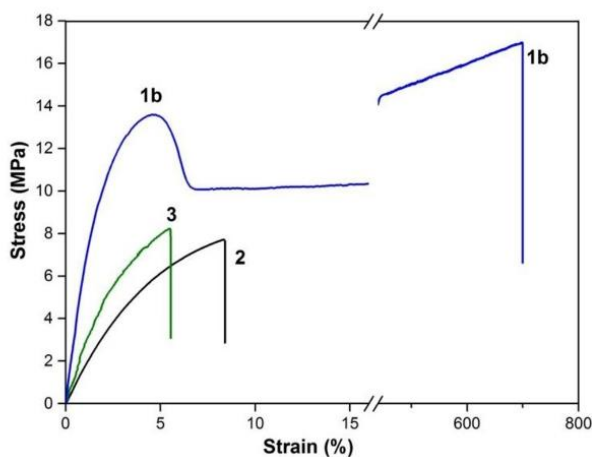


Figure 11: Stress-strain curves of filament rods of copolyetherimides **1b**, **2**, and blend **3**.

As **1b** showed excellent 3D printing performance and mechanical properties, a blend of **1b** and **2** was prepared in a 1:1 ratio (denoted as **3**) and processed to filament rods. By heating filament rods of **2** and blend **3** at $T_{\text{trans.}(low)}$ for 5 min both filament rods kept their original shape (**Figure 12**) due to aggregated perylene bisimide segments.

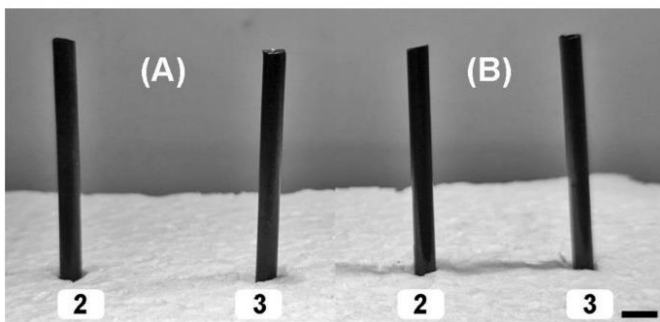


Figure 12: Demonstration of the thermal shape stability of the filament rods of copolyetherimide **2** and blend **3** at room temperature (A) and after heating at 60 °C for 5 min (B). The aggregated perylene bisimide segments are responsible for the shape stability, even at 60 °C. (The scale bar represents 1 cm).

Figure 13(A) shows the oscillating shear rheology measurements of storage modulus G' and loss modulus G'' of blend **3**. Two thermal transitions at about 40 °C and 180 °C are observable as a step-like moduli increases. The increase at the lower temperature results from the crystallization of PEG segments, and the increase at the higher temperature with a crossover of G' and G'' at 183 °C is caused by formed perylene bisimide aggregates.

In **Figure 13(B)**, the complex melt viscosities of all three materials are plotted as a function of the temperature. The melt viscosity, again, is important for 3D printing since a too high viscosity impedes the printing process. In blend **3**, an increase in viscosity is observed at around 180 °C, superimposing with the strong transition of **2** in this region. As expected, the blend viscosity increase is less pronounced compared to **2** and turns into a plateau with a slight slope. The viscosity curves show in the case of **1b** the crystallization of PEG segments at low temperatures of around 40 °C, in the case of **2** the aggregation of perylene bisimide hard

segments at higher temperatures (180 °C), and in the case of the blend **3** a combination of both, thus now featuring a low and a high thermal transition, $T_{\text{trans.}(low)}$ and $T_{\text{trans.}(high)}$ (see also thermal characterization by DSC *Supporting Information S6*). The two transitions are at around 40 °C and 180 °C and should allow 3D printing above $T_{\text{trans.}(high)}$ and 4D printing slightly above $T_{\text{trans.}(low)}$.

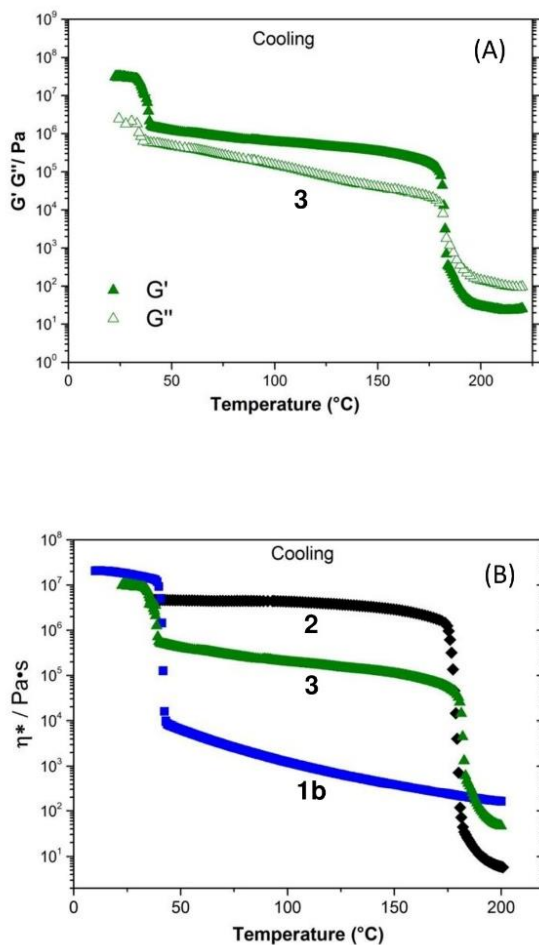


Figure 13: Oscillatory shear rheology measurements upon cooling (A) of copolyetherimides blend **3**. T_{cross} in blend **3** is at 183 °C. In (B), the complex viscosity as a function of the temperature is plotted for the blend components **1b** and **2**, as well as for blend **3** itself.

Also very important, each thermal transition is observed as a clear change in viscosity within a narrow temperature range. In summary, the copolyetherimide blend **3** demonstrates the material properties combination of **1b** and **2**, in combination with relatively low melt viscosities, and thus should enable 4D printing.

3.4.2. 4D printing utilizing blend 3

For demonstrating 4D printing, a ring-shaped self-biting snake was 3D printed in its original shape using blend **3** (**Figure 14** (A), see also *Supporting Information*, S7). As mentioned above, $T_{\text{trans.}(low)}$ was determined at around 40 °C; the temperature of 60 °C was selected for shape transformation as at this temperature crystallized PEG segments are entirely melted. After heating at 60 °C for 5 min in an oven, the ring-shaped snake was transferred into the temporary shape, an open snake, and in this shape cooled down in a refrigerator to about 5 °C (**Figure 14** (B)).



Figure 14: Demonstration of shape memory effect of a 3D printed self-biting snake. The 3D printed material is the blend **3** of copolymers **1b** and **2** in a 1:1 ratio. (A) shows the original shape of the 3D printed object, (B) in the temporary shape after heating at 60 °C and cooling at 5 °C, and (C) the recovered shape after reheating at 60 °C.

By keeping the oven temperature below $T_{\text{trans.}(high)}$ (180 °C) and due to the physical crosslinks of perylene bisimide segments, the achieved elastic deformation was fixed as open ring-shaped

snake by the crystallization of the PEG segments of **1b**. When the temporary shape is reheated at 60 °C for 3 min, the crystallized PEG segments are molten again, the stored elastic energy is released, and the original shape recovered (**Figure 14 (C)**). The printed self-breaking snake shows a resetting of the deformation to its original shape.

4. Conclusion

3D and also 4D printing utilizing tailored $(AB)_n$ segmented copolyetherimides and a blend thereof is demonstrated. The copolyetherimides consist of perylene bisimide and poly(ethylene glycol) (PEG) segments. At room temperature, the crystallized PEG segments stiffen efficiently the injection-molded filament rods and thus facilitate filament feeding utilizing a standard extrusion-based 3D printer. The necessary feature of two thermal transitions at significantly different temperatures for the realization of 4D printing was achieved by blending to different copolyetherimides. The thermoplastic behavior of this blend allowed successful 3D printing at 210 °C, and the achieved two thermal transition temperatures, $T_{\text{trans.}(low)}$ and $T_{\text{trans.}(high)}$, enabled 4D printing. Here, the reversible melting and crystallization of the PEG segments at above and below $T_{\text{trans.}(low)}$ allowed 4D shape memory programming and shape recovering, as at this low temperature the perylene bisimide units are still aggregated and cause an elastic behavior. The presented results demonstrate that tailored $(AB)_n$ segmented copolyetherimides combine good 3D printing performances with low warp deformation, excellent interlayer bonding strength, and the ability of a shape memory effect.

Supporting Information

Supporting Information is available from the Wiley Online Library or from the author.

Acknowledgments

The PEG diamines were kindly synthesized by Sandra Ganzleben and Jutta Failner from the Chair of Macromolecular Chemistry I, University of Bayreuth, Germany.

References

- [1] A. Bagsik, V. Schöppner, and E. Klemp, *14th international scientific conference on polymeric materials* **2010**.
- [2] P. Dudek, *Archives of Metallurgy and Materials* **2013**, 58.
- [3] S. H. Masood, K. Mau, and W. Q. Song, *Materials Science Forum* **2010**, 654-656, 2556.
- [4] S.-H. Ahn, M. Montero, D. Odell, S. Roundy, and P. K. Wright, *Rapid Prototyping Journal* **2002**, 8, 248.
- [5] Q. Sun, G. M. Rizvi, C. T. Bellehumeur, and P. Gu, *Rapid Prototyping Journal* **2008**, 14, 72.
- [6] T.-M. Wang, J.-T. Xi, and Y. Jin, *Int. J. Adv. Manuf. Technol.* **2007**, 33, 1087.
- [7] M. Spoerk, C. Holzer, and J. Gonzalez-Gutierrez, *J. Appl. Polym. Sci.* **2020**, 137, 48545.
- [8] M. Spoerk, J. Sapkota, G. Weingrill, T. Fischinger, F. Arbeiter, and C. Holzer, *Macromol. Mater. Eng.* **2017**, 12, 1700143.
- [9] O. S. Carneiro, A. F. Silva, and R. Gomes, *Materials & Design* **2015**, 83, 768.
- [10] S. Hertle, M. Drexler, and D. Drummer, *Macromol. Mater. Eng.* **2016**, 301, 1482.
- [11] J. Z. Jinneng Xie. *CN 201410332650*, **2014**.
- [12] M. Jin, R. Giesa, C. Neuber, and H.-W. Schmidt, *Macromol. Mater. Eng.* **2018**, 303, 1800507.
- [13] M. Jin, C. Neuber, and H.-W. Schmidt, *Additive Manufacturing* **2020**, 33, 101101.
- [14] C. G. Schirmeister, T. Hees, E. H. Licht, and R. Mülhaupt, *Additive Manufacturing* **2019**, 28, 152.
- [15] M. Spoerk, F. Arbeiter, I. Raguž, G. Weingrill, T. Fischinger, G. Traxler, S. Schuschnigg, L. Cardon, and C. Holzer, *Macromol. Mater. Eng.* **2018**, 303, 1800179.
- [16] Z. X. Khoo, J. E. M. Teoh, Y. Liu, C. K. Chua, S. Yang, J. An, K. F. Leong, and W. Y. Yeong, *Virtual and Physical Prototyping* **2015**, 10, 103.
- [17] M. D. Monzón, R. Paz, E. Pei, F. Ortega, L. A. Suárez, Z. Ortega, M. E. Alemán, T. Plucinski, and N. Clow, *Int. J. Adv. Manuf. Technol.* **2017**, 89, 1827.
- [18] S. K. Leist and J. Zhou, *Virtual and Physical Prototyping* **2016**, 11, 249.
- [19] F. Momeni, S. M. Mehdi Hassani, N. X. Liu, and J. Ni, *Materials & Design* **2017**, 122, 42.

- [20] J. Choi, O.-C. Kwon, W. Jo, H. J. Lee, and M.-W. Moon, *3D Printing and Additive Manufacturing* **2015**, 2, 159.
- [21] C. M. González-Henríquez, M. A. Sarabia-Vallejos, and J. Rodríguez-Hernández, *Progress in Polymer Science* **2019**, 94, 57.
- [22] A. S. Gladman, E. A. Matsumoto, R. G. Nuzzo, L. Mahadevan, and J. A. Lewis, *Nat. Mater.* **2016**, 15, 413.
- [23] Q. Ge, A. H. Sakhaei, H. Lee, C. K. Dunn, N. X. Fang, and M. L. Dunn, *Sci. Rep.* **2016**, 6, 31110.
- [24] M. D. Hager, S. Bode, C. Weber, and U. S. Schubert, *Progress in Polymer Science* **2015**, 49-50, 3.
- [25] A. Lendlein and R. Langer, *Science (New York, N.Y.)* **2002**, 296, 1673.
- [26] J. Leng, X. Lan, Y. Liu, and S. Du, *Progress in Materials Science* **2011**, 56, 1077.
- [27] C. Liu, H. Qin, and P. T. Mather, *J. Mater. Chem.* **2007**, 17, 1543.
- [28] Tobushi Hisaaki, S. Hayashi, and S. Kojima, *JSME international journal. Ser. 1, Solid mechanics, strength of materials* **1992**, 35, 296.
- [29] D. Ratna and J. Karger-Kocsis, *J. Mater. Sci.* **2008**, 43, 254.
- [30] G. Hochleitner, E. Fürsattel, R. Giesa, J. Groll, H.-W. Schmidt, and P. D. Dalton, *Macromolecular rapid communications* **2018**, 39, e1800055.
- [31] Elkins K., Nordby K., Janak C., Gray IV R. W., Bohn J. H., and D. G. Baird. *1997 International Solid Freeform Fabrication Symposium*, **1997**.
- [32] G. Hernández, N. Casado, A. M. Zamarayeva, J. K. Duey, M. Armand, A. C. Arias, and D. Mecerreyes, *ACS Appl. Energy Mater.* **2018**, 1, 7199.
- [33] Z. Liang, R. A. Cormier, A. M. Nardes, and B. A. Gregg, *Synthetic Metals* **2011**, 161, 1014.
- [34] Z. Liang, R. A. Cormier, A. M. Nardes, and B. A. Gregg, *MRS Proceedings* **2011**, 1286.
- [35] E. Rostami-Tapeh-Esmail, M. Golshan, M. Salami-Kalajahi, and H. Roghani-Mamaqani, *Dyes and Pigments* **2020**, 108488.
- [36] T. Sakurai, N. Orito, S. Nagano, K. Kato, M. Takata, and S. Seki, *Mater. Chem. Front.* **2018**, 2, 718.
- [37] C. Liu, J. Yuan, X. Luo, M. Chen, Z. Chen, Y. Zhao, and X. Li, *Mol. Pharm.* **2014**, 11, 4258.
- [38] M. Iijima, D. Ulkoski, S. Sakuma, D. Matsukuma, N. Nishiyama, H. Otsuka, and C. Scholz, *Polym. Int.* **2016**, 65, 1132.
- [39] Huntsman Corporation, JEFFAMINE® ED-900 Polyetheramine, <https://www.sigmaaldrich.com/catalog/product/aldrich/14527?lang=de®ion=DE>, accessed: June 2020.

Supporting Information:

(AB)_n segmented copolyetherimides for 4D printing

Minde Jin, Markus Stihl, Reiner Giesa, Christian Neuber*, Hans-Werner Schmidt*

Macromolecular Chemistry and Bavarian Polymer Institute (BPI), University of Bayreuth, Universitätsstraße 30, 95447 Bayreuth, Germany

* E-mail: christian.neuber@uni-bayreuth.de;

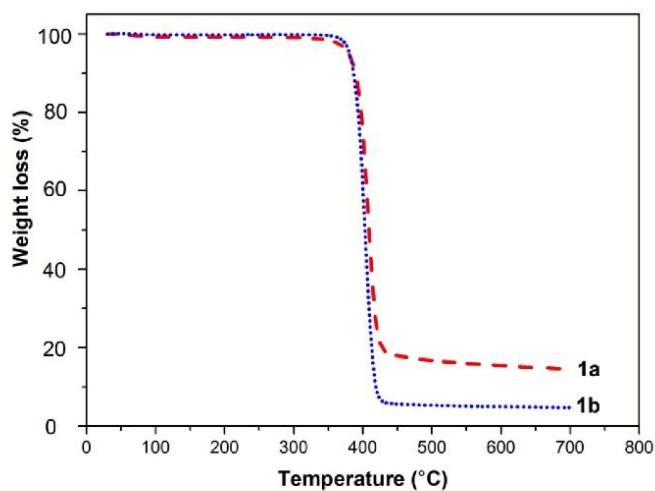
hans-werner.schmidt@uni-bayreuth.de

Table of contents

1. TGA measurements of **1a** and **1b**
2. Injection-molded filament rod welding
3. Filament rod of **1a** and **1b** after tensile testing
4. Optimization of the 3D printing parameters for copolyetherimides **1a**, **1b**, and **2**
5. Preparation and properties of blend **3**
6. 3D printing of blend **3**
7. 4D printing of blend **3** utilizing a U-shape

1. TGA measurements of **1a** and **1b**

Thermal gravimetric analysis (TGA) measurements were performed on a Mettler Toledo TGA/STDA 851e, using a heating rate of 10 K/min from 30 °C to 700 °C under nitrogen atmosphere (20 mL min⁻¹). The polymer samples were placed in an aluminum oxide ceramic crucible. The weight loss was recorded as a function of the temperature. From Figure S1, (AB)_n segmented copolyetherimides **1a** and **1b** exhibit similar thermal decomposition behaviors. The weight loss starts at about 370 °C. The char yield of **1a**, which has a higher perylene bisimide content, is about 14.8% (theoretical 13.4%). As expected, for **1b** with the lower perylene bisimide content, char yield is only at about 4.8% (theoretical 2.8%).



*Figure S1: TGA curves of synthesized (AB)_n segmented copolyetherimides **1a** and **1b**.*

2. Injection-molded filament rod welding

For all copolyetherimides, the barrel temperature of the injection molding unit was set to 230°C to obtain a constant melt flow. The mold temperature was set to 25°C and applied injection/holding pressure was 5 bar for 5 s. The melt was injected into a metal mold containing a Teflon[®] tube (length: 140 mm, outer diameter: 4.0 mm, inner diameter: 3.0 mm). Thus, the final dimension of injection-molded rods is controlled with high precision by the inner tube dimensions. After the injection molding process, the Teflon[®] tube was removed from the mold and a new tube inserted for the next injection cycle (Figure S2, A).

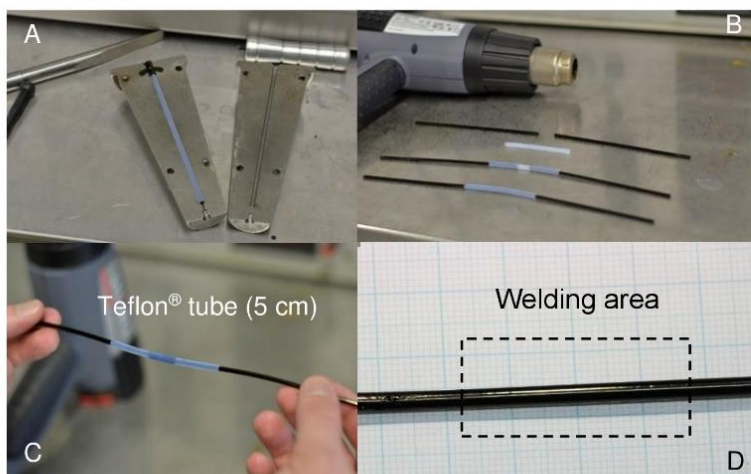


Figure S2: A) Injection-molded filament rod utilizing a Teflon[®] tube as inner mold. B) Joining injection-molded filament rods inside a short Teflon[®] tube. C) Welding two ends of injection-molded filament rod utilizing a heat gun for short-term melting. D) Obtained smooth welding area between two joined filament rods after the detachment of the Teflon[®] tube.

After removing the Teflon[®] tube by cutting, each obtained filament rod is approximately 135 mm to 140 mm long and weighs around 1.0 g. Then, seven injection-molded filament rods were welded together into a filament section with the length of about 90 cm by using a short Teflon[®] tube with

same diameter and a length of about 5 cm as guide. For this purpose, two ends of injection-molded filament rods were pushed together inside the Teflon[®] tube and heated in the contact area with a heat gun for short-term melting (Figure S2, B and C). The obtained welding areas are very smooth, and the Teflon[®] tube could be easily slid to the filament end position for the next welding (Figure S2 (D)).

3. Filament rod of 1a and 1b after tensile testing

Figure S3 shows pictures of failed short filament rods and dog-bones which were originally punched out of compression molded film of **1a** and **1b** after tensile testing. While **1a** shows a smooth surface at the fracture area, **1b** exhibits the properties of a typical tough and ductile semi-crystalline material with very high elongation at break of about 700%.

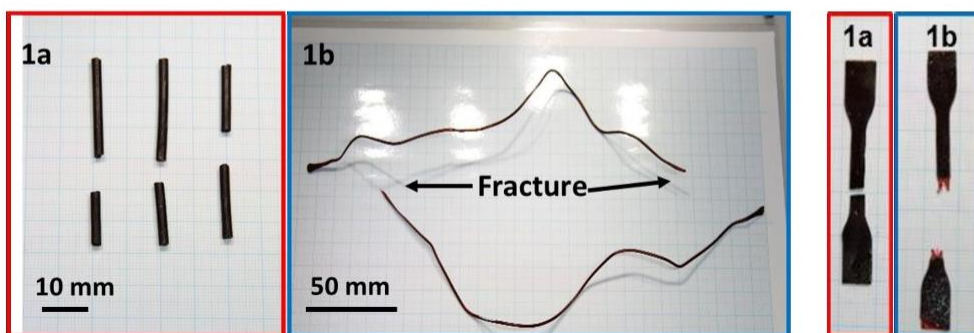


Figure S3: Pictures of failed filament rods and dog-bones of copolyetherimides **1a** and **1b** after tensile testing.

4. Optimization of the 3D printing parameters for copolyetherimides **1a**, **1b**, and **2**

To achieve dimensional stable and defect-free 3D printed parts by extrusion-based 3D printing, processing variables, such as extruder and printing platform temperature, printing and cooling fan speed, have to be optimized for each material. The geometry for this printing optimization was a square tube and the criteria were less warp deformation and smooth part finishing using a qualitative evaluation with the naked eye. By performing a series of printing runs, the most important processing variables were optimized and are summarized in Table S1. Utilizing these optimized printing parameters, **1a** and **1b** could be 3D printed in different shapes (Figure S5), while copolyetherimide **2** could not be used for 3D printing at all.

Table S1: Optimized 3D printing parameters for 1a, 1b, and 2.

<i>3D printing variables/Material</i>	<i>1a</i>	<i>1b</i>	<i>2*</i>
Nozzle temperature (°C)	175	170	n/a
Printing platform temperature (°C)	50	50	n/a
Printing speed (mm/s)	15	15	n/a
Layer height (μm)	250	250	n/a
Fan speed (%)	100	100	n/a
3D printing platform surface	3M blue tape		

*) not available, could not be printed due to poor adhesion to the printing build surface.

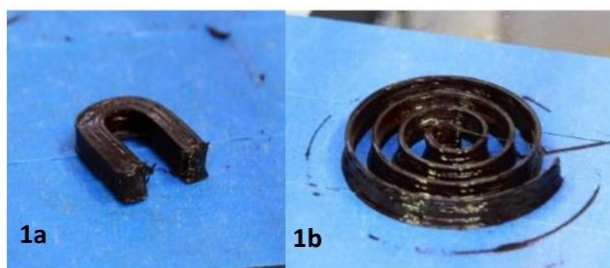


Figure S5: 3D printed objects utilizing optimized printing parameters for 1a or 1b. 1a: 3D printed U-shape; 1b: 3D printed spiral shape.

5. Preparation and properties of blend 3

As neither copolyetherimide **1a** nor **1b** possessed two clear thermal transitions, a blend consisting of **1b** and **2** was prepared, denoted as **3**. A Carver 2518 hot press was used to mix both copolymers by compression molding of the blend **3** film, folding the film, and repeating the compression molding and folding procedure for at least 10 times.

Differential scanning calorimetry (DSC) was conducted using a Mettler Toledo® DSC 2 STARe system under a nitrogen atmosphere from 25 to 250 °C at a heating/cooling rate of 10 K/min. From the second heating and cooling DSC runs of **3**, clear melting and recrystallization peaks at 56 °C and 32 °C of PEG segments of the corresponding blend components are observed (Figure S6). At about 190 °C, melting peaks are detected in **2** and blend **3** which correspond to the disassembly of aggregated perylene bisimide segments. In blend **3**, the melt enthalpy of perylene bisimide segments is about 50% of **2** which agrees with the 1:1 blending ratio.

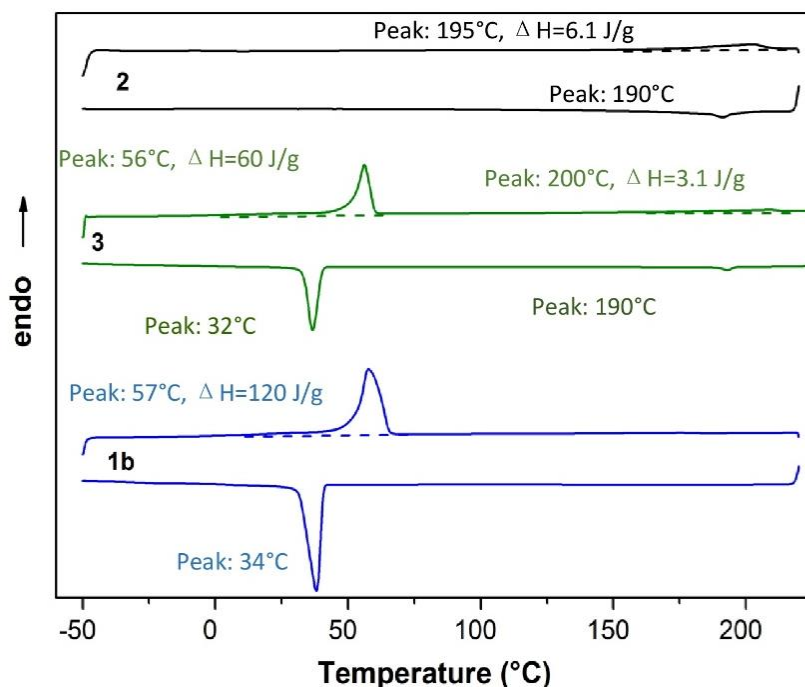


Figure S6: DSC measurement of **2**, blend **3**, and **1b**.

From TGA curves (Figure S7), the char yield of blend **3** (1:1 ratio of **1b** and **2**) is in the middle of the two copolyetherimides **1b** and **2**. The weight loss starts at about 370 °C. The char yield of **1a** with the higher perylene bisimide content is about 18%. For **1b** with a much lower perylene bisimide content, the char yield is about 5%.

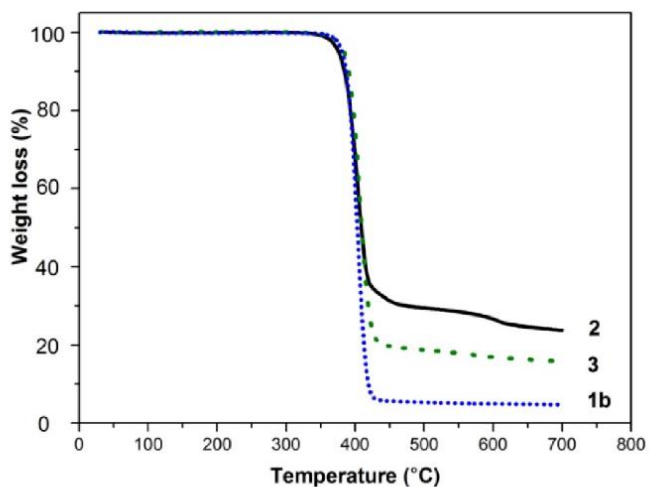


Figure S7: TGA measurement of **1b**, **2**, and blend **3**. Testing conditions are summarized in section S1.

Stress-strain curves of dog bones punched out of compression-molded films (Figure S8) show very similar mechanical behaviors compared with investigation on injection-molded rods (see also Table S2). The measured E-modulus of about 226 MPa for blend **3** should provide enough stiffness needed for a successful feeding into an extrusion-based 3D printers.

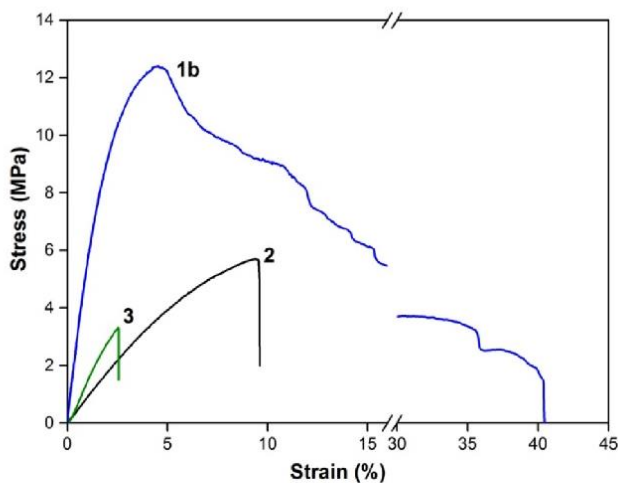


Figure S8: Stress-strain curves of compression-molded film of **1b**, **2**, and blend **3**. Testing conditions are summarized in the main text.

Table S2: Mechanical properties of synthesized copolyetherimides **1b**, **2** and of blend **3** from injection-molded filament rods and dog bones punched out of compression-molded films.

Material	Specimen^{a)}	<i>E</i> [MPa]^{b)}	σ_{br} [MPa]^{c)}	ϵ_{br} [%]^{d)}
1b	Injection-molded rod	688 (108) ^{e)}	16.0 (0.3)	700 (50)
	Compression-molded	613 (51)	12.5 (0.3)	35 (5)
2	Injection-molded rod	85 (8) ^{f)}	6.0 (0.4)	9.7 (0.4)
	Compression-molded	613 (51)	12.5 (0.3)	35 (5)
3	Injection-molded rod	226 (25)	8.5 (0.6)	6.7 (3.2)
	Compression-molded	165 (25) ^{e)}	7.4 (0.2)	8.1 (0.3)

^{a)} Tensile specimen form. Injection-molded rod: filament rod obtained by injection-molding; compression-molded: dog-bone punched out of a compression-molded film; ^{b)} E-modulus; ^{c)} strength at break; ^{d)} elongation at break; ^{e)} standard deviation in parentheses from the data of at least 10 specimens.

6. 3D printing of blend 3

The prepared blend **3** with a 1:1 ratio of **1b** and **2** was successfully 3D printed. For the optimization of 3D printing variables, smaller square tubes were 3D printed (Figure S9 left). The optimized nozzle temperature was identified to 210 °C, which is above $T_{\text{trans.}(high)}$ and the other optimized 3D printing parameters are the same as found for **1a** (see Table S1).

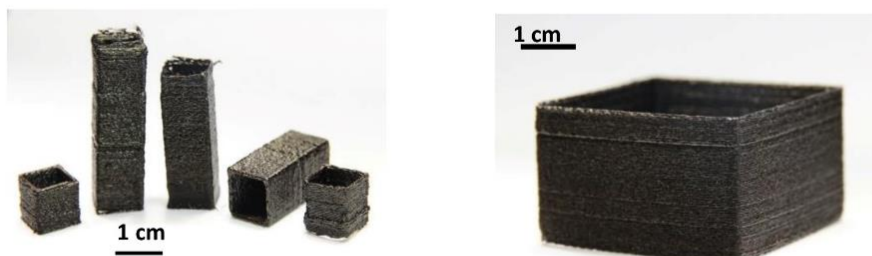


Figure S9: Extrusion-based 3D printed square tubes for optimization of the printing variables (left) and utilizing blend 3(right).

7. 4D printing of blend 3 utilizing a U-shape

To demonstrate 4D printing, a U-shape was 3D printed in its original shape utilizing the copolyetherimide blend 3 (Figure S10). This shape could be transferred into a temporary V-shape slightly above $T_{\text{trans.}(low)}$, then the V-shape fixated by cooling below $T_{\text{trans.}(low)}$, and the U-shape recovered by reheating at slightly above $T_{\text{trans.}(low)}$.



Figure S10: Demonstration of shape memory effect utilizing a 3D printed U-shape of blend 3. Slightly above $T_{\text{trans.}(low)}$ (60 °C), the U-shape could be transferred to the temporary shape, this shape fixed by cooling, and nearly fully recovered by reheating at slightly above $T_{\text{trans.}(low)}$ for a short time period.

Extended summary

Additive manufacturing (AM) opens up a whole new era for digital design and intelligent manufacturing, which will play a vital role in the next industry evolution (industry 4.0). The application and exploration of new polymer materials are the most challenging task for driving this emerging technology to final maturity. In this context, the motivation for this thesis arises from the need for tailor-made materials for additive manufacturing.

Among 3D printing technologies, extrusion-based additive manufacturing, also known as fused deposition modeling (FDM) or fused filament fabrication (FFF), is one of most widely-used processes. Here, a thermoplastic extrusion process in combination with computer-numerical-controlled technology provides a cost-effective layer by layer production of 3D printed parts. There is a demand of a targeted material development for extrusion-based 3D printing. In this context, the thesis covers (i) an efficient material screening method for the development and testing of polymers for extrusion-based 3D printing, (ii) tailoring polypropylene for extrusion-based additive manufacturing and (iii) a new class of $(AB)_n$ segmented copolyetherimides for 3D and 4D printing.

The *Introduction* gives a brief overview on 3D printing technologies with special emphasis on extrusion-based 3D printing. The principles, challenges, and the commonly used polymers are discussed. Special focus is given on the semi-crystalline polypropylene, which is underrepresented in extrusion-based 3D printing in spite of its outstanding broad property profile. In addition, smart materials with shape memory effects are presented in view of 4D printing.

This cumulative thesis consists of three topics which resulted in already two publications and one manuscript. An overview of the thesis as well as a summary of the major achievements are presented in chapter *Synopsis*.

The first topic deals with the development of an *efficient material screening method to identify and optimize thermoplastic polymers for extrusion-based 3D printing*. Usually, the feedstock material is a continuous filament and for the filament production quantities of several kilograms are required. To overcome this, an efficient small-scale screening and testing method which requires only 10 to 50 g is essential to screen and further develop materials for extrusion-based 3D printing. This was achieved in this thesis by using a mini compounder and a mini injection molding machine to produce short filament rods which were joint together and used as feedstock in the 3D printer. In

addition, a special test specimen, in form of a printed free-standing square tube consisting of only a single-material-line stack was used for evaluation of critical performance parameters of the printed parts. Warp deformation was measured from printed square tubes and also interlayer bonding quality was obtained utilizing small-scale tensile specimens punched out of printed square tube sidewalls. By this developed method, the required time and material consumption are significantly reduced. To validate this method, three different grades of polypropylene are processed into filament rods and compared to two commercially available PP filaments and a commercial ABS filament. For all PPs significant warpage were observed compared with ABS and PLA due to the semi-crystalline nature, the lower degree of crystallization, and the E-modulus lead to reduced warp deformation. Isotactic PP with a relatively high degree of crystallization and stiffness demonstrated the highest geometric deformation. The investigated polypropylene-ethylene random copolymer with a lower degree of crystallization and stiffness exhibited reduced geometric deformation. In conclusion, semi-crystalline PP, with increased interlayer bonding quality compared with ABS and PLA, is a promising extrusion-based 3D printing material with an improved isotropic property.

The second topic deals with *tailoring polypropylene for extrusion-based 3D printing*. Polypropylene is one of the most commonly applied semi-crystalline thermoplastic in consumer and technical products and therefore, an interesting candidate for 3D printing. However, at the beginning of the thesis, only a limited number of commercial PP filaments were available, which suffer from relatively high volume shrinkage and warp deformation. Therefore, different PPs grades were selected and modified with the aim to reduce warp deformation and to reduce the anisotropic properties by improving the interlayer bonding quality. Two commercially available grades of polypropylene/ethylene random copolymers with a lower degree of crystallization were explored. To modify these grades, a β -nucleating agent, several amorphous polypropylenes (aPP) and one linear low-density polyethylene (LLDPE) were selected as additive or blend component. The achieved results demonstrate that the crystallization behavior and E-modulus of polypropylene play a significant role in reducing warp deformation. The addition of a selected β -nucleating agent showed a slightly negative influence on the material performance as this additivation could neither reduce the geometric deformation nor increase the interlayer strain bonding quality. By blending two different raco PP grades with aPP grades, warp deformation could be drastically reduced. In addition, the interlayer bonding strength is remarkably enhanced in these blends in spite of slight decreases in stiffness. An outstanding interlayer bonding strength was achieved in blends with raco

PP/aPP. This was confirmed by tensile tests, optical microscope, and visualized by a 3D printed frog which allows repeatable jumps and withstands a static weight loading of 5kg.

In the third topic, a new class of $(AB)_n$ segmented copolyetherimides for 4D printing was developed. $(AB)_n$ segmented copolyetherimides consisting of perylene and poly(ethylene-glycol) are rarely published except in the application fields of all-organic polymer batteries and organic photovoltaics. Due to the low-melting crystals of PEG segments and the high-melting perylene imide aggregates, $(AB)_n$ segmented copolyetherimides are promising for 4D printing by utilizing 3D printing in combination with the shape memory property. The $(AB)_n$ segmented copolyetherimides were synthesized and characterized regarding their thermal, rheological, and mechanical properties in view of 3D printing properties. The perylene imide segments act as reversible physical crosslinks which disassemble at temperatures between 100 and 200°C. The existing crystallinity of PEG segments improves the stiffness of produced filament rods, which is important to feed them smoothly into the 3D printer. The results demonstrate that this type of $(AB)_n$ segmented copolyetherimides combine good 3D printing performance with low warp deformation and excellent interlayer bonding. The PEG segments exhibit a low melting temperature around 40 to 60 °C and are semi-crystalline at room temperature, which could act as switching domain for shape memory programming. With a blend of two synthesized $(AB)_n$ segmented copolyetherimides, shape memory effect is realized by tuning the thermal transitions. By 3D printing this blend, 4D printing is achieved and demonstrated.

As a summary, this thesis reveals new essential findings for extrusion-based 3D printing. With the help of the developed powerful screening method, promising novel materials have been investigated and developed with tailored properties and optimized printing performances for extrusion-based 3D and 4D printing.

Acknowledgment

First of all, I would like to thank my supervisor Prof. Dr. Hans-Werner Schmidt for giving me this new, interesting and interdisciplinary research topic. I am grateful for the opportunity to attend a lot of conferences, participate in industry projects, and also the special experience to found our own company. Besides, I would like to thank Prof. Schmidt for the financial support of my research project and my permanent residence in Germany. Most important, I've learned a lot from Prof. Schmidt about the spirit of "German Quality and Precise" in scientific research.

Special thanks go to Dr. Christian Neuber for fruitful discussions, ideas, and inspirations. I thank Christian for his guidance and tutoring from my master thesis to the end of my PhD. Moreover, Christian treats me like a family member, which makes me feel warm in Bayreuth. Every time, when I faced with difficulties and problems, Christian is always willing to help.

I thank Dr. Reiner Giesa for many fruitful scientific discussions and laboratory works. He helps me a lot with practical laboratory work including machines and software.

I am indebted to thank the entire research group of Macromolecular Chemistry I for all the cooperativeness and the fantastic working atmosphere. It was always a pleasure to come to University of Bayreuth and I never felt alone! Special thanks go to Alexander, Jonas, , who solved quite a few of my computer and 3D printing problems. Klaus K., Felix K., Daniel K. Christoph S., Jutta and Sandra are gratefully acknowledged for providing the laboratory experiences and chemicals for my research topic. I really want to thank the secretaries Petra and Christina for their kindness and helpfulness; they helped me really a lot. Very important, I thank Andy F. and Andy S., who treat me as a brother, support me to face all the difficulties in Germany.

I thank the PPprint GmbH founder members Prof. Schmidt, Christian N., Sebastian S., and Dominik W., thank you for the enjoyable and memorable startup time that spending with you in the last two years.

At last, I thank my parents for their ongoing remote support, especially when I faced difficulties in Germany. This work would not have been possible without their caring support and help.

Erklärung

(Eidesstattliche) Versicherungen und Erklärungen

(§ 9 Satz 2 Nr. 3 PromO BayNAT)

Hiermit versichere ich eidesstattlich, dass ich die Arbeit selbstständig verfasst und keine anderen als die von mir angegebenen Quellen und Hilfsmittel benutzt habe (vgl. Art. 64 Abs. 1 Satz 6 BayHSchG).

(§ 9 Satz 2 Nr. 3 PromO BayNAT)

Hiermit erkläre ich, dass ich die Dissertation nicht bereits zur Erlangung eines akademischen Grades eingereicht habe und dass ich nicht bereits diese oder eine gleichartige Doktorprüfung endgültig nicht bestanden habe.

(§ 9 Satz 2 Nr. 4 PromO BayNAT)

Hiermit erkläre ich, dass ich Hilfe von gewerblichen Promotionsberatern bzw. -vermittlern oder ähnlichen Dienstleistern weder bisher in Anspruch genommen habe noch künftig in Anspruch nehmen werde.

(§ 9 Satz 2 Nr. 7 PromO BayNAT)

Hiermit erkläre ich mein Einverständnis, dass die elektronische Fassung meiner Dissertation unter Wahrung meiner Urheberrechte und des Datenschutzes einer gesonderten Überprüfung unterzogen werden kann.

(§ 9 Satz 2 Nr. 8 PromO BayNAT)

Hiermit erkläre ich mein Einverständnis, dass bei Verdacht wissenschaftlichen Fehlverhaltens Ermittlungen durch universitätsinterne Organe der wissenschaftlichen Selbstkontrolle stattfinden können.

Bayreuth, den 05.08.2020

Minde Jin